Design, Synthesis, Manufacture, Characterization and Evaluation of Lipid Nanocapsules in Chitosan-Iota-Carrageenan based Hydrogel Scaffold as a Potential Anti-Covid-19 Drug Delivery System

A thesis submitted at Rhodes University in fulfilment of the requirements for the degree of

Master of Science (Chemistry)

By

Grady Kathondo Mukubwa

B. Pharm (University of Kinshasa)

Supervised by Professor RUI WERNER MAÇEDO KRAUSE

Co-supervised by Professor RODERICK BRYAN WALKER

June 2022

Dedication

To my later father, Pharmacist Mumbere Kathondo Félicien

To my beloved grandmother, Felly Thembo Kathondo

Acknowledgement

I am very grateful to everybody who supported me throughout this research journey making this final work possible.

My utmost, sincere and deepest gratitude particularly goes to:

The Lord my God, for the gift of life, without which all this would never occur;

Professor Rui Werner Maçedo Krause, who happily accepted to host me in his lab and to supervise my research. For having been a guide, an advisor, a father and a role model in science, may he find through this work the fruits of his seeds of excellence sown in me;

Professor Roderick Bryan Walker who accepted, without hesitation, to become my co-supervisor and granted me access to analytical facilities in his research laboratory, in addition to his valuable advices;

Professor Tetana Zikhona from the University of the Witwatersrand for helping with some analytical facilities;

The NGO Förderverein Uni Kinshasa e.V/Else-Kroener Fresenius Stiftung for the incredible intellectual and financial support to my studies through the special scholarship program "Bourse d'Excellence Bringmann aux Universités Congolaises" (BEBUC);

Mr Safari Bazibuhe Justin for mentoring and supporting me throughout my research journey;

Mrs Samantha Mabvira, Msc from the Biopharmaceutical Research Laboratory, for introducing me to the Design of Experiments and for all her support and advices;

Mr Marvin Randall, for his unconditional help in performing the TEM, SEM and EDS analyses;

The staff members of the Chemistry Department at Rhodes University;

My fellow members of the Organic and Medicinal Chemistry Research Laboratory F22 and the Biopharmaceutical Research Laboratory S10, for their precious collaboration;

My lovely family members, for their unconditional love. I think of my grandmother Felly, my mother Astrid, my uncles and aunts, my brothers, sisters and cousins: Divine, Germaine, July, Gemima, Enock, Keren, Erick, André, Félicien, Felix, Roland, Billy;

My beloved friends and companions, Eunice Ngomba Mwamba, Kamfis Kamavu, Christian Rukumbuka, Choonzo Chiyumba, Yolande Openda, Bafokeng Sekaleli, Francis Agyeman, Urbain Ndagano, Edden Makangila, Rachel Ndoole, Thierry Shauri, Bienfait Isamura, Mofeli Leoma. May each of them find in this work a mark of unconditional love and friensdship.

Abstract

Covid-19 is a deadly viral disease that has been rampant around the world since 2019. Although the successful introduction of the vaccine has reduced the spread of covid-19, new cases and deaths are still being recorded. To date, no specific curative antiviral treatment has been approved for covid-19. However, many existing antiviral drugs have been and are still being studied against covid-19 and some of them, such as Remdesivir, have shown promise and could be repurposed to treat this infection. Unfortunately, antiviral drugs are prone to resistance as most of them have poor biopharmaceutical properties, including low solubility, permeability and bioavailability, which could hinder any clinical success.

Recent advances in nanotechnology-based delivery systems have made it possible to improve the biopharmaceutical properties of many drugs, especially those of poorly water-soluble drugs, by formulating them as lipid nanoparticles (LNP). Thus, in order to contribute to the fight against covid-19, this work aimed to develop Lipid Nanocapsules (LNC), based on some natural raw materials, which could improve the biopharmaceutical properties of antiviral drugs. In addition, since covid-19 infection is mainly respiratory, this work also aimed to fabricate a targeted delivery system based on a hydrogel capable of entrapping LNC and ensuring their efficient deposition and release in the lungs. The LNC consisted of a mixture of medium-chain triglycerides oil (MCT oil), crude soy lecithin, tween 80, NaCl and water, while the hydrogel consisted of a chitosan-grafted-iota carrageenan-grafted-poly (acrylamide-co-acrylic acid) system (CS-iCar-p (AAm-Co-AA)). Efavirenz (EFV), a drug with very low water solubility that has recently been demonstrated to have the potential to influence sars-cov-2 life cycle through different targets (3CLP, RdRp, Hellicase, 3'to5'exonuclease, 2'-O-ribose methyltransferase and EndoRNAse), was chosen as the model drug to evaluate the developed delivery system.

The combination of LNP and hydrogel results in a delivery system known as the LNP-hydrogel composite, an emerging area of research in the field of drug delivery. To date, no research has reported the design and fabrication of an LNC-CS-iCar-p (AAm-Co-AA) hydrogel composite that could effectively deliver an antiviral drug to the lungs in addition to its advantages in terms of biological activities.

Prior to the design of experiment, EFV solubility was assessed in water, labrafac lipophile 1349 and MCT oil. After that, the Design Expert Software version 13 was used to design the different experiments performed in this work. The I-optimal mixture design of experiments was performed for both LNC preparation and CS-iCar-p (AAm-Co-AA) hydrogel synthesis to study the impact of raw materials on the characteristics of these delivery systems. LNC were prepared using the phase inversion method while the free radical precipitation graft copolymerization method was used to synthesize hydrogel. In order to build polynomial models that could predict the amount of drug both LNC and CS-iCar-p (AAm-Co-AA) hydrogel can entrap, a D-optimal (custom) randomized design was performed. Moreover, various characterization techniques were used to investigate the physicochemical properties of the developed delivery systems. Thereafter, drug release studies were performed using a 1% sodium lauryl sulfate solution adjusted to either pH 4 or 7.

Solubility studies revealed that EFV was more soluble in labrafac lipophile 1349 and in MCT oil than in water; therefore, given its affordability, MCT oil was used for the LNC formulation. The design of experiment carried out allowed the construction of polynomial models that could predict, on the one hand, the droplet size, the polydispersity index and the Zeta potential of LNC, which were respectively around 50nm, below 0.2 and below -33. On the other hand, the model could predict the swelling capacity of the synthesized hydrogel, which was optimised to about 30,000% (300 g of water to 1 g of hydrogel). This turned out to be influenced by the proportion of polymers, the ratio of monomers as well as the concentration of the cross-linking agent. In addition, the characterization techniques further supported the improvement of EFV solubility by highlighting its conversion into its amorphous state after encapsulation in LNC. They also confirmed successful synthesis of CS-iCar-p (AAm-co-AA) hydrogel.

LNC were able to encapsulate about 87% of EFV while the synthesized CS-iCar-p (AAm-co-AA) hydrogel entrapped around 53% of EFV encapsulated in LNC. While LNC were able to release 42% and 27% of EFV after 74 hours in a 1% sodium lauryl sulfate solution (SLS) at pH 7 and pH 4 respectively, the LNC-CS-iCar-p (AAm-co-AA) hydrogel composite released about 50% and 40% of the drug after 9 days in the same release medium. Interestingly, the chemical integrity of the drug was preserved throughout the manufacturing process up to after its release, suggesting that the developed LNC-CS-iCar-p (AAm-co-AA) hydrogel composite could be used as a novel potential anticovid-19 drugs delivery system.

Graphical Abstract

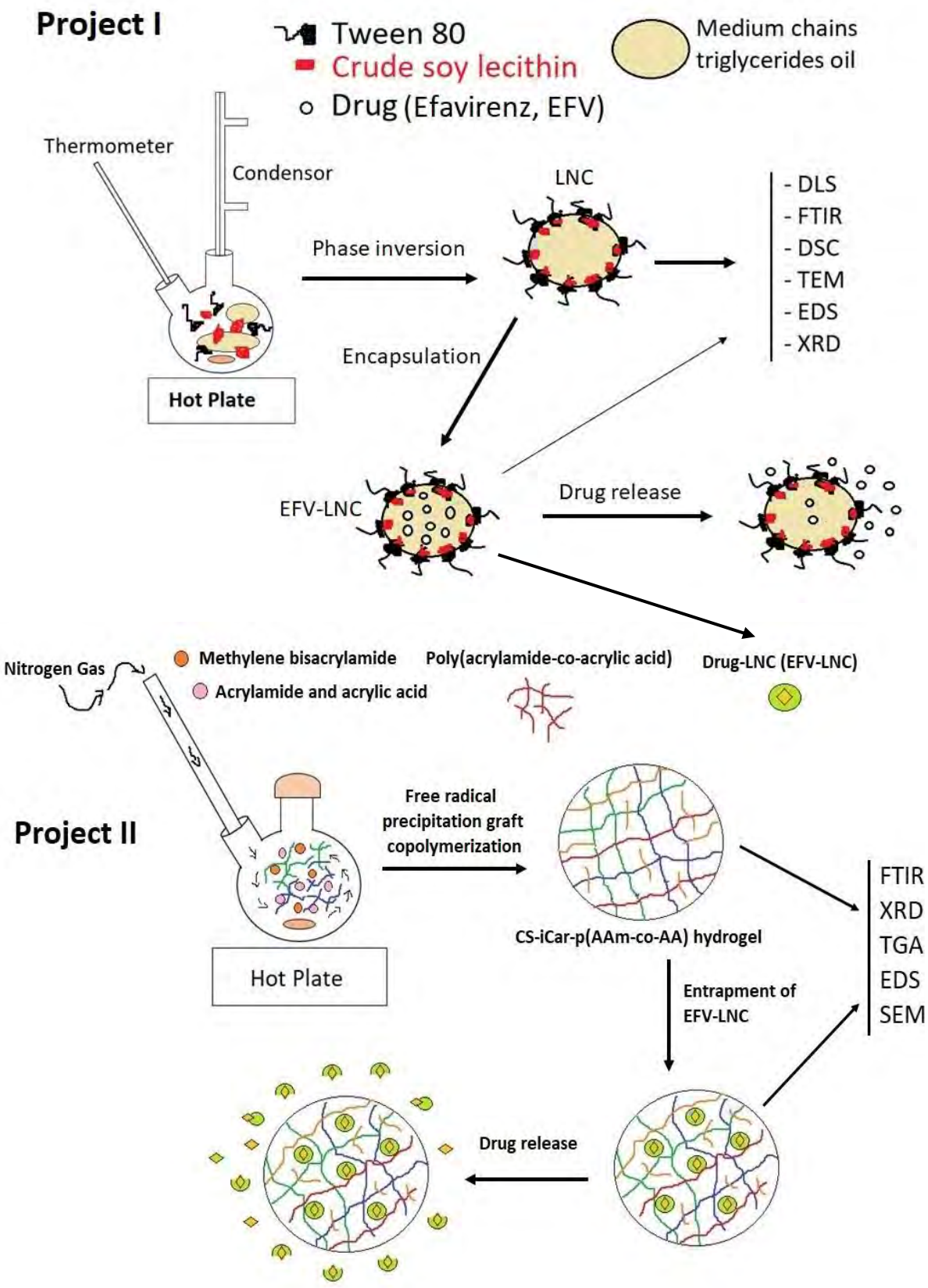

Table of Content

List of Figures

List of Tables

List of Equations

Chapter One

General Introduction

1. GENERAL INTRODUCTION

1.1. Covid-19

1.1.1. Introduction

Covid-19 is a viral disease caused by severe acute respiratory syndrome coronavirus 2 (sars-cov-2), a highly contagious corona virus identified for the first time in Wuhan in China as of December 2019. During the last two years, covid-19 pandemic has been devastating for the world, closing schools, communities and businesses, with emergence of new life habits like wearing masks, remote work, and social distance and so on. Although effective vaccines have been developed and tested in record time, the emergence of worrying new sars-cov-2 variants has dimmed the hope for vaccination and brought back the deadly threat of the disease. As a result, scientists and the global health system are still working hard to develop sustainable vaccines and therapies to tackle all emerging variants and to ensure that everyone in the world is vaccinated.

1.1.2. Epidemiology

The covid-19 outbreak was reported for the first time to the World Health Organisation (WHO) on December 31st 2019. Few days after, on 7th January 2020, the virus responsible for the outbreak has been identified as a coronavirus above 95% and 70% similar to the bat coronavirus and the SARS-Cov, respectively[1]. Patient zero of this new coronavirus turned out to be a Chinese woman selling shrimp in the Wuhan Huanan seafood wholesale market that was therefore considered to be the origin of the virus after environmental samples collected there tested positive[1,2]. To date, although bats are known to be the source of the sars-cov-2 virus, the animal through which the virus passed to humans is still undetermined, with pangolins and snakes being the suspects to date.

As the number of positive cases began to rise dramatically among people who have not been exposed to the live animal market, it was obvious that human-to-human transmission was taking place[3]. The covid-19 infection is very contagious and is transmitted by droplets released from coughing and sneezing of symptomatic patients or asymptomatic ones before symptoms appear. Given that the infected droplets can spread up to two meters or settle on surfaces, people get infected either by inhaling them or by touching contaminated surfaces and then their nose,

mouth and/or eyes. It is also assumed that the virus can be found in the stool and water supply and could therefore be transmitted via the feco-oral route[1,4].

People of all ages and from all over the world are at risk of catching the virus and developing the disease. According to current epidemiological data, more than 500 million confirmed cases and over 6 million deaths have been reported worldwide. As of 17th April 2022, among the six WHO regions, the Europe region turned out to have experienced the strongest hit of the disease in term of cumulative cases (42%) followed by Americas (30%), South-East Asia (11%), Western Pacific (10%), Eastern Mediterranean (4%) and Africa (2%). As far as the cumulative number of deaths is concerned, Americas appeared to be number one on the list (44%) followed by Europe (32%), South-East Asia (13%), Eastern Mediterranean (6%), Western Pacific (4%) and Africa (3%)[5].

Overall, despite the success of various strategies implemented to combat it, new cases and deaths are still being recorded. In the week of 11-17 April 2022, more than 5 million new cases and 18,000 deaths were reported in the six WHO regions, with South Korea having the highest number of cases and the United States of America the highest number of deaths[5].

However, it is worth mentioning that of these new cases and deaths, the African region as a whole had only 25,107 and 87 respectively. Since the start of the covid-19 pandemic, the African region has remained significantly less affected than the Americas, Europe and Asia. The clear reasons for this contrast are not yet known. Nevertheless, this low prevalence of covid-19 disease in the African region has been attributed to a number of factors. One of these is the age of the population, which is considered an important risk factor. Globally, it has been observed that the majority of deaths due to Covid-19 disease have occurred in people in their sixties or older. The overall African population average age is less than 20 years old with only around 4% of the whole population being over 65 years old compared to other WHO regions, where around 35% of the Eastern and South-Eastern Asia population and 29% of the Europe and Northern American population is over 65. Hence, it is assumed that it could be normal that only a few deaths have been reported for Africa[6–11]. Other factors hypothesized to limit the impact of covid-19 disease in Africa include potential cross-immunity due to previous exposure to other infectious diseases like malaria or to other circulating coronaviruses; lack of long-term care facilities; possible dramatic undercounting of deaths due to limitations of the SARS-Cov-2 test[7,8,12,13].

Paradoxically, South Africa is an exception among other African countries. As of 17 April 2022, according to a WHO update, 47 African countries have been affected by the covid-19 pandemic, with more than 8 million cumulative cases and over 170,471 deaths. Of these, South Africa has recorded over 3 million (45.2%) cases and 100,147 deaths (59.0%)[14]. This discrepancy could be explained by the fact that the average age of the South African population is a bit higher than in most African countries, as well as by the presence of a long-term care sector[6,15]. In addition, South Africa has a higher prevalence of HIV and tuberculosis, which have been associated with higher covid-19 mortality rates. Other reasons include the higher prevalence of non-communicable diseases compared to other countries, better diagnostic capabilities and health care, facilitating the reporting of many new cases[13,16].

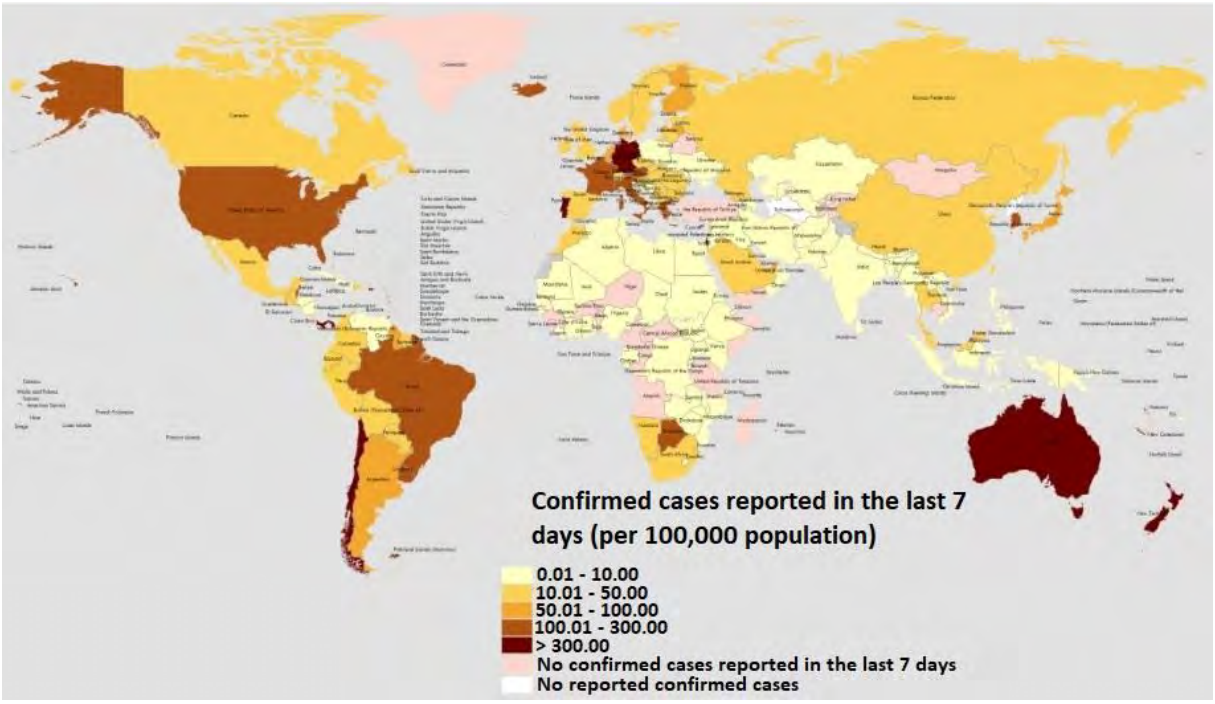

Figure 1. *Global distribution of covid-19 new cases as of June 15, 2022 (WHO, weekly epidemiological update – 15 June 2022, https://www.who.int/publications/m/item/weekly-epidemiological-update-on-covid-19---15-june-2022, last access June 16, 2022)*

1.1.3. Pathogen

1.1.3.1. Virus: SARS-Cov-2

Severe acute respiratory syndrome coronavirus 2 is one of the coronaviruses that commonly affect birds and mammals. Coronaviruses belong to the family Coronaviridae and more specifically to the subfamily Coronavirinae. This includes the genera Alpharacoronavirus, Betacoronavirus, Gammacoronavirus, and Deltacoronavirus. Of these, only alphacoronaviruses and betacoronaviruses can cause disease in humans. SARS-Cov-2, which is an RNA virus,

belongs to the betacoronavirus genus. Its genome is a single-stranded positive RNA (+SSRNA) with an average size of about 30 kilobases, making it, along with other coronaviruses, larger than all other RNA viruses[17,18]. The SARS-Cov-2 genome encodes structural proteins and an open reading frame polyprotein (ORF1a/ORF1ab polyprotein) that are being extensively studied as major drug targets. In addition, the genome has several open reading frames that code for accessory proteins that are not essential for viral replication, but which have been shown to play a role in pathogenesis[19]. The four main structural proteins encoded by the SARS-Cov-2 genome are the nucleocapsid protein (N), transmembrane protein (M), envelope protein (E) and spike protein (S)[18]. Of these, the N protein is the most expressed during infection. It consists of a single strand of positive ribonucleic acid (RNA). This protein not only plays an essential role in maintaining the RNA structure of the virus, but is also known to be highly immunogenic, which explains its use in vaccine development and serological testing. Once the virus has infected the organism, the N protein enters the host cell with the viral RNA where it facilitates viral transcription and neutralises cellular interferons and suppressors of RNA 5 transcription, thereby hindering or thwarting the host response to the virus[20–22].

On the other hand, the spike protein is another part of sars-cov-2 that plays a critical role in its fate and pathogenicity. It consists of an elongated transmembrane protein that gives the virus a crown-like appearance when viewed under the electron microscope. The Spike protein has been identified as the key mediator of sars-cov-2 entry into cells by binding to the angiotensin-converting enzyme receptor 2 (ACE2) after its activation by human proteases[20,23]. ACE2 is widely expressed in respiratory epithelium, nasal epithelial cells, small intestinal enterocytes and slightly in endothelium, myocytes and smooth muscle[24,25].

In addition, the most abundant structural protein of the virus is the M protein, which is responsible for the shape of the viral envelope. The M protein also contributes to reducing/preventing host defence against the virus and plays a central role in the assembly of the virus with other coronaviral structural proteins. The smallest viral structural protein is the E protein, a short integral membrane protein of 109 amino acids that plays a role in virus assembly, release and pathogenicity[20,26].

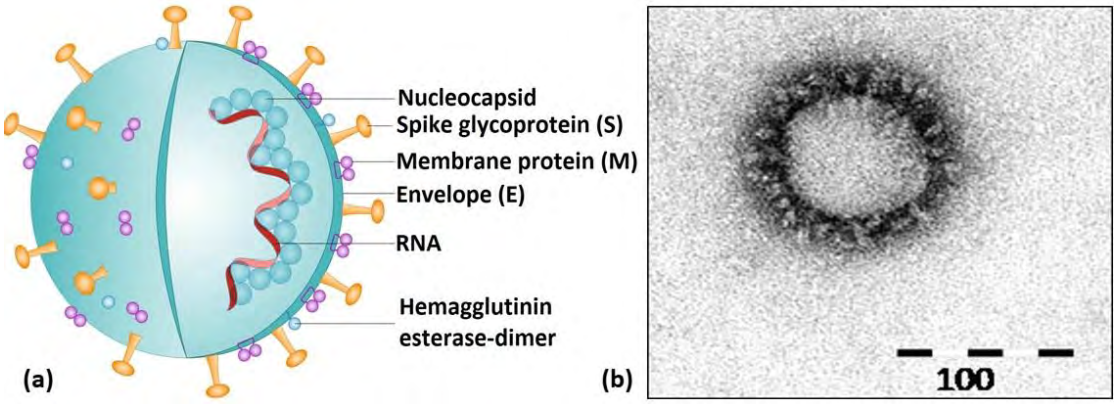

Figure 2. *(a) SARS-Cov-2 structure illustrating a positive-sense RNA virus with its four principal structural proteins namely nucleocapsid (N), spike glycoprotein (S), membrane protein (M), and envelope (E). Photo credit to Florindo et al.*[27]. *(b) SARS-Cov-2 structure through electronic microscope lenses illustrating a crown of peplomers, which is characteristic of the Coronavirus genus. Photo credit to Dr Monica Birkhead, SVP CEZPD, https://www.nicd.ac.za/nicd-capacity-for-isolation-and-culturing-of-severe-acute-respiratory-syndrome-coronavirus-2-sars-cov-2-from-clinical-specimens/, last access June 16, 2022).*

1.1.3.2. SARS-Cov-2 variants

While the WHO and health systems around the world have been trying to contain and combat the disease with different strategies, new variants of the virus have begun to emerge and drown out the growing hopes of controlling and eradicating the virus, posing new challenges to the scientific community. Indeed, variants are known as viral genomes containing one or more mutations. They are classified in terms of lineages or groups of lineages that are designated differently as Variant of Concern (VOC), Variant of Interest (VOI), Variant of High Consequence (VOHC) or Variant to Watch (VBM) depending on how public health authorities should respond/react to their respective attributes and characteristics[28]. The most worrying/alarming of these variants is the "variant of concern". Several parameters are considered in order to designate a variant as a "variant of concern". This is particularly when the variant is found to be increasingly contagious, causing severe illness that could be explained by an increasing number of hospitalizations or deaths. In addition, there must also be evidence of the new variant resistance to antibodies, which was acquired during a previous infection or vaccination. A variant is also termed a "variant of concern" when it no longer responds to existing/established treatments, vaccines or diagnostic tools. On the other hand, VOI are similar to VOC and refer to variants that have shown specific genetic markers that may affect virus spread, diagnosis, established treatments and immunity. Variants must also be linked to an increase in the number of cases to be considered VOI[28,29].

So far, different variants have been identified/recognised and some of them, namely alpha (B.1.17), beta (B.1.351), gamma (P.1), delta (B.1.617.2) and epsilon (B.1.427; B.1.429), have been downgraded from VOC to MBV. MBVs are variants that had characteristics of VOCs or had a potential or obvious impact on approved or authorised medical countermeasures, but which are no longer detected or are circulating at very low levels. On the other hand, variants eta (B.1.525), iota (B.1.526), kappa (B.1.617), N/A (B.1.617.3) and zeta went from being qualified as VOI to VBM. Currently, only Omicron is considered as a "Variant of Concern". It was first identified in South Africa in samples from a patient in Botswana, before being detected in many other countries around the world[28–30].

1.1.4. Pathogenesis

Although the understanding of covid-19 pathogenesis is still inadequate, it can be explained by analogous pathogenic mechanisms of SARS-Cov and MERS-Cov. Like SARS-Cov, SARS-Cov-2 enters the host cell by binding to the ACE2 receptor through proteins interaction [2,31]. Thanks to critical proteolytic event happening in S protein, the viral membrane directly fuses with the host cell membrane resulting in its endocytosis, followed by its fusion with the endosome membrane, hence allowing the nucleocapsid release in the host cell cytoplasm[2]. The following event consists of viral RNA release that results from the proteolytic degradation of the N protein of the nucleocapsid. Once released, the viral RNA is replicated as partial and complete genome copies and translated in the endoplasmic reticulum to form new SARS-Cov-2 virions [32]. Few days of incubation after, accounting for 2 up to 14 days, the viral propagation and migration happens thereof and triggers a strong immune response (such as the cytokine storm) resulting in clinical manifestation of covid-19 disease [33]. Although some people are likely to be asymptomatic, covid-19 is generally expressed by fever, tiredness and dry cough, sometimes aches, pains, nasal congestion, running nose, sore throat, dyspnea, fatigue, viral pneumonia or diarrhea. Complications encompass pneumonia, acute respiratory syndrome, multi organ failure, septic shock and all this may eventually lead to death[1,2].

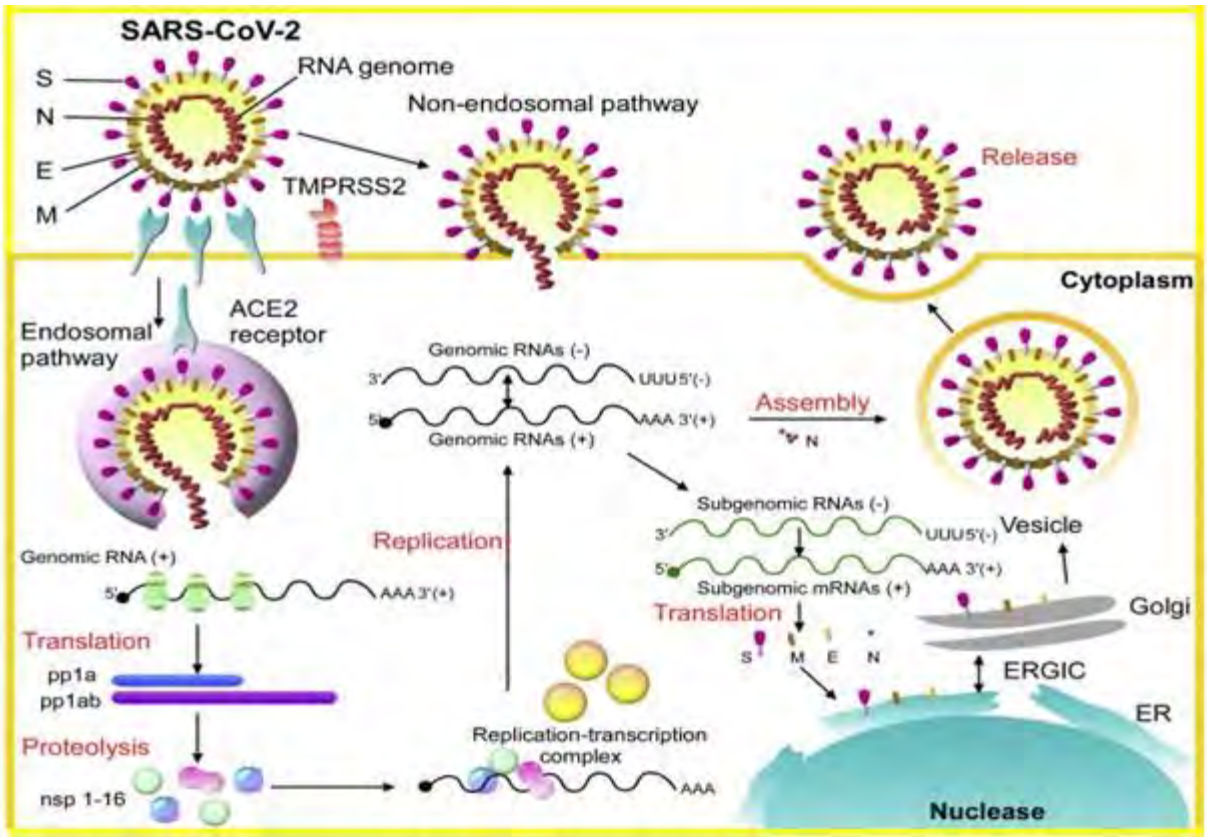

Figure 3. *Schematic representation of SARS-Cov-2 replication. Photo credit to Liu et al.* [34].

1.1.5. Diagnosis

Covid-19 diagnosis is based on epidemiological record, clinical symptoms and paraclinical analyses. As far as paraclinical analysis are concerned, different approaches are possible, namely nucleic acid detection tests including next generation sequencing, reverse transcription-polymerase chain reaction (RT-PCR) and loop-mediated isothermal amplification (LAMP); imaging tests especially the chest computed tomography scan (CT scan); the antigen-antibody based tests such as the enzyme-linked immunosorbent assay (ELISA); and some alternative tests such as biosensors, paper based devices and point-of-care test (POCT). Among them the antigen and RT-PCR tests are the most used techniques for the diagnosis of covid-19[35].

1.1.5.1. Antigen based tests

Antigen tests are based on the identification of specific proteins present on the surface of sars-cov-2. They are performed by collecting swab samples from nasopharynx and anterior nares. Antigen tests provide fast result within less than half an hour and are therefore used to diagnose an active or acute infection. They are more affordable than RT-PCR tests and do not require any specialized facility to be performed. However, they lack specificity and show low sensitivity. Therefore, they are likely to result into many false negative responses[35,36].

1.1.5.2. Antibody based tests

Antibody tests, also known as serological tests, are performed by using blood samples rather than swab samples. They are based on the identification of antibodies contained in the blood sample at either a significant or measurable concentration. The antibody tests mainly target immunoglobulin M and immunoglobulin G, which are produced by the immune system in response to the viral infection. These tests are intended to detect a past infection rather than diagnosing the infection, as it takes up to three weeks after infection for antibodies to develop and be detected in the serum. Different techniques can be used to perform antibody tests, namely lateral and immunoassay tests like the enzyme-linked immunosorbent assay (ELISA) and the chemiluminescent immunoassay (CIA). Although antibody tests allow identification of past infection in asymptomatic patients, negative tests do not necessarily mean absence of previous infection given that some people do not develop detectable IgM and IgG following the infection[37,38].

1.1.5.6. Reverse transcription-polymerase chain reaction (RT-PCR)

RT-PCR tests are molecular tests based on identification of genetic material of the virus. Different groups of sars-cov-2 genes may be used for this purpose such as ORF-1a gene, ORF-1b gene, RdRp gene, N gene, E gene etc. The RT-PCR tests use nasopharyngeal or oropharyngeal swabs or anterior nasal swabs. They appear to be the most reliable tests for the diagnosis of covid-19 given their high sensitivity around 95%. However, this sensitivity is affected by the quality of the sample, which depends on the time of collection, the amount collected and the maintenance of cold chain. Failure to collect and keep sample appropriately may yield false-negative results. Furthermore, in addition to long analysis time and having a specialized laboratory to run RT-PCR tests, these ones pose a risk of biological safety hazards during sample transport and processing[35,39].

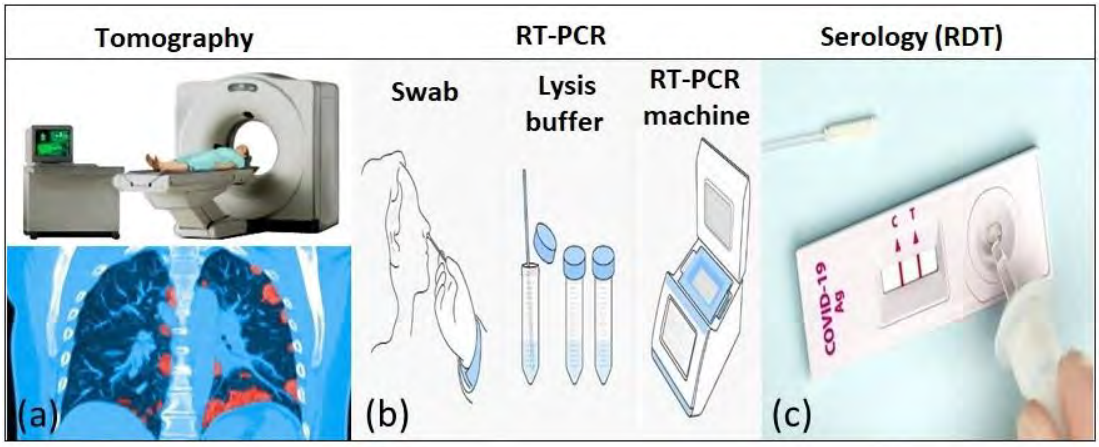

Figure 4. *Covid-19 diagnostic tools representation.*

(a) Tomography analysis (https://www.mountsinai.org/health-library/tests/thoracic-ct, https://www.sciencenews.org/article/coronavirus-covid-19-some-patients-may-suffer-lasting-lung-damage, accessed in June 16, 2020).
(b) Reverse Transcriptase Polymerase Chain Reaction analysis (RT-PCR) (https://www.businessinsider.co.za/how-coronavirus-throat-tests-work-rt-pcr-method-explained-2020-4?r=US&IR=T, accessed in June 16, 2022). (c) Rapid Diagnostic Test (RTD) of Covid-19 based on serology (https://www.traveldailymedia.com/post-pandemic-travel-the-hidden-cost-of-testing/, accessed in June 16, 2022).

1.1.6. Treatment

1.1.6.1. Preventive treatment

Since the dawn of time, it has been known that prevention is better than cure. This statement is still true today when it comes to covid-19. Since the beginning of the covid-19 outbreak, several strategies have been implemented to prevent the spread of covid-19. At national and international level, travel bans between most countries were established. However, as time went on, when boarders were reopened, compulsory covid-19 check out points were implemented in different airports and boarders worldwide to limit the virus propagation. At individual level, some barrier measures were recommended, namely wearing of face masks, hand washing and sanitizing as well as practicing social distancing up to two meters from each other [2].

Furthermore, since 2021, successful vaccination program has been carried out around the world to protect people against covid-19. Indeed, the widely used covid-19 vaccines include conventional inactivated ones (sinovac, sinopharm), adenovirus-vectored (Gamaleya, J & J Jansessen, AstraZeneca), and mRNA (Pfizer, Moderna) vaccines, which are all meant to elicit neutralizing antibody (NAb). Despite the emergence of new variants of the virus, it has been surprisingly noticed that they remained effective. Hence, boosters doses of the vaccine have been recommended to level up the Nab concentration and counteract the threat of the variants [40].

1.1.6.2. Curative

Up to now, no specific curative antiviral treatment has been approved for covid-19. The management of the disease is mainly supportive and symptomatic. Different therapeutic protocols have been implemented worldwide. These include the repurposing of some drugs such as chloroquine and hydroxychloroquine used for many years to treat malaria. These two drugs have been associated to different mechanisms of action to combat sars-cov-2. These ones include interference in the endocytic pathways by increasing the endosomal pH that impedes the proteolytic cleavage of S protein and therefore the viral entry into the host cell [41], blockage of silica acid receptors, restriction of pH mediated S protein cleavage at the ACE2 binding site and prevention of cytokine storm [42]. Besides, based on former experience with SARS and MERS, other antiviral drugs such as ribavirin or the combination of lopinavir-ritonavir have also shown some efficacy against covid-19 although no added benefit of this combination has been demonstrated so far [1,43].

Interestingly, Remdesivir, an antiviral drug basically developed against ebola virus, has been successfully used against covid-19 and even received the FDA approval for use in covid-19 patients [44,45]. Remdesivir is known as an adenosine analogue that counteract the SARS-Cov-2 lifecycle by incorporating into nascent viral RNA chains resulting in its premature termination [41,45,46]. In addition to that, passive antibody therapy has demonstrated promising outcome in the treatment of covid-19. It is based on the administration of neutralizing antibodies. This phenomena is known as immunotherapy as it involves the use of the immune system agents among which monoclonal antibodies are accounted as the majority of biotherapeutics used either for prevention or to fight against the virus. Unlike the active vaccination, that requires more time to develop, passive antibody therapy is likely to provide urgent and immediate immunity to vulnerable people [2].

Human serum from convalescent covid-19 people is a possible source of antibody that could be used to improve covid-19 patients' clinical status [47]. As of now, sotrovimab, a pan-sarbecovirus monoclonal antibody, has received FDA Emergency use authorization to hinder covid-19 progression early in the course of the disease, especially in high-risk patients. Although its mechanism of action is still unknown, sotrovimab is assumed to impede membrane fusion by binding to one spike protein preserved epitope [48,49].

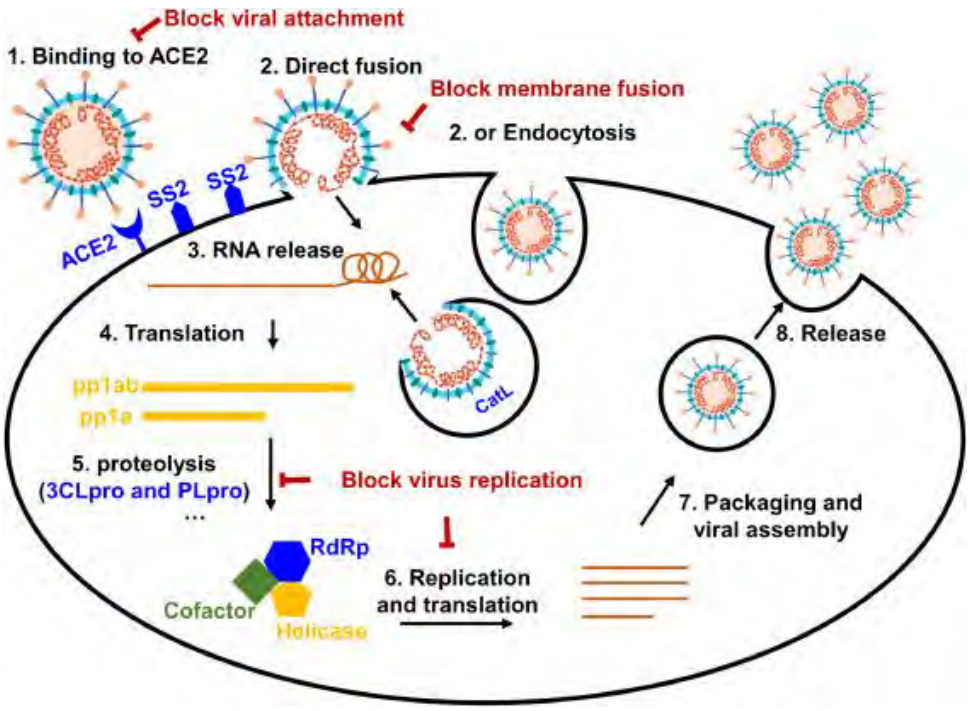

Figure 5. *Schematic representation of potential anti-covid-19 drug key targets in the SARS-Cov-2 life cycle. Photo credit to Su et al.* [50].

1.1.6.3. Efavirenz

a) Physicochemical and molecular aspects

The physicochemical properties of Efavirenz (EFV) are presented in Table 1.

Table 1. *Physicochemical characteristics of EFV*

	Property name	Property value or description
1	Molecular formula	C14H19ClF3NO2
2	Molecular weight	315.67 g.mol-1
3	Systematic name (IUPAC)	(4S)-6-Chloro-4-(2-cyclopropylethynyl)-4-(trifluoromethyl)-2,4-dihydro-1H-3,1-benzoxazin-2-one
4	Melting point	139 – 141°C
5	Solubility	In water, 0.093 mg/L at 25°C
6	Exact Mass	315.0273907
7	Monoisotopic Mass	315.0273907
8	Topological polar surface area	38.3 $Å^2$
9	Heavy atom content	21
10	Physical description	Solid
11	Colour/Form	Crystals; white to slightly pink crystalline powder
12	Vapour pressure	3.8 x 10^{-7} mmHg at 25°C
13	Log P	4.6
14	Dissociation constants	pKa = 10.2

b) Structure

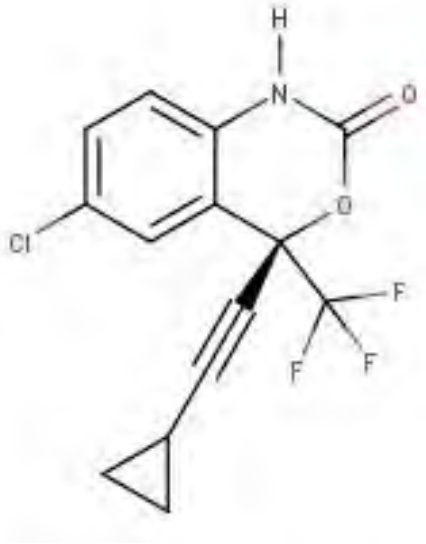

Figure 6. *Structure of Efavirenz drawn using Marvin Sketch Software.*

c) Synthesis of Efavirenz

Many synthetic procedures have already been used successfully to produce Efavirenz. They differ from each other depending on the starting materials, the number of steps, the cost, the yield, the optical purity as well as the industrial feasibility. One of those synthetic pathways is the synthesis of efavirenz involving resolution of enantiomers as described by Radesca et al.[51]. Briefly, reflux 4-chlorophenyl isocyanate (1) with tert-butanol in toluene to produce N-Boc-4-chloroaniline (2) in 93% yield. This is followed by lithiation of compound (2) ortho to the tert-butoxycarbonylamino group with sec-butyllithium. Thereafter, use ethyl trifluoracetate to quench compound (2) at -40°C to form the trifluoromethyl ketone (3) in 77% yield. Next step consists of addition of lithium cyclopropylacetylide (4) to compound (3) in THF at -40 to -35°C resulting in the tertiary alcohol (5) in 69% yield. Then treat this one with one equivalent of butyllithium in toluene followed by three hours reflux to obtain the racemic cyclic carbamate (±) -1 consisting of 6-chloro-4-cyclopropylethynyl-4-trifluoromethyl-1,4-dihydro-2H-3.1-benzoxazin-2-one, in 90% yield. Resolve this compound with camphonoyl chloride (7) using NaH in THF to obtain an amide (8) whose desired diastereomer is isolated by crystallization from hexane/ethyl acetate (93:7) in 37% yield. Finally, to obtain efavirenz ((-)-1), compound 7 is hydrolysed with DMSO/Water (4:1) in 92% yield[51].

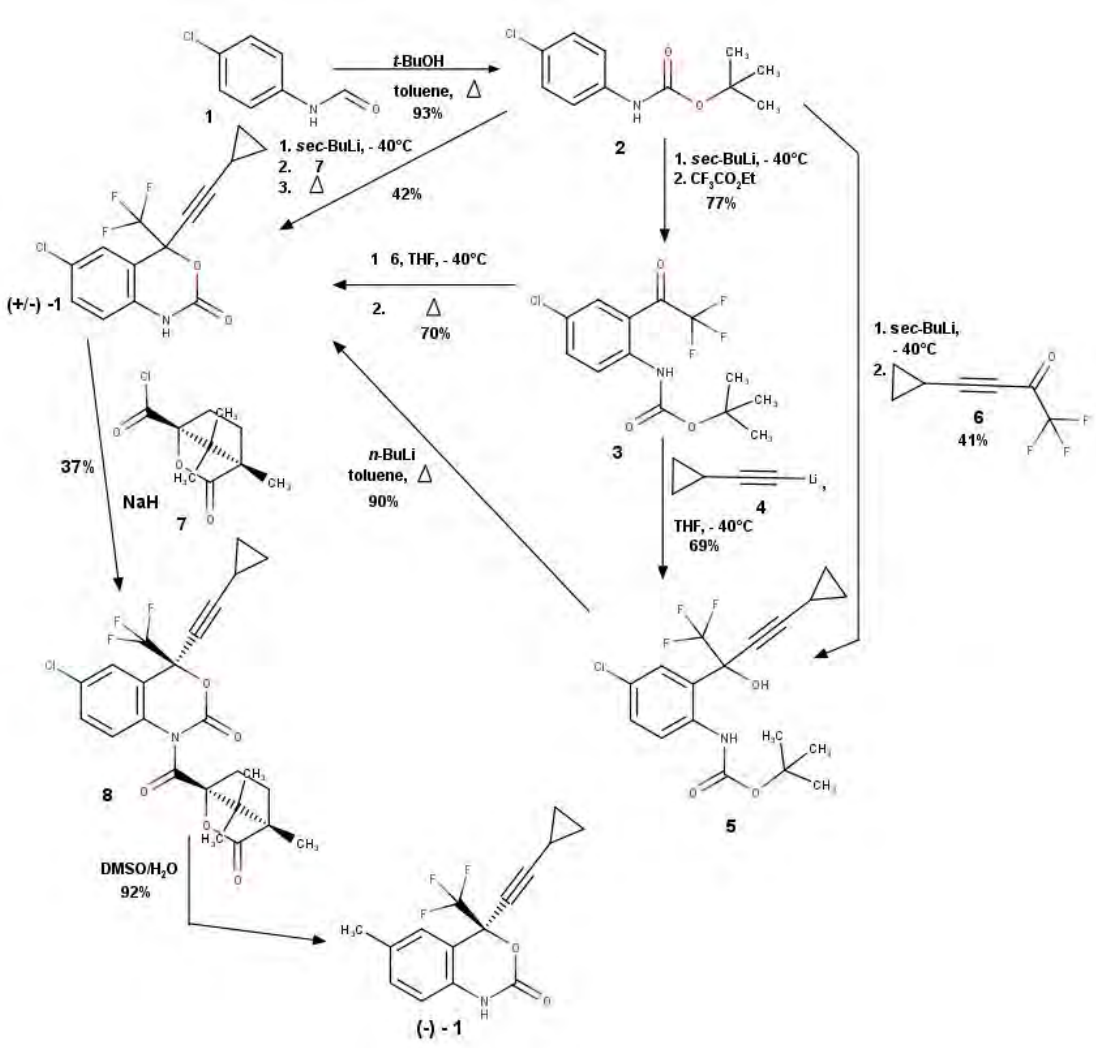

Figure 7. *Schematic representation of Efavirenz synthesis drawn with Marvin sketch, structures reproduced from Radesca et al.*[51]

d) Pharmacology of efavirenz

Efavirenz is an antiretroviral that belongs to the class of non-nucleoside reverse transcriptase inhibitors (NNRTIs). It is available as a solid oral dosage form namely as tablets and capsules[52]. Efavirenz is a benzoxazinone that acts by inhibiting the non-nucleoside reverse transcriptase of human immunodeficiency virus type 1 (HIV-1) resulting in the decrease of viral charge in the blood. It is indicated in the treatment of HIV patients with the aim of suppressing HIV replication for as long as possible and the daily dose ranges from 200 to 600 mg[52–55].

Efavirenz is well absorbed after oral administration and reaches peak concentrations of about 4.1 mg/ml 5 hours after dosing. Efavirenz is approximately 99% bound to plasma proteins. Its elimination half-life varies between 40 and 76 hours depending on whether it is taken once or multiple times[54–57]. The metabolism of efavirenz is primarily via CYP450 2B6 and 3A4 to hydroxylated metabolites followed by glucuronidation. Efavirenz induces and inhibits

cytochrome P450 and leads to autoinduction. It also inhibits CYP3A4, CYP2C9, and CYP2C19[58–60]. Thus, drugs metabolized by CYP2B6, 3A4, 2C9 and 2C19 are likely to interact with efavirenz. Efavirenz is therefore contraindicated in combination with agents that highly depend on the CYP450 3A4 metabolism pathway. It is also contraindicated to pregnant women during first semester, given the risk of foetal malformations. Patients under therapy with efavirenz are likely to experience some common adverse effects namely central nervous system symptoms, rash and hepatitis[59–61].

During the Covid-19 pandemic and based on predictions that HIV antiretroviral drugs may be the best compounds to treat Covid-19, several antiretroviral drugs, including Efavirenz, have been subject to intensive *in silico* studies to evaluate and determine their ability to inhibit SARS-Cov-2 virus and thus become potential candidates for Covid-19 management[62,63]. According to results obtained from an *in silico* study carried out on some commercially available antiviral drugs, Efavirenz exhibited a promising binding affinity to the SARS-Cov-2 3C-like proteinase, with a dissociation constant (Kd) value of 199.17 nM. Efavirenz also targeted different other targets on the virus including 3CLP, RdRp, Hellicase, 3'to5'exonuclease, 2'-O-ribose methyltransferase and EndoRNAse suggesting that further studies could be performed to confirm its activity against SARS-Cov-2 [64,65].

1.2. Lipid-nanocapsules (LNC)

1.2.1. General consideration of LNC

Lipid-nanocapsules (LNC) are a type of lipid nanoparticles that have been developed, along with solid lipid nanoparticles, as an alternative to the use of liposomes or polymer particles, as having the advantage of being produce in the absence of solvent[66]. The term "nanocapsules" stands for particles whose core is liquid or semiliquid surrounded by a solid film at room temperature (15-25°C), unlike solid lipid nanoparticles and lipid nanospheres which are matrixes whose entire mass is solid. LNC are colloidal systems according to their tiny size[67].

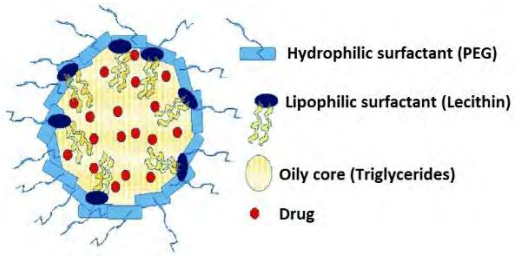

Figure 8. *Structure of lipid-nanocapsule (LNC) illustrating its three main components: medium chain triglycerides, poly ethylene glycol based surfactant and lecithin. Photo adapted from Rassouli et al.* [68].

1.2.2. Composition

LNC are mainly made of an oily core consisting of either triglycerides or fatty acid ester, a solid film coating the nanocapsules that consists of both a lipophilic surfactant such as lecithin whose proportion of phosphatidylcholine is between 40 and 80%, and a hydrophilic surfactant such as solutol ® HS15. While the triglycerides are formed by C8 to C12 fatty acids namely capric and caprylic fatty acids and mixtures thereof, fatty acid ester may be selected among C8 to C18 fatty acid esters like ethyl palmitate, ethyl oleate, ethyl myristate, isopropyl myristate, octyldodecyl myristate, and mixtures thereof. The LNC composition may also contain salt such as sodium chloride whose concentration has been demonstrated to provoke a shift in the phase inversion zone. Indeed, the higher its concentration, the lower the phase inversion temperature. The estimated proportions of these different components are described in table 2[67,69].

Table 2. *LNC Components with their respective lower and upper proportions*

	Proportion by weigh of LNC	
Component	**Lower (%)**	**Upper (%)**
Triglycerides	5	15
Lecithin	1	3
Hydrophilic surfactant	5	15
Water	64	89
Salt	1	4

Heurtault et al. developed lipid-nanocapsules preferably composed of the following main raw materials:

- Labrafac ® WL 1349 (Gattefossé, Saint-Priest, France) which is an oil made of caprylic and capric acid (C8 and C10) medium chain triglycerides. While its density varies from 0.930 to 0.960 at 20°C, its HLB value is about one.
- Lipoid ® S73-3 (Lipoid GmbH, Ludwigshafen, Germany) that corresponds to soybean lecithin containing around 69% phosphatidylcholine and 9% phosphatidylethanolamine. Lipoid ® S73-3 is solid at 37°C and at room temperature in the formulation.
- Solutol ® HS15 (BASF, Ludwigshafen, Germany), which is consists of poly-oxyethylene esters of 12-hydroxystearic acid and is used as the non-ionic hydrophilic surfactant of the formulation.

1.2.3. Preparation methods

As with nanoemulsions, different techniques could be used to produce LNC, including high-energy methods (high-pressure homogenization; microfluidization; ultrasonication) and low energy methods. Low energy methods include [70]:

- Phase inversion emulsification methods:
  - ✓ Transitional phase inversion (TPI) encompassing phase inversion temperature (PTI) and phase inversion composition (PIC)
  - ✓ Catastrophic phase inversion (CPI): emulsion inversion point (EIP).
- The self-nanoemulsification method

Of these methods, the phase inversion temperature turned out to be the most successful and widely used to produce LNC. The phase inversion temperature technique (PIT) was reported for the first time by Shinoda and Saito in 1968 [71]. It is well known for the production of microemulsions and nanoemulsions. The PIT is based on the affinity of surfactants toward the oil phase and the aqueous phase at 25°C. This affinity is determined by the hydrophilic-lipophilic balance (HLB) value. Briefly, the o/w emulsion obtained by mixing an oil phase containing lipid melt and non-ionic surfactant and an aqueous phase consisting of sodium chloride and water, is heated above the PIT. As the temperature increases, the polyethoxylated groups of non-ionic surfactants (polyethoxylated surfactants) get dehydrated, making the surfactant more lipophilic, resulting in higher affinity towards the oily phase. Hence, phase inversion from the initial o/w emulsion to water-in-oil (w/o) nanoemulsions occurs through intermediate liquid crystalline or bi-continuous structures [70,72,73]. However, if sudden cooling is applied, the system get destabilized and undergoes phase inversion again as the affinity of surfactant molecules is reversed. Interestingly, at this point, if rapid cooling or sudden dilution with cold water is applied, kinetically stable, spherical particles of desired shape, size and polydispersity form, i.e. the o/w nanoemulsions [74–77].

It is important to mention that phase inversion might not happen even in presence of non-ionic polyethoxylated (POE) surfactant. Although the presence of POE groups in the surfactant molecules is crucial for phase inversion induction, some non-ionic polyethoxylated surfactants possess either a too short or too long POE head group or either too long or too short hydrophobic chains, which are not sensitive enough to the temperature to induce phase inversion. The phase inversion temperature is the temperature at which, for a fixed composition, the relative affinity of the surfactant for both the lipid and the aqueous phase is equal [74,75].

Different techniques can be used to characterize the PIT or the emulsion inversion, including the following-up of the emulsion electrical conductivity, the measurement of turbidimetry or even eye-naked monitoring of the emulsion aspect changes from turbid to translucent or transparent [75,78,79]. The originality with this method comes in with the temperature cycling (number fixed at N=3) that results into very high stable nanoemulsions demonstrated to show nearly no droplets growth for at least a year unlike the ones obtained using the classical PIT method that are stable for only a few months [69,80,81].

1.2.4. Difference between nanoemulsions and lipid-nanocapsules

Nanoemulsions are either oil-in-water (o/w) or water-in-oil (w/o) conventional emulsions that contain very small particles. Only the o/w emulsions are suitable for lipophilic substances encapsulation in aqueous medium. They consist of two immiscible liquids of which one is dispersed as small spherical droplets (diameter < 100 nm) in the other. Nanoemulsions could be prepared from oil and water only without using a surfactant. However, the resulting system would be very unstable and would end up into droplet coalescence; hence, the use of a surfactant not only could facilitate nanoemulsions formation but also could ensure its kinetic stability during storage [82].

When nanoemulsions are produced by the PIT method and exposed to temperature cycling, they display a very high stability. This one could be accounted for by the thick interfacial layer potentially created with the temperature cycling process. During this process, the surfactant is forced to overconcentrate at the interface, likely resulting into droplets with an overconcentrated interfacial zone. In the case of lipid-nanocapsules, this thick layer is reinforced with the neutral phospholipidic framework, therefore creating a strong core-shell around the droplets that hinders any oil diffusion across the interface [75,83].

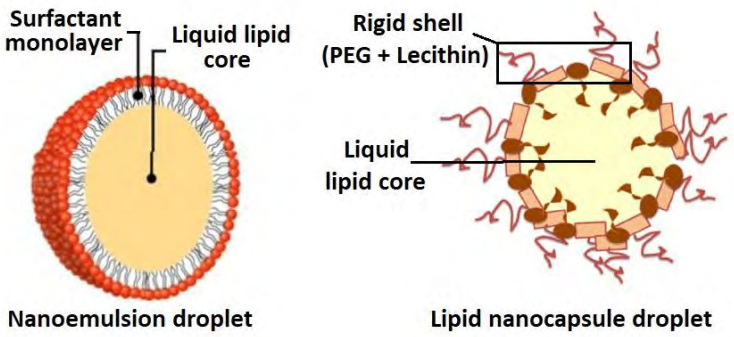

Figure 9. *Illustration of nanoemulsions and lipid nanocapsule droplets, adapted from Balamurugan et al.* [84] *and Eissa et al.* [85].

1.2.5. Characterization

Once manufactured, LNC are characterized for their various physicochemical properties, the most evaluated being their particles size, shape and morphology, their size distribution (polydispersity), their surface charge (Zeta potential), the chemical composition, their phase behaviour (polymorphism), their encapsulation efficiency as well as their in vitro drug release ability. A large number of characterization techniques used for this purpose are summarized in table 3; and a brief explanation of the most commonly used is given below.

Table 3. *LNC properties with their respective characterization techniques*

	Parameter	**Techniques**
1	Particle size	Dynamic Light Scattering (DLS)
2		Microscopy: Transmission Electron Microscopy (TEM), cryogenic-TEM (Cryo-TEM), Atomic Force Microscopy (AFM)
3	Zeta potential/Surface charge	Dynamic Light Scattering (DLS)
4	Particle shape/morphology	Microscopy: Transmission Electron Microscopy (TEM), cryogenic-TEM (Cryo-TEM), Atomic Force Microscopy (AFM)
5	Phase behaviour	X-ray Diffraction (XRD)
		Differential Scanning Calorimetry
		Thermogravimetric Analysis
6	Chemical composition	Fourier-Transform Infrared Spectroscopy (FTIR), Energy Dispersive X-ray Spectroscopy (EDS)
7	Encapsulation efficiency and Drug release	Dialysis technique followed by drug quantification using techniques like UV-vis spectroscopy, High Performance Liquid Chromatography (HPLC) etc.

1.2.5.1. Dynamic Light Scattering

Dynamic light scattering (DLS), also known as photo correlation spectroscopy or quasi-elastic light scattering, is an established and precise physical technique that measures particle size distributions ranging from less than a nanometer up to several microns. DLS is based on Brownian motion consisting of a random movement of particles resulting from their collisions with solvent molecules. According to the Brownian motion of particles, smaller particles move or diffuse faster than large ones in a liquid[86,87]. The size distribution is obtained through the information on the diffusion speed contained in the light scattered by particles. Indeed, this is well expressed by the Stokes-Einstein relationship, which states that the diffusion coefficient of particles is inversely proportional to the hydrodynamic diameter (Equation 1). The latter is defined as the size of a sphere scattering at the same speed as the measured particle [86,87].

Equation 1. *Stokes-Einstein relationship:*

$D = \frac{KT}{3\pi\eta dp}$ (**Eq. 1**), where D = diffusion constant, K = Boltzmann constant, T = absolute temperature, η = viscosity and dp = hydrodynamic diameter.

DLS technique has many advantages. Besides being a non-destructive technique that requires small amount of sample, DLS analysis can be performed with a wide range of sample buffer, temperature and concentrations [86].

1.2.5.2. Transmission Electron Microscopy

Transmission Electron Microscopy (TEM) has emerged as a powerful tool for the characterization of nanoparticles. Unlike light microscope, TEM uses electron as source of illumination. Given the short wavelength of the electron beam, which is 100,000 folder shorter than photons, TEM can achieved very high resolution in the sub-nanometer scale of nearly 0.2 nm in conventional TEM. The beam of electrons that is produced is transmitted through the liquid sample spotted onto a copper grid to form an image. Hence, TEM provides direct and clear visualization of nanoparticles, including lipid nanocapsules (LNC). Under TEM, LNC appear as black spherical or ellipsoidal particles on a white background. However, in case LNC are negatively stained, for example by either uranyl acetate or phosphotungstic acid, they appear as bright spots on a black background. Since TEM allows differentiation of individual vesicles from aggregates, the LNC population can be critically evaluated [69,88].

1.2.5.3. Differential Scanning Calorimetry

Differential scanning calorimetry (DSC) is a thermoanalytical technique that allows the measurement of the heat flow into or out of a sample as function of temperature or time. Samples are placed in specialized pans made of aluminium tin, zinc or indium. The DSC analysis can be performed on two principal types of instruments. This can be either heat flux DSC, which measures the difference in heat flow between the sample and a reference as a function of temperature or time, or power differential DSC, which measures the difference in power supplied to the sample and a reference. Both the sample and reference are subject to nearly the same heating, cooling and isothermal treatment throughout the experiment that takes place in a controlled atmosphere (nitrogen gas). Frequent electric power electric power adjustments happen upon material phase transition either melting or crystallization, described and expressed by the heat flow curve. This one consists of the plot of heat capacity against temperature or time. Thanks to the transition temperature or enthalpy provided by the heat flow curve, the nature of thermal events can be identified and is either endo or exothermic [89–91].

A large number of properties of sample can be determined using DSC, including fusion and crystallisation events, glass transition and so on. While crystallisation is an exothermic process resulting from the transition from amorphous solid to crystalline solid, the fusion or melting point of a sample results into an endothermic peak in the DSC curve. Given its ability to determine transition temperatures and enthalpies, DSC turns out to be a valuable tool in producing phase diagrams for lipid nanoparticles as well as other compounds [92].

1.2.5.4. X-ray Diffraction

X-ray diffraction (XRD) is a well established non-destructive technique used to elucidate the crystallographic structure of a material. XRD is based on Bragg's law ($n\lambda = 2d \sin\theta$) and works by irradiating a material with incident monochromatic beam of x-rays followed by measurement of the intensities and scattering of angles of the x-rays that leave the material [93,94]. Generally, the x-ray diffractometer operates at determined voltages and current and uses CuKα x-rays (λ = 0.150406 nm) as source of radiation, over the 2θ range (10 to 100 degrees). While broad peaks are the expression of amorphous regions of the samples, crystalline regions are expressed by sharp peaks [95].

In addition to crystallization, XRD provides information on structures, phases, preferred crystal orientations and other structural parameters like average grain size, strain and crystal defects. XRD technique encompasses single crystal XRD and powder XRD, the latter being the one that applies to lipid nanoparticles or hydrogels as it offers the advantage of characterizing both the starting materials and the end products with detailed qualitative presentation of their microstructural behaviours [89,96].

1.2.5.5. Energy Dispersive X-ray Spectroscopy

Energy Dispersive X-ray Spectroscopy (EDS, EDX or XEDS) is an analytical technique used to elucidate the surface chemical or elemental composition of sample. During the analysis, an electron beam of 10 to 20 Kev strikes the sample and triggers x-ray emission from it, which is the expression of the difference in energy between the higher energy shell and the lower energy shell. Thereafter, the energy-dispersive spectrometer allows the measurement of the energy emitted by an x-ray, which is characteristic of the difference in energy between the two shells and of the atomic structure from which they were emitted. This elemental composition relies on the fundamental principal that each element has a unique atomic structure that allows unique sets of peaks on its x-ray spectrum [97–99].

1.2.6. Applications

Lipid nanocapsules are used for the encapsulation of a wide variety of drugs, including anti-infective agents, anti-cancer agents, active ingredients used for the central nervous system, etc. These drugs can be lipophilic or hydrophilic, meaning that they can be soluble in the fat phase or the aqueous phase, respectively [67]. LNCs are promising vectors for the delivery of these therapeutic molecules by different routes, including oral, intravenous, dermal, cerebral, pulmonary, etc. [100].

A group of researchers demonstrated that LNC could allow some drugs to cross the blood-brain barrier, such as hyperforin, a natural antidepressant whose LNC formulation has been shown to block calcium (Ca^{+2}) channels in cultured cortical neurons, inhibiting the release of neurotransmitters and thus alleviating depression [101]. Other drugs such as Ibuprofen, Gemcitabine, Paclitaxel, Acriflavine etc. have been successfully formulated in LNC with promising clinical applications [102–106].

1.3. Lipid nanoparticles and their hydrogel composite

1.3.1. General consideration

LNPs have shown great promise for drug delivery by different routes, except that due to the inadequate rheological properties of their aqueous dispersions, they are hardly applicable to dermal, transdermal, ocular, mucosal and transmucosal routes. To circumvent this problem, LNPs could be converted into hydrogel composites resulting in semi-solid formulations capable of providing spatial and temporal control of the release of active ingredients in these difficult routes of administration [107].

1.3.2. Hydrogels

Hydrogels are three-dimensional networks of polymers. Although not soluble in water, they are highly absorbent while maintaining their physical integrity. The presence of hydrophilic functional groups like amide, amino, carboxyl and hydroxyl groups that are attached to the polymeric chains of hydrogels could explain their ability to retain large amount of water [108]. Due to their properties such as flexibility, biocompatibility, biodegradability, non-toxicity and ability to absorb a lot of water, hydrogels have attracted a lot of interest for many applications in medicine. These include applications in contact lenses, in wound dressing, in biosensors, in drug delivery, in tissue engineering etc. [109,110]. The key parameters that influence the porosity and the degree of swelling of hydrogels include the degree of cross-linking, the concentration and the nature of polymers that either natural or synthetic. Among them,

hydrogels porosity and degree swelling control the passive diffusion kinetics of active molecules, biomolecules, or nanoparticles that are entrapped inside the scaffold [111–113].

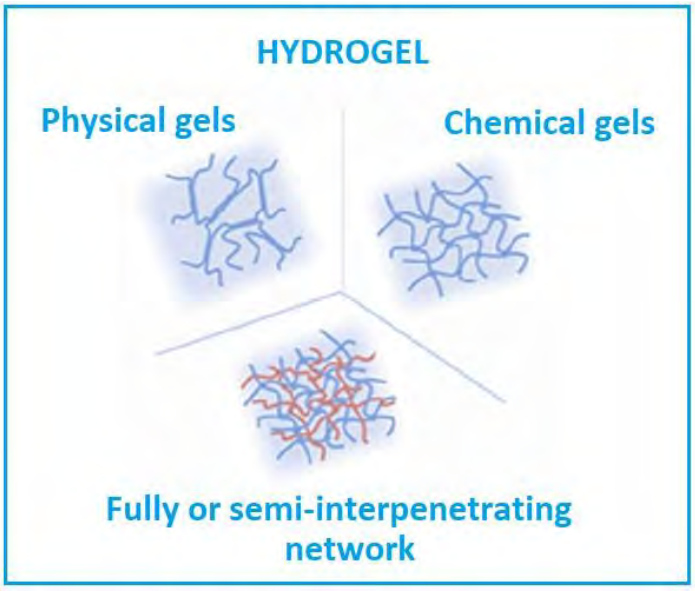

Figure 10. *Schematic representation of hydrogel entanglements depending on the type of cross-linking. Photo adapted from Desfrançois et al.* [107].

1.3.2.1. Classification of hydrogel

Hydrogels are classified based on the source of polymers, ionic charge, polymeric composition, physical properties, degradability, cross-linking techniques, and response to the environment [112].

As far as the classification based on the source of polymers is concerned, hydrogels are either natural or synthetic depending on whether the polymers used to design them are natural or synthetic. Among natural polymers, polysaccharides are the most used given their many advantages such as water solubility, high swelling capacity, biocompatibility, biodegradability and so on. There are different polysaccharides that are used to produce hydrogels, including chitosan, carrageenan, pectin, agarose, xanthan etc. Since natural hydrogels are limited by their weak mechanical properties and since they vary depending on the batch, synthetic moieties are used to improve them [114,115].

On the other hand, synthetic hydrogels are the ones obtained from synthetic polymers. They exhibit advantages such as limited batch-to-batch variability, improved control of their matrix structure and chemical composition, ability to be tuned according to the targeted applications and requirements. Synthetic polymers mainly used to produce synthetic hydrogels include poly(N-vinyl-pyrrolidone), poly (electrolyte complexes) and poly (vinyl alcohol), poly

(hydroxyalkyl methacrylate), poly (acrylate), poly (acrylamide), poly (methacrylamide) and its derivatives, etc. [114,116]

Since synthetic hydrogels are limited by their poor biocompatibility and biodegradability at one hand and their toxic character at the other, a class of semisynthetic hydrogels (hybrid) have been developed. They are made out of natural and synthetic polymers moieties. Although they might exhibit some cytotoxicity, low biocompatibility, they combine the many advantages of both natural and synthetic hydrogels previously described [117].

Based on the electrical charge on their cross-linked chains, hydrogels are either neutral (non-ionic), ionic (cationic hydrogels such as the ones based on poly (lysine), poly (amido-amine) and anionic hydrogels like the ones based on poy (acrylic acid) and amphoteric hydrogels[112]. On the other hand, based on the cross-linking, hydrogels are either physically cross-linked hydrogel or chemically linked ones. Physically linked hydrogels have matrix architecture formed by physical interactions with weak bonds like hydrogen ones, ionic interactions, host-guest chemistry, hydrophobic interactions, coordination bonds and $\pi - \pi$ stacking interactions. Chemically linked hydrogels have networks resulting from covalent bonds and could be obtained by either using reactive side of linear polymers or by using crosslinking agents like N,N,N',N'-tetramethylethylenediamine, N,N'-methylene bisacrylamide, glutaraldehyde etc. [118,119]

Based on their polymeric composition, hydrogels are homopolymeric, copolymeric or interpenetrating polymeric hydrogels. These ones refer to hydrogels produced using respectively a single species of monomer, two or more different monomers species and two polymers where the individual chains are entangled [112].

Based on the environmental stimulations, hydrogels are either chemically responsive hydrogels (pH-sensitive), or physically responsive hydrogels (responding to temperature, light, pressure, magnetic fields, ultrasound or electrical fields) or even biologically responsive hydrogels [120].

1.3.2.2. Preparation

Different techniques can be used to prepare hydrogels. They are either chemical or physical, depending on the type of the resulting crosslinking. Physical crosslinking techniques include ionic interaction, complex coacervation, maturation (heat-induced aggregation), freeze-thawing and heating or cooling of a polymer solution [112,121].

On the other hand, chemical crosslinking include crosslinking by radical polymerization, crosslinking by chemical reaction of complementary groups (ex. Crosslinking with aldehydes, by addition reaction, by condensation reaction), crosslinking by high-energy radiation, enzymatic crosslinking and grafting [112,121].

Of these techniques, grafting is the most used and it consists of attaching monomers onto the backbone of a pre-formed polymer either natural or synthetic. Briefly, in order to generate radicals, the polymer chains are activated either chemically by use of chemical reagents known as initiators (e.g. ammonium or potassium persulfate) or by radiation that consists of using high-energy radiations like gamma and electron beam radiation as initiators to activate the macromolecular backbones. Once the polymer chains are activated, the monomers attachment follows and their functional growth results into branching and crosslinking [112,121].

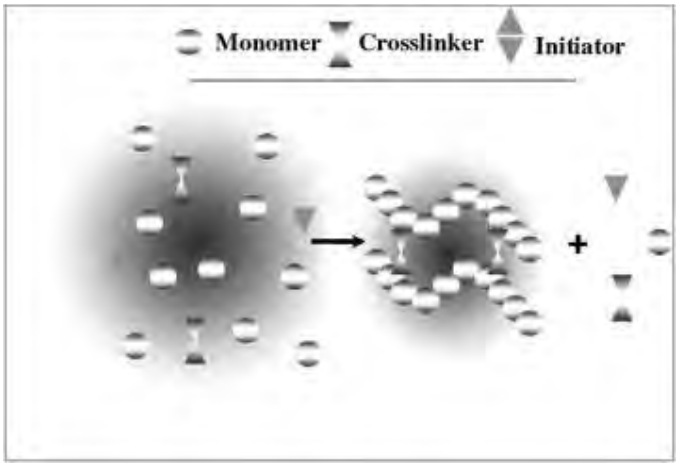

Figure 11. *Schematic illustration of hydrogel preparation showing how monomer and crosslinking agent combine to form hydrogel scaffold after initiation. Photo credit to Ahmed* [112].

1.3.2.3. Characterization of hydrogels

Once synthesized, hydrogels are subject to characterization for their physicochemical properties. The most evaluated physicochemical properties of hydrogel include their water content, phase behaviour (polymorphism), chemical composition, mechanical properties, surface morphology, encapsulation efficiency and drug release ability. Commonly utilised techniques to assess these parameters are presented in table 4 [112,122].

Table 4. *Hydrogel properties with their respective characterization techniques*

	Parameter	**Technique**
1	Phase/Thermal behaviour	X-ray Diffraction (XRD)
		Differential Scanning Calorimetry
		Thermogravimetric Analysis
2	Chemical composition	Fourier-Transform Infrared Spectroscopy (FTIR),
		Energy Dispersive X-ray Spectroscopy (EDS)
		Nuclear Magnetic Resonance Spectroscopy (solution NMR and ssNMR)
3	Surface morphology	Scanning Electron Microscopy
4	Mechanical properties	Dynamic Mechanical Analysis (DMA)
5	Water content	Swelling capacity (teabag, filtration and sieves methods)
6	Encapsulation efficiency and Drug release	Dialysis technique followed by drug quantification using techniques like UV-vis spectroscopy, High Performance Liquid Chromatography (HPLC) etc.

a) Swelling studies

Since hydrogels are defined as polymeric networks with the ability to absorb and hold significant amount of water without dissolving in it, one of the most critical properties to determine is the fraction of water absorbed. This study is carried out using dried hydrogel known as xerol, which is allowed to swell in water followed by determination of the swelling ratio or swelling capacity. This one is defined as the amount of water in gram contained in one gram of xerogel and is expressed in g/g or in percentage of swelling ratio (%SR). The teabag method, the sieves method and the filtration method can be used to determine this parameter[123].

e) Scanning Electron Microscopy

Scanning electron microscopy (SEM) is a microscopic technique that allows morphological characterization of materials such as hydrogels by scanning their surface with focused beam of electrons. Unlike TEM in which the electron beam passes through the sample to create a 2D image, in SEM, the electrons interacting with atoms in the samples are reflected and detected by the instrument, therefore providing information about the surface topography of the sample, which is expressed as a 3D image [124].

Morphological characterization of hydrogels is very essential as it allows highlighting critical their physical properties, including shape, porosity, pore size, size distribution or pores and wall

thickness, which vary depending on the method used to produce hydrogels (physical, chemical or radiation-induced cross-linking), which can be tuned according to the targeted application. Although the risk of collapse of pore structure during dehydration makes difficult the morphological analysis of hydrogel, SEM analysis has been demonstrated to provide good image with resolution of about 10 nm. SEM analysis is carried out under a high vacuum and requires prior lyophilisation of the sample [124,125]

f) Nuclear Magnetic Resonance Spectroscopy

Nuclear magnetic resonance spectroscopy analysis of hydrogels has attracted interests of researchers in recent years given its ability to elucidate polymeric structural properties and physical processes. Hence, thanks to chemical shift and peak intensities of simple spectra, structural properties like the polymer composition, the tacticity and the sequence distribution can be determined. Moreover, NMR analysis allows resolving the structure, degree of grafting, molecular organization, water-biopolymer interactions and internal dynamical behaviour of hydrogels [126].

NMR is based on the absorption of electromagnetic radiation in the radiofrequency region 4 to 900 MHZ. It exploits the transition in nuclear spin states. Indeed, given that many nuclei have spin and are all electrically charged, they are prone to energy transfer when external magnetic field is applied and could therefore have two possible nuclear spin energy states. This transfer of energy occurs from a lower to a higher energy level and takes place at a wavelength corresponding to radio frequencies. Once the spin goes back to its base level, emission of energy occurs at the same frequency. The NMR instrument produces the spectrum by measuring and processing the signal that corresponds to the energy transfer that has occurred. Both solution NMR and solid-state NMR spectroscopy are the NMR techniques used for hydrogels characterizations [126–129].

1.3.3. Hydrogels as lipid nanoparticles scaffold

Lipid nanoparticles as already described, provide many advantages when applied to drug delivery. They have also been shown to achieve prolonged release of encapsulated drugs. However, when applied to mucosal, dermal, transdermal or ocular drug delivery, they need to be supported by a three-dimensional network to remain at the administration site. Hence, LNP-hydrogel composite has been developed for this purpose, yielding advantages of both LNP (enhancement of solubility, permeability, bioavailability and protection of the drug from degradation) and hydrogels (mucoadhesion, biocompatibility, good rheological properties etc.).

This composite allows circumventing the incompatibility between hydrophobic drugs and the water-swollen hydrogel matrix as double encapsulation is achieved by first encapsulating the drug in LNP, themselves loaded in the hydrogel scaffold [107].

Researchers have investigated different types of polymers to produce hydrogel scaffold for LNP. The majority of them belong to the following polymer families: poly (acrylic) acid polymers (e.g. Carbopol®), poloxamers (e.g. Pluronic®), polysaccharides (e.g. cellulose, carrageenan, chitosan etc.). All of them are biocompatible. Poly (acrylic) acid polymers based hydrogels form as a result of entangled chains while hydrogels formed from poloxamers are a result of physical interactions. On the other hand, polysaccharides based hydrogels are mostly a result of chemical crosslinking [107].

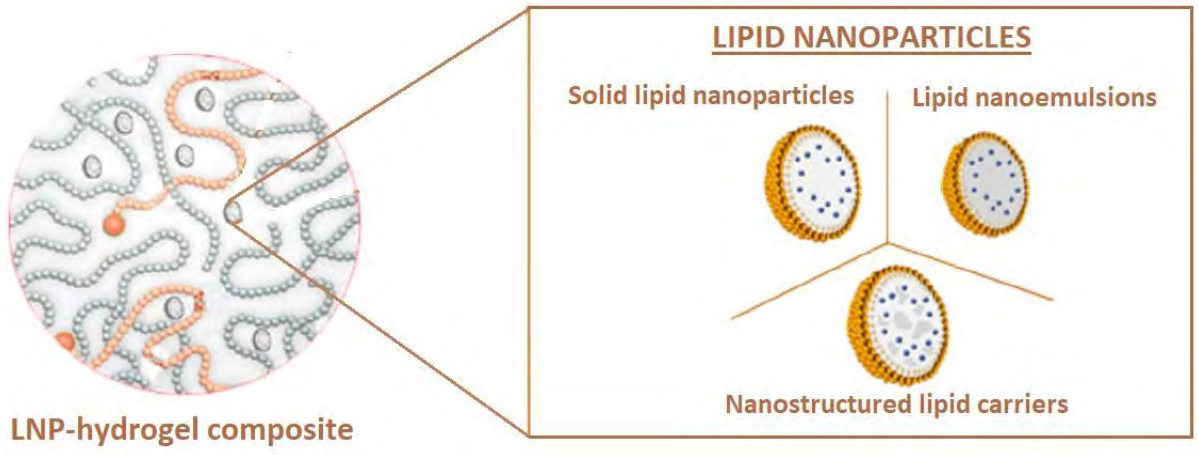

Figure 12. *Schematic representation of Lipid nanoparticles-hydrogel (LNP-hydrogel composite) composite illustrating LNP entrapped within the hydrogel structure. Photo adapted from Desfrançois et al.* [107].

1.3.3.1. Preparation of LNP-hydrogel composites

The preparation of LNP-hydrogel composites depends on the type of polymer used to produce the hydrogel.

a) Preparation based on physical interactions

Poly (acrylic) acid hydrogels and poloxamers based hydrogels are the most used to prepare LNP-hydrogel composites using this method, since their gelation process is based on physical interactions. Briefly, an aqueous solution containing a determined amount of LNP dispersion, and the polymer is stirred for homogenisation. To obtain the LNP-hydrogel composite, if the polymer used is the poly (acrylic) acid (Carbopol ®), the homogenized mixture pH should be adjusted to the ideal Carbopol ® gelation pH, which in most cases ranges from 6 to 8, as indicated by the supplier. On the other hand, when poloxamer is the polymer used, its aqueous

mixing with the LNP dispersion is done at low temperature (around 4 to 10°C) to avoid early gelation. After homogenisation, the mixture is progressively brought back to room temperature [107].

b) Preparation based on chemical interactions

This preparation consists of synthesizing hydrogels prior to mixing them with the LNP dispersion. Hydrogels are chemically synthesized using any of the methods previously mentioned in section 1.3.2.2. Most of the LNP-hydrogel composites preparations based on chemical interactions are performed using polysaccharides as polymers, given their incredible biological activities and high biocompatibility. For example, chitosan-based hydrogel can be synthesized by free radical polymerization by using a monomer such as acrylic acid, a crosslinking agent such as methylene bisacrylamide (MBA) and an initiator such as ammonium persulfate. Once synthesized and washed by an organic solvent such as methanol or acetone, the dried hydrogel will be mixed with the LNP dispersion to yield the LNP-hydrogel composite [107,112].

1.3.3.2. Types of LNP-hydrogel composites

a) LNP-poly (acrylic) acid-based scaffolds

Synthetic anionic poly (acrylates) (Carbopol ®) with a high molecular weight represent 26% of the hydrogels used to shell LNP. Carbopol ® based hydrogels are obtained by neutralizing the solid powder up to pH ranging from 5.7 to 7, to release the alkali ions bound to the carboxylic moieties. The addition of electrolytes such as NaOH is usually performed. However, in the case of LNP-hydrogel composites, their use could lead to LNP aggregation. Hence, non-ionic neutralisers like triethanolamine or ehtylenediamine can be used as an alternative [130,131].

b) LNP-poloxamer based scaffolds

Poloxamers (poloxamer 188 known as Pluronic ® F68 and poloxamer 407 known as Pluronic ® F127) are used to produce thermos-responsive hydrogels thanks to their thermos-reversible gelation process at specific concentration and temperature Hence, LNP-poloxamer composites have been investigated for sensitive delivery routes like the injectable, ocular or rectal routes [132–135].

c) LNP-polysaccharides based scaffolds

Polysaccharides have attracted attention and interest of many researchers thanks to their numerous and incredible properties yielding different medical applications. These properties include easy accessibility, biocompatibility, mucoadhesiveness, biodegradability, high affinity

toward water and ability to undergo diverse chemical modifications. Polysaccharides consist of long chains of monosaccharide units that are linked together by glycoside bonds. Since polysaccharides hydrogels have poor mechanical properties, are fragile and degrade at physiological pH when in their natural state, their backbone is mostly modified or they are combined with other synthetic polymers. Chitosan, cellulose and xanthan are the three most used polysaccharides to produce LNP-polysaccharide hydrogel composites [107,136].

Different works have reported successful formulations of LNP-polysaccharide composites. This is the case for Topotecan based NLC-Hydroxyethylcellulose; Copaiba oil based LNE-hydroxyethylcellulose; Avanafil based SLN-hydroxypropylmethylcellulose; Nitrendipine SLN-chitosan; ketoconazole SLN-dextran; siRNA carried by chitosan-transacylated LNC, etc. NLC, LNE, LNC and SLN respectively refer to nanostructured lipid carriers, lipid nanoemulsions, lipid nanocapsules and solid lipid nanoparticles [107,137].

1.3.3.3. Characterization of LNP-hydrogel composites

Due to the recent emergence of this domain, through characterization of LNP-hydrogel composites is still very rare. However, like hydrogels and nanoparticles, they can be characterized for some physicochemical properties such as phase behaviour (polymorphism), chemical composition, mechanical properties, surface morphology, encapsulation efficiency and drug release ability.

1.4. Pulmonary delivery

Given the very interesting features of the lungs responsible of their ability to absorb drugs either for local or for systemic delivery, pulmonary delivery systems have been intensively investigated and turned out to be very promising biomedical assets. Indeed, pulmonary route is seen as non-invasive administration pathway that could allow local and systemic delivery of therapeutic agents due the very large absorption surface and permeability of the lungs as well as good blood supply. Pulmonary delivery is associated with the advantage of having low enzymatic activity, of providing rapid absorption of drugs and of avoiding first-pass metabolism. In short, three main benefits of pulmonary delivery may be achieved, namely a rapid onset of action, high local concentration, and needle-free systemic delivery of drugs with poor oral bioavailability. Thanks to these interesting properties of the lungs, local respiratory diseases (e.g. asthma, pulmonary fibrosis, pneumonia, lung cancer, infectious diseases like tuberculosis, covid-19 etc.), along with some systemic diseases could be effectively treated by using pulmonary delivery system [138,139].

1.4.1. Pulmonary system description

As illustrated in Figure 12 the pulmonary system is made of two main pulmonary structures: an upper one and a lower one. This system plays a very critical double role in the human body that consist of oxygen supply and carbon dioxide clearance. While the nose, the nasal cavity and the pharynx (nasopharynx, oropharynx and laryngopharynx) constitute the upper structures, the lungs represent the lower structures and are made of the larynx, trachea, carina, bronchi, bronchioles and alveoli. Thanks to the mucous membranes present in the upper structures, foreign particles like smoke and other pollutants are filtered out before the air reaches the lungs. These upper structures also heat up and humidify the air that is inhaled [140].

The role of the lower airway is to pull in air from the upper structures and allow absorption of oxygen in exchange of carbon release in the alveoli. This phenomenon is referred to as ventilation, which consists of the exchange of air between the atmosphere and the alveoli during inhalation and exhalation; and diffusion that consists of oxygen and carbon dioxide exchange through the respiratory membrane from area of high to low pressure [140,141].

It is worth mentioning that the surface of these different airway structures is covered with mucus-laden cilia which play a very important role in cleaning the airways by a process known as mucociliary clearance. These cilia transport inhaled dust particles and microbes in the airways to the upper parts of the respiratory system for removal either by coughing, sneezing, spitting or swallowing. This clearance process is known to be one of the main innate defence mechanisms that protect the lungs from biological inert, irritating and suspended particles in the air [141].

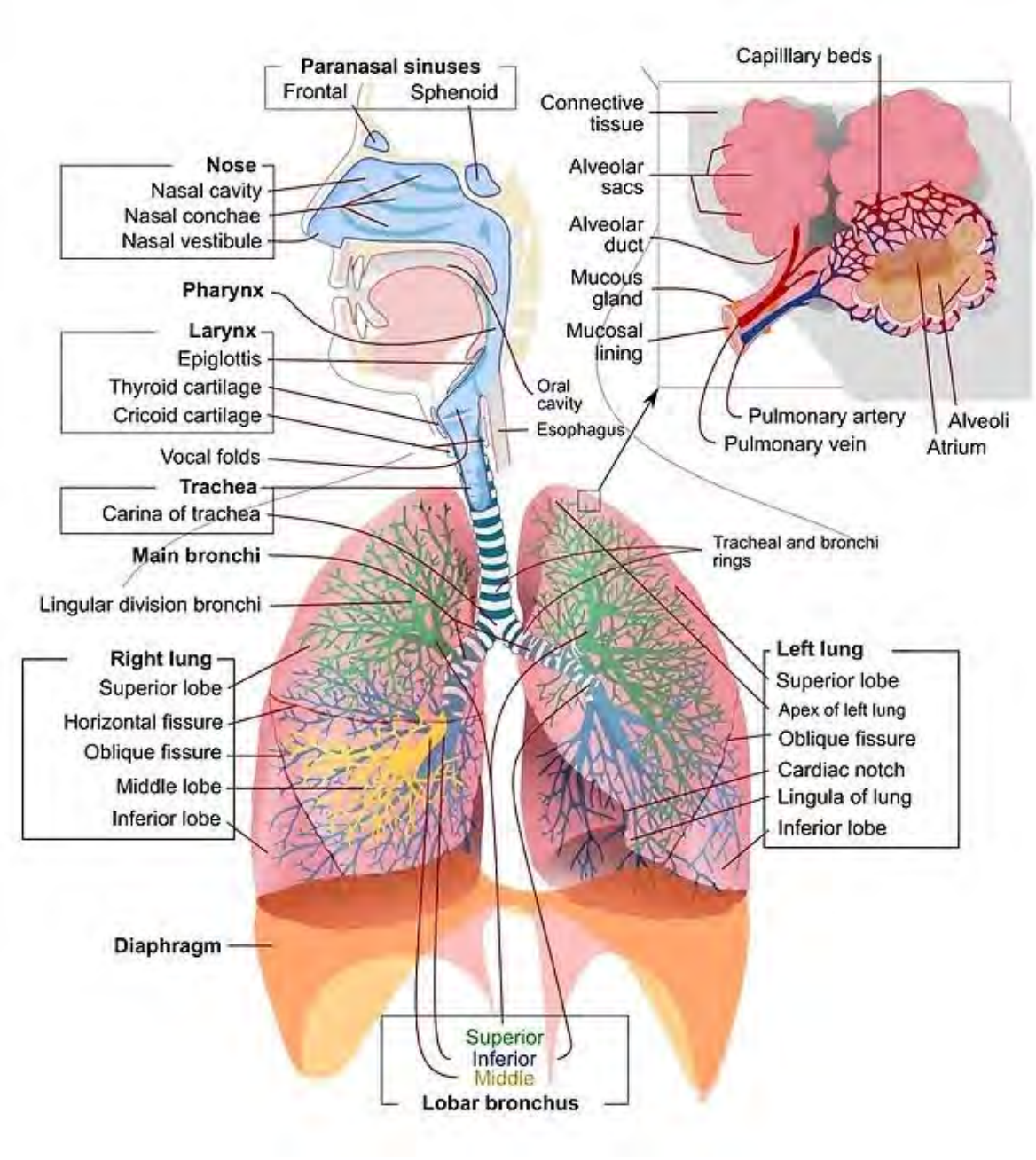

Figure 13. *Anatomical schema of the human respiratory system.*

https://www.redbubble.com/fr/i/impression-rigide/Diagramme-du-syst%C3%A8me-respiratoire-humain-par-allhistory/30345034.7Q6GI (Accessed in June 18, 2022).

1.4.2. Influence of the lung architecture on drug delivery

Among the different parts of the lungs, the alveolar region of the deep lung presents the largest surface area and thinnest diffusion pathway for dissolved material, which makes it the first target for drug delivery. When delivered via inhalation, hardly greater than 20% of the drug reaches the alveoli as large amount of it may deposit within the airways ducts and subsequently be moved away by mucociliary escalator [142]. However, the physiological effectiveness of

inhaled particles depends on their ability to deposit within the respiratory system. Factors that contribute to inhaled particle deposition include particle size, shape and density, airflow velocity and volume, physiological variations between patients, and pause time between inhalation and exhalation [143].

Generally, there are three main physical mechanisms of particle deposition, which are determined by both aerodynamic diameter and inhalation flow dynamics. They include impaction by inertial forces, electrostatic deposition and interception; sedimentation by gravitational forces; and diffusion by Brownian motion. Particles with size greater than 5 µm are subject to impaction while sedimentation typically influences particles with size between 1 and 5 µm. Particles with size ranging from 0.5 to 1 µm undergo deposition by diffusion [144–148].

On the other hand, inhaled particles are also prone to elimination by the various clearance mechanisms present in the respiratory system, including the mucociliary or cough clearance to the gastrointestinal tract, the passive or active absorption into the capillary blood network and the metabolism. Poorly soluble particles hardly diffuse toward the cell layer and can therefore be cleared to the gastrointestinal tract by mucociliary escalator or cough; they can also be passively or actively absorbed into the capillary blood network or metabolized in the mucus or lung tissue [142]. Inhaled particles are also prone to alveolar macrophage uptake. Indeed, the air surface of each alveolus is often cleared by about 12 to 14 macrophages that phagocytize any insoluble particle in the alveolar region [149]. The understanding of these clearance mechanisms is very important as it can inspire and guide researchers about how they can deal with pulmonary drug delivery.

1.4.3. Overcoming pulmonary clearance mechanisms for successful drug delivery

As explained in previous sections, one of the biggest challenges to overcome the pulmonary delivery system is the inhaled particles deposition, which is influenced by many factors among which the size of particle plays a great role. Hence, modifying the aerodynamic diameter (d_a) of the particle can prevent its clearance from the airways. Generally, small particles with d_a < 0.5 µm are easily cleared away while particles d_a above 10 µm are easily deposited into the proximal airways including the mouth, throat and larynx [150]. Moreover, particles with d_a of 1 to 5 µm can be deposited in the alveolar airspaces and are generally considered as optimal design for pharmaceutical inhalation and therapeutic approaches within the lungs. To date, different drug carriers have already been studied to improve the controlled release of drug in

the pulmonary system. They mainly include liposomes, biodegradable polymeric microparticles and hydrogels, as described in table 5 [151].

Table 5. *Drug delivery system available for pulmonary delivery*

	Delivery system	**Characteristics**	**Materials**
1	Liposomes	Amphiphilic Biocompatible and biodegradable Targeting potential and ease of functional modification Tolerable and safe	Egg phosphatidyl choline and cholesterol, soybean phosphatidylcholine, hydrogenated soyaphosphatidylcholine and hydrogenated soyaphosphatidyl glycerol
2	Biodegradable polymeric microparticles	Biocompatible and biodegradable Slower release rate and longer duration of action; release rate controllable Decreased particle clearance from phagocytosis	Albumin Sebacic acid Poly(ether-anhydrides) Poly(lactide and/or glycolide) Poly(lactic-co-glycolic acid) PEG 1,3-*bis*(carboxyphenoxy)propane
3	Hydrogel	Swellable Evade alveolar macrophage uptake Biocompatible and low toxicity	Natural polymers: chitosan, alginate, collagen, gelatin, hyaluronic acid and dextran Synthetic polymers: hydroxyethylmethacryate, vinyl acctate, *N*-(2-hydroxy propyl) methacrylate

1.5. Problem Statement

Covid-19 is a deadly viral disease that has been killing millions of people since 2019. According to the latest reports, more than 500 million people have been infected so far and over 6 million have died from the disease. A highly contagious virus called sars-cov-2 has been identified as the cause of Covid-19. To date, no effective treatment has been fully approved to combat the disease and researchers are still working to find one. However, recently, an mRNA-based vaccine has been introduced and approved for use in humans, raising hopes of eliminating the threat of the virus. Unfortunately, despite the hope for the vaccine, cases of covid-19 and deaths are still recorded even among those vaccinated. On the other hand, older antiviral drugs are being screened for their ability to inhibit the life cycle of the sars-cov-2 virus so that they can be used to treat covid-19. This is the case of Remdesivir, formerly developed against the ebola virus, which has received urgent approval for use in humans against covid-19.

Although effective in treating viral infections, antiviral drugs are susceptible to resistance and ineffectiveness. According to the biopharmaceutical classification system, about 90% of existing and upcoming antivirals are characterised by poor solubility or permeability. This results in the use of large amounts of drug to reach the therapeutic dose in the bloodstream, which exposes the patient to dangerous side effects.

Since the lungs are the most affected by sars-cov-2, this project aims at developing a pulmonary drug delivery system capable of achieving both successful local and systemic release of potential anti-covid-19 drugs. The lungs features provide a large surface area for absorption, a high potential drug permeability and no first-pass metabolism making them a very promising drug delivery pathway. While soluble particles in the mucosal matrix diffuse rapidly into the epithelial lining fluid and are readily absorbed, poorly soluble particles are likely to be removed naturally by mucociliary escalator, coughing and/or phagocytosis by alveolar macrophages impeding successful drug delivery.

Recent advances in nanotechnology research have identified several strategies to overcome such drawbacks, among which the loading of antiviral drugs into advanced delivery systems has attracted great interest and shown promising results [152–155]. Among them, lipid-based delivery systems have revived many drugs belonging to BSC classes II, III and IV by enhancing and improving both their solubility and permeability. There are many types of lipid-based delivery systems, including liposomes, microemulsions, nanoemulsions, nanostructured lipid carriers, etc. [152]. Interestingly, up to now some antiviral drugs have successfully reached the market as lipid-based formulations. This is the case for amprenavir (Agenerase®), saquinavir (Fortovase®), and ritonavir (Norvir®) [156].

Hence, the first goal of this work is to develop lipid-nanocapsules (LNCs) to improve biopharmaceutical properties of potential antivirals against sars-cov-2 by using Efavirenz as a drug model. Efevirenz is a non-nucleoside reverse-transcriptase inhibitor (NNRTI), used, in combination, for first line treatment of HIV and recently investigated for its potential activity against sars-cov-2 [62,65]. On the other hand, LNCs are lipid-based drug delivery systems introduced by Heurtault et al., in 2002 who reported them to be very stable systems with particle size below 100 nanometers depending on their components proportions. LNC are produced easily by using a low energy organic solvent-free method named phase inversion as developed and explained in previous studies[69,75]. Their structure consists of an oily liquid core surrounded by a rigid shell, suggesting that they are a suitable vehicle for efavirenz due to its

log P of 4.6 [157–159]. Furthermore, labrafac® lipophile 1349, lipoid® S75-3 and solutol® HS15 are the main components used to manufacture LNCs. In this work, it is planned to use different materials namely medium chain triglycerides from coconut and palm kernel oil, crude soy lecithin and tween 80, in order to make LNCs more affordable for low-income countries. In addition, as far as we know, this will be the first time that these materials have been used to develop lipid nanocapsules.

However, due to their small particle size, LNCs do not achieve good residence time when applied to pulmonary delivery. As they cannot be easily deposited in the alveolar region, they are likely to be phagocytised by alveolar macrophages or exhaled out of the airway. Therefore, the efficacy of the drug is not achieved or is only possible by using very high concentrations of the particles and by increasing their frequency of administration, which exposes to drug toxicity.

Latest research into pulmonary delivery systems has shown that hydrogels have the potential to overcome the deposition problems observed in this route of administration. Hydrogels are three-dimensional polymeric matrix networks that absorb a large amount of water and have interesting properties, including bioadhesivity, biodegradability, low toxicity and low interfacial tension, which make them excellent candidates for drug delivery to the lungs. The mucus lining the airways of the lungs has wettability and stickiness properties that are, interestingly, similar to the surface characteristics of hydrogels. As hydrogels are mucoadhesive, their contact or interaction with the mucus layer is likely to increase the residence time of the drug formulation in the lungs as well as achieve sustained release. In addition, due to their swelling ability, hydrogels can prevent or delay engulfment by macrophages. In addition, they are also known to exhibit certain biological activities such as antibacterial and antiviral activities.

Therefore, the second objective of this work is to synthesise highly swellable hydrogel scaffolds capable of encapsulating Efavirenz-based LNCs and allowing their pulmonary delivery. To achieve this objective, natural polymers will be used. These include iota-carrageenan (iCar) and chitosan (CS). Recent *in vitro* studies and *in silico* analysis have respectively shown that iCar has inhibitory activity against sars-cov-2 and shows promising inhibitory potential against the main sars-cov-2 protease (MPro). Therefore, the resulting hydrogel of this study would not only enable successful drug delivery, but also intrinsically combat sars-cov-2 virus.

1.6. Aim and objectives of the research

The aim of this study was to design, synthesize, manufacture, characterize and evaluate lipid nanocapsules and their hydrogel composite for pulmonary delivery of potential anti-covid-19 drugs.

Two main projects were designed from the general aim of this research in terms of two main specific objectives, which were:

1. To design, manufacture, characterize and evaluate lipid nanocapsules (LNC)

— Use of Efavirenz (EFV) as drug model of poor water-soluble drugs and evaluate its solubility in LNC starting material (namely oils likely to be used in their composition);
— Optimization of LNC formulation using phase inversion;
— Building polynomial models capable of predicting LNC properties, namely the droplet size, the polydispersity index and the Zeta potential, by using Design Expert Software version 13;
— Characterization of LNC for their droplet size, polydispersity index and Zeta potential; for their chemical composition, thermal and phase behaviour, as well as for their shape and morphology;
— Evaluation of LNC encapsulation efficiency as well as their drug release ability;
— Evaluation of LNC stability over 28 days of storage.

2. To design, synthesize, manufacture, characterize and evaluate LNC-hydrogel composite

— Synthesis by free radical copolymerization of hydrogel using chitosan and iota-carrageenan as polymer backbones, acrylic acid and acrylamide as monomers, N'N'Methylene bisacrylamide as crosslinking agent and ammonium persulfate as the initiator, to the "chitosan-g-iota carrageenan-g-poly (acrylamide-co-acrylic acid) hydrogel" (CS/iCar-p(AAm-co-AA));
— Evaluation and optimisation of CS/iCar-p(AAm-co-AA) swelling capacity, by building up a mathematical model for its prediction;
— Preparation of EFV-LNCs-CS-iCar-p(AAm-co-AA) hydrogel composite;
— Characterization of both CS-iCar-p(AAm-co-AA) hydrogel and EFV-LNCs-CS-iCar-p(AAm-co-AA) hydrogel composite for their chemical composition, phase behaviour, thermal decomposition profile as well as for their surface morphology;
— Evaluation of encapsulation efficiency of LNC entrapped in CS-iCar-p(AAm-co-AA) hydrogel as well as EFV drug release profile from the double encapsulation system.

Chapter Two

Materials and Methods

Project I: "Design, Manufacture, Characterization and Evaluation of Lipid Nanocapsules to Enhance the Biopharmaceutical Properties of Efavirenz

***Mukubwa, G.K.**; Safari, J.B.; Walker, R.B.; Krause, R.W.M. Design, Manufacturing, Characterization and Evaluation of Lipid Nanocapsules to Enhance the Biopharmaceutical Properties of Efavirenz. Pharmaceutics* **2022**, *14, 1318. https://doi.org/10.3390/pharmaceutics14071318*

The above paper published in Pharmaceutics reports most of the results obtained in this first project

2. MATERIALS AND METHODS

2.1. Materials and Methods for Project I

2.1.1. Materials

2.1.1.1. Chemical

Crude soy lecithin granules were purchased from Health Connection Wholefoods (Cape Town, South Africa). According to the manufacturer's specifications, these granules mainly contained phosphatidylcholine, phosphatidylinositol, polyunsaturated fat, saturated fat, glycemic carbohydrates and sodium. MCT oil was obtained from Absolute Organix (Johannesburg, South Africa), Labrafac Lipophile 1349 was purchased from Gattfossé (Saint-Priest, France), Tween 80 was purchased from Merck (Johannesburg, South Africa) and efavirenz was donated by Adcock Ingram Limited (Wadeville, South Africa). Sodium chloride was purchased from Minema (Roodepoort, South Africa). HPLC-grade acetonitrile was purchased from Merk (Darmstadt, Germany). HPLC-grade water was produced using a RephiLe Bioscience Direct-Purefi Ultrapure RO Water system (Boston, MA, USA).

2.1.1.2. Instruments

A sonication bath (Digital Ultrasonic Cleaner PS-10A, Meizhou city, China) was used during the development process. A Benchmark "my Fuge" mini centrifuge (Benchmark Scientific, Sayreville, NJ, USA). HPLC analysis was performed using an Agilent 1100 Liquid Chromatography series equipped with a quaternary pump (G1311A), degasser (G1322A), diode array detector (G1315B) and manual injector (G1328B) with a Phenomenex® Kinetex® column (2.6 µm C18, 100 Å, 150 × 4.6 mm i.d.). Samples were freeze-dried using a LABCONCO FreeZone ® 6 Liter Benchtop Freeze-Dry system (Kansas City, MO, USA). A PerkinElmer Spectrum 100 FT-IR Spectrometer was used to record IR spectra and a TA DSC 250 instrument was used for thermal analysis. The material crystallinity was assessed using an XRD D8 Discover or D2 Phaser Instrument (Bruker, Billerica, MA, USA). A Zetasizer nano ZEN–3600 MAL1043132 from Malvern Instruments (Malvern, UK) was used to determine the particle size, polydispersity index and zeta potential of the materials. Particles' shape was analyzed using a Zeiss Libra-120KV TEM instrument (Oberkochen, Germany). The elemental composition of the developed materials was evaluated by using an INCA PENTA FET coupled to VAGA TESCAM energy-dispersive X-ray spectroscopy (Brno, Czech Republic).

2.1.2. Methods

2.1.2.1. Quantitative Determination of Efavirenz

A reversed-phase high-performance liquid chromatographic method developed by Bienvenu et al. was validated for the quantification of EFV[160]. The validated method was applied in the solubility, encapsulation and drug loading capacity, and *in vitro* drug release studies.

2.1.2.1.1. Chromatographic conditions

The chromatographic conditions used to validate the HPLC method are described in Table 6. The instrument consisted of an Aligent 1100 Liquid Chromatography Series equipped with a quaternary pump (G1311A), degasser (G1322A), diode array detector (G1315B) and manual injector (G1328B).

Table 6. *Chromatographic parameters*

Parameter	Description or Value
Column	Phenomex Kinetex® 2.6 µm, C18 100 Å, 150 x 4.6 mm
Mobile phase	0.1% Formic acid buffer + Acetonitrile (25:75)
Injection volume	20.0 µl
Flow rate	1 ml/min
Retention time	2.48 ± 0.012
Reaction time	3 min
Wavelength	247 nm

2.1.2.1.2. Description of the Validation Procedure

The selected HPLC method was validated according to the International Council for Harmonization guidelines (ICH 2005). Linearity range, accuracy and precision (repeatability and intermediate precision) were investigated to ensure that the method was suitable under the actual experimental conditions. The stock solution of Efavirenz was prepared by accurately weighing 25 mg of the analytical standard into a 25 mL clean and dry volumetric flask to which a mixture of acetonitrile and MilliQ water (40:60) was added up to the meniscus. Sonication was applied to the resultant mixture to obtain complete dissolution of Efavirenz.

d) Linearity

A range of five calibration standard (5, 35, 65, 95 and 125 µg) were prepared. The calibration curve was plotted using peak areas of Efavirenz against standard concentrations. The linearity was assessed by using the correlation coefficient (R squared). Experiments were run five times for each of the five calibration standards in order to calculate the relative standard deviation (RSD) of the slope.

e) Accuracy and Precision

Intra- and interday accuracy and precision were checked by assaying five consecutive replicates of three low, medium and high concentrations (10, 55 and 105 µg/ml) on five different days. Calibration curves were freshly determined on each day of the analysis. The accuracy was calculated as the percentage of the deviation between the known and the obtained concentrations. Precision was expressed in terms of the RSD within a single run (intraday) and between different assays (interday).

2.1.2.2. Solubility Assessment of Efavirenz

Efavirenz solubility was evaluated by adding an excess amount (1.5 g) to 5 mL of either Labrafac Lipophile 1349, MCT oil or HPLC-grade water. Then, shaking was performed for 24 h at 750 revolutions per minute (rpm) at 25 °C, followed by centrifugation at a speed of 6000 rpm for 30 min. The supernatant was thereafter treated with acetonitrile–water (40:60) to precipitate the lipids. Subsequently, it was filtered using a 0.22 µm simplepure™ syringe filter, and the efavirenz content in the filtrate was determined using the validated HPLC method.

2.1.2.3. Design and Optimization of Lipid Nanocapsules

2.1.2.3.1. I-optimal Mixture Design and Statistical Optimization

With the aid of Design-Expert software version 13.0 (Stat-Ease, Inc., Minneapolis, MN, USA), the I-optimal mixture design was performed to ascertain the interactive effects of different proportions of LNC components on the droplet size, polydispersity index and zeta potential. This design was selected given that it provides lower average prediction variance across the region of experimentation and is desirable for response surface methodology for which prediction is important[161]. The MCT oil, crude soy lecithin, Tween 80 and NaCl-water were the independent variables while the droplet size, polydispersity index, zeta potential and temperature of dilution were the responses. These responses were expected to fit the different

polynomial models for prediction purposes. The independent variables aligned with the ranges listed in Table 7 with the components' proportions totaling 100%.

Table 7. *Input variable constraints for I-optimal mixture design*

Low Limit (%)		Constraint		High Limit (%)
10,000	≤	A: PURE MCT OIL	≤	12,000
1500	≤	B: CRUDE SOY LECITHIN	≤	3000
9000	≤	C: TWEEN 80	≤	14,000
71,000	≤	D: NaCl-WATER	≤	79,500
		A + B + C + D	=	100,000

2.1.2.3.2. Model Optimization

The goal of this section was to assess the prediction performance of the polynomial models fitted to the responses. For this purpose, four different blends generated by the design expert software were selected and run in triplicate. The average values of the experimental data were compared to a 95% prediction interval (95%PI).

Equation 2. *95% Prediction Interval (95%PI)*

$$95\%\text{PI} = \hat{y}_0 \pm t_{\left(\frac{\propto}{2}, residual\ df\right)} \times SE_{pred} \quad \textbf{(Eq. 2)}$$

where $\hat{y}_0$ is the predicted value of the response, $t_{\left(\frac{\propto}{2}, residual\ df\right)}$ is the student's *t* critical value and SE_{pred} is the standard error of the prediction.

As presented in Table 8, the optimization criteria consists of maximized or minimized proportions of Tween 80 or MCT oil with proportions of crude soy lecithin and NaCl-water maintained in the fixed ranges of 1.5–3% and 71–79.5%, respectively.

Table 8. *Optimization criteria and generated blends*

Components (%)	Blend 1	Blend 2	Blend 3	Blend 4
Criteria	**A maximized and C minimized**		**A minimized and C maximized**	
Unit	**%**		**%**	
MCT oil (A)	12.00	12.00	10.00	10.00

Crude soy lecithin (B)	3.00	1.50	3.00	1.50
Tween 80 (C)	9.00	11.70	13.10	12.94
NaCl-water (D)	76.00	74.80	73.90	75.56

2.1.2.4. Preparation of Lipid Nanocapsules

The I-optimal mixture design from the Design Expert software version 13.0 generated 24 and 4 blends, respectively, for the design and optimization studies of LNCs. These were prepared using an organic solvent-free phase-inversion method. Briefly, as inspired from Heurtault et al., a total weight of 2.5 g of all components (MCT oil, crude soy lecithin, Tween 80 and NaCl-water with NaCl amount fixed at 50 mg in all formulations) were mixed in a round boiling flask under 1300 rpm magnetic stirring in an oil bath mounted on a hot plate. The temperature was raised from room temperature to 95 °C and three temperature cycles were applied in a range of 70 to 95 °C where phase inversion resulting in translucent mixtures was observed. Then, to obtain stable LNCs, a sudden cooling of the translucent mixtures with cold HPLC-grade water (1 to 4 °C), three times the volume of NaCl-water, was applied during the last cycle. A condenser was always set up to avoid any evaporation.

2.1.2.5. Characterization

2.1.2.5.1. Droplet Size, Polydispersity Index and Zeta Potential

The Malvern Nano-ZS Zetasizer (Malvern Instruments, Worchester, UK) was alternately set to dynamic light-scattering mode for the droplet size (DS) and the polydispersity index (PDI) determination, and to laser Doppler anemometry (LDA) mode for the zeta potential (ZP). A dilution of 500 µL of the saturated samples in 50 mL of HPLC-grade water was performed prior to all determinations. The sample was placed into a 12.5 × 12.5 × 45 mm BRAND® disposable cuvette (BRAND GmbH + CO KG, Wertheim, Germany) for the DS and the PDI, while a folded capillary cell was used for the ZP, and the experiments were performed at 22 °C at a scattering angle of 173°. The same parameters were evaluated over a period of 28 days for stability studies using samples stored at 15 °C + 0.8.

Subsequently, a drop of each saturated sample was placed onto a 3.05 mm holey carbon copper grid (FORMVAR/Carbon support 300 mesh) obtained from TAAB Laboratories Equipment, Ltd., Alderson, Berks, RG7 8NA, UK, for microscopic visualization of the LNC. The sample was stained with uranyl acetate for better visualization. A Whatmanfi 110 hydrophilic filter

paper (Whatmanfi International, Ltd., Maidstone, UK) was used to adsorb excess liquid and the sample was allowed to dry for 24 h at room temperature (25 °C). Then, transmission electron microscopy (TEM) (accelerating voltage of 80 kV) was used to observe the shape of the LNCs. TEM images were processed using ImageJ software version 1.53e to allow for the establishment of the size distribution.

2.1.2.5.2. Encapsulation Efficiency and Drug Loading Capacity

The D-optimal (custom) randomized design from Design-Expert software version 13.0 (Stat-Ease, Inc., Minneapolis, MN, USA) generated 13 formulation runs for the optimization of the encapsulation efficiency and the drug loading capacity. Briefly, efavirenz, the independent input in this study, was added to an optimized LNC formulation (MCT oil:Lecithin:Tween 80:Salted-Water with ratio 12:3:9:76) in a range of 95 to 250 mg. After each preparation, a 1:4 (EVF-LNC:Millipore water) dilution was performed followed by centrifugation at 6000 rpm for 30 min. The supernatant was treated with acetonitrile–water (40:60) and filtered using a 0.22 µm simplepure™ syringe filter, and the efavirenz content in the filtrate was determined using the validated HPLC method.

The following formulas were used to determine the encapsulation efficiency and drug loading capacity:

Equation 3. *Encapsulation Efficiency (%)*

$$\%EE = \frac{Mf}{Mi} \times 100 \quad \textbf{(Eq. 3)}$$

where $\%EE$ stands for encapsulation efficiency, Mf is the efavirenz mass determined from the filtrate and Mi the initial mass of efavirenz in the formulation.

Equation 4. *Drug Loading Capacity (%DLC)*

$$\%DLC = \frac{Mf}{Mt} \times 100 \ \textbf{(Eq. 4)}$$

where $\%DLC$ stands for drug loading capacity, Mf is the efavirenz mass determined from the filtrate and Mt the total mass of the formulation.

2.1.2.5.3. Differential Scanning Calorimetry

Differential scanning calorimetry allowed for the thermal assessment of the developed EFV-LNC as compared to that of the blank-LNC, the physical mixture as well as that of the raw materials. Briefly, the LNC dispersions were freeze-dried overnight. Then, 3 to 5 mg of the dried samples were weighed in sealed aluminum pans for analysis and heated from 30 to 170 °C at a rate of 10 °C per minute using an empty aluminum pan as reference. Nitrogen flow rate of 20 mL/min was used to maintain an inert atmosphere in the sample chamber. DSC Pyris software allowed us to record changes in the heat flow of the samples and data process as thermograms. The physical mixture was prepared by simply blending efavirenz with raw materials (MCT oil, crude soy lecithin, Tween 80 and NaCl-water) at 35 °C, in amounts equivalent to the ones used to form an optimized EFV-LNC formulation. After freeze-drying the physical mixture, 3 to 5 mg aliquot was weighed and analyzed under the same conditions as LNC.

2.1.2.5.4. X-ray Diffraction Spectroscopy

The crystallinity of EFV-LNC was compared to that of both free efavirenz and blank-LNCs by using X-ray powder diffraction (XRD) on a Bruker D8 Discovery equipped with a Lynx Eye detector (proportional counter), using a nickel filter and Cu-Ka radiation at 1.5404 Å. The scans were run at 2θ range 10–60° with a slit width of 6.0 mm at a scanning speed of 1° min^{-1}. Samples were prepared as described in section 2.1.2.4., then both EFV-LNCs and blank-LNC were freeze-dried and up to 0.2 g aliquot was weighed for analysis.

2.1.2.5.5. Fourrier Transform Infrared Spectroscopy

The PerkinElmer Spectrum 100 FTIR Spectrometer allowed us to obtain the sample's IR spectra in attenuated total reflection mode. Sixteen scans were applied in the wavenumber ranging from 650 to 4000 cm^{-1}. The signal from functional groups in the freeze-dried EFV-LNC were compared to those of freeze-dried blank-LNC and raw materials (free efavirenz, MCT oil, crude soy lecithin and Tween). LNC and EFV-LNC samples were prepared as described in section 2.1.2.4. An unmeasured aliquot was taken from each sample and from each raw material, then placed on the spectrophotometer for analysis.

2.1.2.5.6. Energy-Dispersive X-ray Spectroscopy

The energy-dispersive X-ray spectroscopy was used to perform the surface elemental analysis of EFV-LNCs in comparison to blank-LNC and raw materials (free efavirenz, crude soy

lecithin, Tween 80 and NaCl). LNC and EFV-LNC samples were prepared as described in section 2.1.2.4. An unmeasured aliquot was taken from each sample and from each raw material, then placed on different sample stubs for analysis.

2.1.2.6. *In Vitro* Drug Release

The optimized formulation with an efavirenz concentration of 17.5 mg/mL was considered for in vitro release studies. The release medium consisted of 1% sodium lauryl sulfate solution. The medium pH was adjusted to 7 then to 4 using concentrated HCl to ascertain the release behavior in both neutral and acidic conditions. Briefly, 200 µL of EFV-LNC formulation corresponding to 3.5 mg of efavirenz was placed in a dialysis bag (dialysis tubing cellulose membrane, flat width 25 mm (1.0 in), Sigma-Aldrich, St. Louis, MO, USA), which was soaked in 25 mL of release medium. Samples were submerged at 37 °C for 74 h while maintaining a constant shaking (100 rpm). At selected time intervals (0.5, 1, 2, 6, 10, 16, 21, 51 and 74), a 5 mL aliquot of the solution was withdrawn and immediately substituted with 5 mL of fresh release medium to maintain sink conditions. “Factorial multilevel categoric” design was previously performed and generated 66 runs corresponding to a triplicate for each level in both pH 4 and pH 7. The number of levels was 11 corresponding to the time intervals, and the design had two “categoric” factors corresponding to pHs 4 and 7.

2.1.2.7. Statistical Analysis

Statistical analyses were performed using the two-way analysis of variance (ANOVA), and significance was tested at the 0.05 level of probability. Additionally, certain software packages, such as Design Expert, OriginPro version 9, Microsoft Excel, and Image-J, were used in data treatment.

Project II: "Design, Synthesis, Manufacture, Characterization and Evaluation of Lipid Nanocapsules-Hydrogel Composite"

A manuscript entitled "Lipid Nanocapsules in chitosan-g-iota carrageenan-g-poly (acrylamide-co-acrylic acid) hydrogel scaffold, for Pulmonary Drug Delivery System: Design, Synthesis, Manufacture, Characterization and Evaluation", based on results presented in this second project, is underway to be submitted for publication in ACS Applied Materials & Interfaces.

2. MATERIAL AND METHOD

2.2. Materials and Methods for Project II

2.2.1. Material

2.2.1.1. Chemicals

Crude Soy lecithin granules were purchased from Health Connection Wholefoods (USA). According to the manufacturer's specifications, 100 g of the granules mainly contained phosphatidylcholine (23 g), phosphatidylinositol (14 g), polyunsaturated fat (35 g), saturated fat (13 g), glycaemic carbohydrates (8 g) and sodium (0.011 g). MCT oil was obtained from Absolute Organix (Jeppestown, Johannesburg), Labrafac Lipophile 1349 was purchased from Gattfossé (France), Tween 80 was purchased from Merck (Johannesburg, Gauteng, South Africa), Efavirenz was donated by Adcock Ingramfi Limited (Wadeville, Gauteng, South Africa). Iota-carrageenan (iCar), chitosan low molecular weight (CS), acrylic acid (AA), N,N methylene bisacrylamide (MBA) and acrylamide (AAm) were purchased from Sigma-Aldrich (Darmstadt, Germany). Glacial acetic acid, sodium chloride and acetone ware purchased from Minema (Roodepoort, South Africa). Ammonium persulfate was purchased from Saarchem (Wadeville, South Africa). HPLC grade acetonitrile was purchased from Merk (Germany). HPLC-grade water was produced using a RephiLe Bioscience Direct-Purefi Ultrapure RO Water system, (Boston, MA, USA).

2.2.1.2. Instruments

A sonication bath (Digital Ultrasonic Cleaner PS-10A, Meizhou city, China) was used during the development process. A Benchmark "my Fuge" mini centrifuge (Benchmark Scientific, Sayreville, NJ, USA). HPLC analysis was performed using an Agilent 1100 Liquid Chromatography series equipped with a quaternary pump (G1311A), degasser (G1322A), diode array detector (G1315B) and manual injector (G1328B) with a Phenomenex® Kinetex® column (2.6 µm C18, 100 Å, 150 × 4.6 mm i.d.). Samples were freeze-dried using a LABCONCO FreeZone ® 6 Liter Benchtop Freeze-Dry system (Kansas City, MO, USA). A PerkinElmer Spectrum 100 FT-IR Spectrometer was used to record IR spectra and a TA DSC 250 instrument was used for thermal analysis. The material crystallinity was assessed using an XRD D8 Discover or D2 Phaser Instrument (Bruker, Billerica, MA, USA). A Zetasizer nano ZEN–3600 MAL1043132 from Malvern Instruments (Malvern, UK) was used to determine the particle

size, polydispersity index and zeta potential of the LNC. Particles' shape was analyzed using a Zeiss Libra-120KV TEM instrument (Oberkochen, Germany). The elemental composition of the developed materials was evaluated by using an INCA PENTA FET coupled to VAGA TESCAM energy-dispersive X-ray spectroscopy (Brno, Czech Republic). The surface morphology of hydrogels was determined under a TESCAN VEGA scanning electron microscope (Brno, Czech Republic).

2.2.2. Methods

2.2.2.1. Preparation of Efavirenz based Lipid Nanocapsules (EFV-LNCs)

EFV-LNCs were prepared using the phase inversion method developed in the first project[162]. Briefly, it consisted of a blend of MCT oil, lecithin, tween 80 and NaCl-Water in a percentage (w/w) ratio of 12:3:9:76 and containing 17.5 mg/ml of Efavirenz. Practically, 25 g of empty LNCs components were weighed. In other words, 3 g of MCT oil, 0.75 g of lecithin, 2.25 g of tween 80 and 19 g of NaCl-Water (water and NaCl respectively accounting for 18.5 and 0.5 g) were weighed in a 250 round boiling flask and 1.35 g of Efavirenz were added. The mixture was magnetically stirred at 1300 rpm in an oil bath mounted on a hot plate, then heated to 95 °C and three temperature cycles were applied in the range of 70-95 °C where phase inversion resulting in translucent mixtures was observed. Then, in order to obtain stable LNCs, a sudden cooling of the translucent mixtures with cold HPLC-grade water (1 to 4 °C), three times the volume of water, was applied during the last cycle. A condenser was always in place to avoid evaporation.

2.2.2.2. Design and Optimization of chitosan-g-iota carrageenan-g-poly (acrylamide-co-acrylic acid) hydrogel (CS/iCar-p(AAm-co-AA))

Design Expert version 13 (Stat-Ease, Inc., Minneapolis, MN, USA) was used to perform the I-optimal mixture design to evaluate the interactive effects of the iCar-CS hydrogel components on its swelling capacity. The independent variables consisted of two polymers (iota-carrageenan and chitosan), two monomers (acrylic acid and acrylamide) and a crosslinker (N,N-methylene bisacrylamide), while the output variable was the swelling capacity which had to fit a polynomial model capable of predicting its values. The input variables are listed in Table 9 with their proportions totalling 100 %.

Table 9. *I-optimal mixture design input variables*

Low Limit (%)		Constraint		High Limit (%)
3.000	≤	A:IOTA-CARRAGEENAN	≤	6.000
3.000	≤	B:CHITOSAN	≤	6.000
40.000	≤	C:ACRYLIC ACID	≤	53.000
40.000	≤	D:ACRYLAMIDE	≤	53.000
1.000	≤	E:N,N METHYLENE BISACRYLAMIDE	≤	3.000
		A+B+C+D+E	**=**	**100.000**

2.2.2.3. Model optimization and confirmation

This section aimed at evaluating the fitted polynomial model's ability to predict swelling capacity. The swelling capacity maximization was the only optimization criteria. The software generated a couple of blends and the one with the highest desirability was selected and synthesised three times, followed by a triplicate measurement of the swelling capacity. The average values of the experimental data were compared to 95% prediction interval (95%PI).

$95\%\text{PI} = \hat{y}_0 \pm t_{\left(\frac{\propto}{2}, residual\ df\right)} \times SE_{pred}$ (**Eq. 2**) where $\hat{y}_0$ is the predicted value of the response, $t_{\left(\frac{\propto}{2}, residual\ df\right)}$ is the student's t critical value and SE_{pred} is the standard error of the prediction.

2.2.2.4. Synthesis of CS/iCar-p(AAm-co-AA) hydrogel

The method used in this section was inspired by Rahmani et al. with some modifications [163]. It consisted of hydrogel synthesis by free radical precipitation graft copolymerization AA/AAm on iota-carrageenan/chitosan backbone using APS as an initiator. Concisely, all of the initial ingredients were combined to make a total weight of 500 mg per batch. Iota-carrageenan and chitosan were separately dissolved in 10 ml HPLC grade water in a 50 mL round boiling flask submerged in an oil bath mounted on a hot plate pre-set at 60°C (Mixture A) and in 10 mL of a 1 wt % acetic acid solution in a beaker (Mixture B), respectively. Both mixtures were stirred at 800 rpm for 1 hour to achieve homogeneity. Mixture B was then added to mixture A, followed by appropriate amounts of acrylic acid, acrylamide and MBA. Polymerization was thereafter initiated by adding APS (0.05 – 0.2 g). The reaction was carried out under nitrogen atmosphere. The resulting hydrogels were then rinsed several times using approximately 500 mL of acetone before being dried in the oven at 40 °C.

2.2.2.5. Development of EFV-LNC-CS/iCar-p(AAm-co-AA) hydrogel composite

The EFV-LNC-CS/iCar-p(AAm-co-AA) hydrogel composite was developed by allowing the hydrogel to entrap the EVF-LNC, followed by the quantitative determination of EFV encapsulated in the entrapped LNC. Hence, a D-optimal (custom) randomized design was set up for this purpose by using the Design-Expert software version 13.0 (Stat-Ease, Inc., Minneapolis, MN, USA). This one generated 13 runs consisting of EFV concentration in LNCs ranging from 17.5 mg/mL to 87.5 mg/mL. The encapsulation was achieved using the swelling equilibrium method[164]. Briefly, an appropriate volume of EFV-LNCs corresponding to the desired concentration was diluted in a 25 mL volumetric flask. The resulting solution was used to soak a defined amount of dried hydrogel (50 mg) for 24 hours at room temperature. Following that, the swollen hydrogel was filtered out of the solution and rinsed with HPLC grade water. The filtrate was collected in a clean beaker for estimation of non-encapsulated EFV-LNCs. Hence, an aliquot (150 µL) of this filtrate was taken and diluted in a 10 ml volumetric flask using a mixture of acetonitrile and water (40:60). The EFV content was then determined by using a reversed-phase high performance liquid chromatographic method developed by Bienvenu et al. and validated in the first project [160,162].

The encapsulation efficiency was calculated using the formula below:

$$\%EE = \frac{Mf}{Mi} \times 100 \text{ (Eq. 3)}$$

Where %EE stands for encapsulation efficiency, Mf is the Efavirenz mass determined from the filtrate and Mi the initial mass of efavirenz in the soaking solution.

2.2.2.6. Characterization

2.2.2.6.1. Droplet size, polydispersity index and zeta potential of EFV-LNCs

For droplet size (DS) and polydispersity index (PDI) determination, the Malvern Nano-ZS Zetasizer (Malvern Instruments, Worchester, UK) was alternately set to dynamic light scattering mode and laser doppler anemometry (LDA) mode (ZP). Prior to all measurements, 500 µl of the saturated sample were diluted in 50 ml of HPLC grade water. For the DS and PDI, the sample was placed in a 12.5 x 12.5 x 45 mm BRAND® disposable cuvette (BRAND GmbH + CO KG, Wertheim, Germany), while the ZP was performed in a foldable capillary cell, and the tests were carried out at 22 °C with a scattering angle of 173°.

2.2.2.6.2. Swelling capacity of CS/iCar-p(AAm-co-AA) hydrogel

The swelling capacity of the produced hydrogel was estimated using the filtration method. A hydrogel amount of 50 to 100 mg was recorded as W_0 and socked in a beaker containing 40 to

80 mL of HPLC grade water for 24 hours. Afterward, the mass of a piece of filter paper pre-saturated with distilled water was recorded as W_1 and placed in a Büchner funnel. The swollen hydrogel in solution was then filtered under vacuum to remove any surplus water. The filter paper (with the swollen hydrogel on it) was removed from the funnel and weighed again, yielding the final mass recorded as W_2. The equation below was used to calculate the swelling capacity (SC) and measurements were done in triplicate[165]:

Equation 5. *Swelling Capacity (%SC)*

$$\%SC = \frac{W_2 - W_1}{W_0} \times 100 \quad \textbf{(Eq. 5)}$$

2.2.2.6.3. Fourier Transform Infra-Red Spectroscopy (FTIR)

The IR spectra of the synthesized hydrogel along with the manufactured LNC-hydrogel composite were compared with those of the raw material to assess any possible changes within their functional groups. The PerkinElmer Spectrum 100 FTIR Spectrometer in attenuated total reflection mode allowed to record the different spectra. Sixteen scans with wavenumbers ranging from 650 to 4000 cm-1 were performed. Experiments were realised on the freeze-dried samples of the synthesized hydrogel and the LNC-hydrogel composite.

2.2.2.6.4. Thermal Gravimetric Analysis

Thermal Gravimetric Analysis (TGA) was used to assess the thermal decomposition profiles of both CS/iCar-p(AAm-co-AA) hydrogel and EFV-LNC-CS/iCar-p(AAm-co-AA) hydrogel composite, in comparison with iota carrageenan and chitosan. Experiments were performed in an inert nitrogen environment using a Perkin TGA 4000 instrument, where a sample of 2–5 mg of the material was heated at a rate of 10°C per minute from 30 to 600°C.

2.2.2.6.5. Powder X-ray diffraction

The phase behaviour of both freeze-dried CS/iCar-p(AAm-co-AA) hydrogel and EFV-LNC-CS/iCar-p(AAm-co-AA) hydrogel composite was assessed using Powder x-ray diffraction, which allowed to obtain and examine their crystallinity profiles in comparison with iota-carrageenan, and chitosan. The instrument consisted of a Bruker D8 Discovery equipped with a Lynx Eye detector (proportional counter), using a nickel filter and Cu-Ka radiation at 1.5404 Å. The scans were performed at a scanning speed of 1°min-1 and a 2-θ range of 10–60° with a slit width of 6.0 mm.

2.2.2.6.6. Scanning Electron Spectroscopy (SEM) and Energy-Dispersive X-ray Spectroscopy (EDS)

The surface morphology and elemental composition of both CS/iCar-p(AAm-co-AA) hydrogel and EFV-LNC-CS/iCar-p(AAm-co-AA) hydrogel composite were investigated using SEM and EDS, respectively. An INCA PENTA FET was employed in conjunction with VAGA TESCAM energy dispersive X-ray spectroscopy. Prior to analysis, the hydrogels were swollen to equilibrium (24 h) in HPLC-grade water at room temperature and then lyophilized in a freeze-dryer using a LABCONCO FrezeZone® 6 Liter Benchtop Freeze Dry System. The resulting lyophilic hydrogel was fixed on aluminium stubs, coated with gold prior to all the experiments.

2.2.2.7. Statistical Analysis

The two-way analysis of variance (ANOVA) was used for statistical analyses, and significance was tested at the 0.05 level of probability. Besides, software packages like Design Expert, OriginPro version 9, and Microsoft Excel were used in data treatment.

Chapter Three

Results and Discussion

Project I: "Design, Manufacture, Characterization and Evaluation of Lipid Nanocapsules to Enhance the Biopharmaceutical Properties of Efavirenz

Mukubwa, G.K.**; Safari, J.B.; Walker, R.B.; Krause, R.W.M. Design, Manufacturing, Characterization and Evaluation of Lipid Nanocapsules to Enhance the Biopharmaceutical Properties of Efavirenz.* Pharmaceutics ***2022, 14, *1318. https://doi.org/10.3390/pharmaceutics14071318*

The above paper published in Pharmaceutics reports most of the results obtained in this first project

3. RESULTS AND DISCUSSION

3.1. Results and Discussion for Project I

3.1.1. Validation of a Reversed-Phase High-Performance Liquid Chromatographic Method for Quantitative Determination of Efavirenz

A reverse phase HPLC method for Efavirenz quantification was validated according to the International Council for Harmonization guidelines (ICH 2005). It consisted of an isocratic elution method that was applied for an analysis time of 3 min at a flow rate of 1 ml/min. The retention time of the drug was 2.48 ± 0.012 min, as shown in EFV chromatogram in Figure 14 The mobile phase consisted of a 75:25 (V/V) mixture of acetonitrile and MilliQ water adjusted to pH 3.0 using formic acid 0.1%. The injection volume was 20 µl and the wavelength for detection was set at 247 nm.

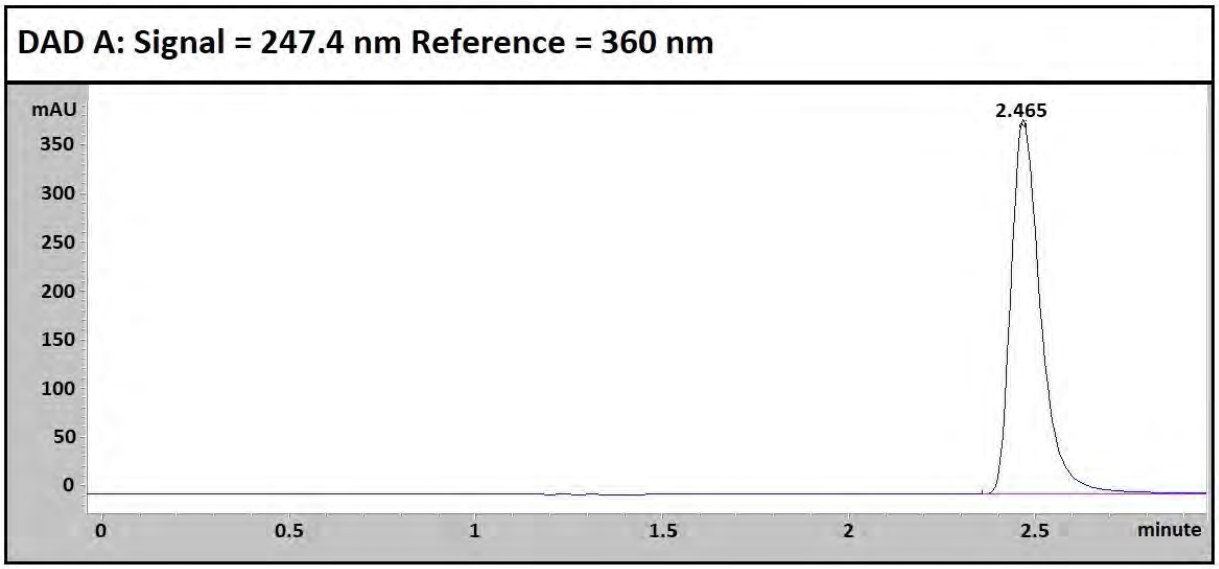

Figure 14. *Chromatogram of Efavirenz detected at 247.4 nm after nearly 2.5 minutes elution.*

3.1.1.1. Linearity

The linearity of the method was determined by preparing five different standard concentrations, namely 5, 35, 65, 95 and 125 µg/ml, which were injected to the HPLC system five times each in order to calculate the relative standard deviation. Figure 15 shows that the method was linear with a correlation coefficient (R^2) of 0.9995.

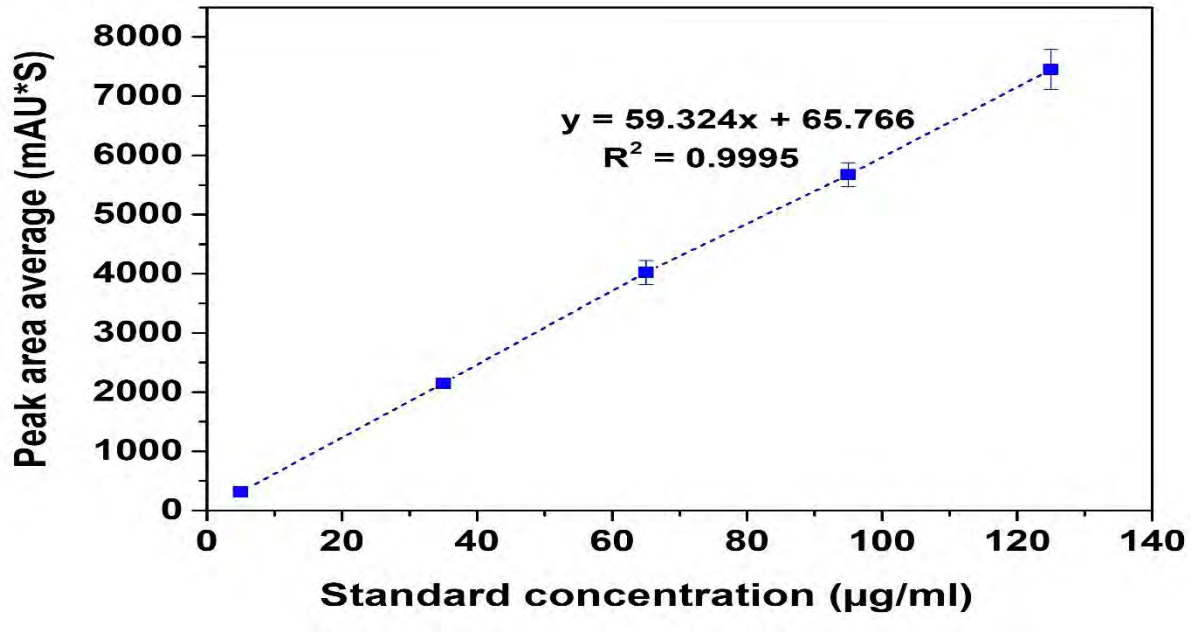

Figure 15. *HPLC calibration curve of Efavirenz.*

3.1.1.2. Precision and Accuracy

Intra- and inter-day accuracy and precision was checked by measuring five consecutive replicates of three low, medium and high concentrations (10, 55 and 105 µg/ml) on five different days. The method turned out to be precise with %RSD values < 4% for all the tested samples. Table 10 presents both intra- and interday precision and accuracy profiles of the validated method.

Table 10. *Precision and accuracy of the validated method*

	Nominal concentration (µg/ml)	Found concentration mean (µg/ml)	±SD mean	Precision (RSD, %)	Accuracy (%)
Intraday	10	9,83301868	0,23643125	2,40446249	98,3301868
	55	55,9377992	2,114132	3,77943363	101,705089
	105	105,844751	2,33118088	2,20245299	100,804525
Interday	10	10,0611445	0,38062244	3,78309291	100,611445
	55	55,4418087	1,99505604	3,59846854	100,803289
	105	105,678684	1,38221094	1,30793732	100,646366

3.1.2. Solubility Assessment of Efavirenz

As highlighted in Figure 16, Labrafac Lipophile 1349 displayed the highest solubility for efavirenz (3336 ± 4.27 mg/mL), followed by MCT oil (27,426 ± 7.97 mg/mL). The lowest solubility was observed in HPLC-grade water (0.089 ± 0.0044 mg/mL) confirming the

practically insoluble nature of this drug already reported in the literature [166]. Labrafac Lipophile 1349 and MCT oil are triglyceride-based oils. The solubilizing capacity of triglycerides is highly influenced by their intrinsic composition, namely, the degree of unsaturation of their carbon chains. The lower the degree of unsaturation, the higher the solubility [167–169]. Both Labrafac Lipophile 1349 and MCT oil are made of saturated fatty acids (capric and caprylic fatty acids). The difference in the solubility of efavirenz in these two oils could be accounted for by their manufacturing process. Labrafac Lipophile is claimed to be originated from strictly vegetal raw materials (not specified) and contains up to 80% and up to 50% of caprylic and capric acid, respectively. MCT oil also originates from vegetal raw material, namely, coconut oil and palm kernel, and is claimed to contain 60% of caprylic and 40% of capric acid. Based on these results and given its availability and affordability on the local market, MCT oil was selected for further investigations.

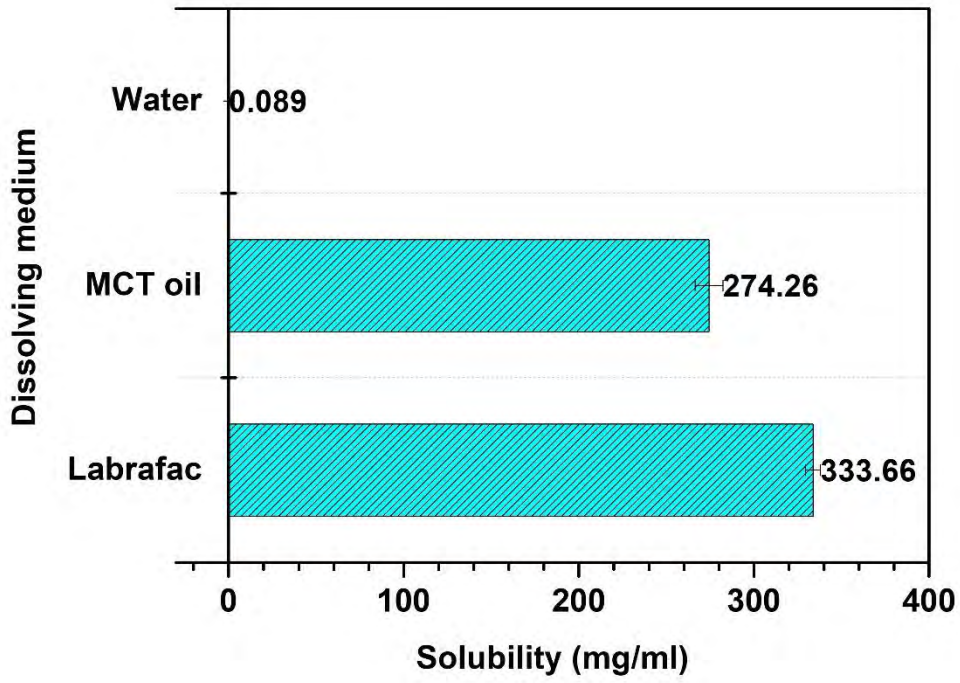

Figure 16. *Solubility profile of efavirenz in Labrafac Lipophile 1349, MCT oil and HPLC-grade water.*

3.1.3. Statistical Analysis and Optimization of Lipid Nanocapsules

Design-Expert software version 13.0 (Stat-Ease, Inc., Minneapolis, MN, USA) was applied to the design and optimization studies of LNCs. Based on the constraints previously summarized in Table 6 (I-Optimal Mixture Design and Statistical Optimization section), a single-block I-optimal mixture design was launched to ascertain the interactive effects of the different

proportions of the mixture components. The I-optimal design provides lower average prediction variance across the region of experimentation and was therefore suitable for this study as the prediction of LNC DS, PDI and ZP is important. The I-optimal design allows best fitting the different responses to statistical models, such as linear, quadratic and special cubic models, for points prediction and optimization [161]. The optimal custom design algorithm generated 24 blends summarized in Table 11, along with their respective values for the droplet size, polydispersity index and zeta potential.

Table 11. *Blend compositions generated by I-optimal design and observed experimental data*

	Input Variables (% m/m)				**Responses**			
	MCT Oil A	**Crude Soy Lecithin B**	**Tween 80 C**	**Salt Water D**	**Droplet Size (nm)**	**PDI**	**Zeta Potential (mV)**	**Temperature of Dilution (°C)**
1	12.00	2.16	11.50	74.34	40	0.093	−49	93
2	10.00	2.42	11.49	76.09	33	0.127	−73	83
3	11.16	1.50	11.38	75.95	46	0.152	−56	95
4	11.83	2.87	13.89	71.41	31	0110	−50	86
5	10.00	3.00	9.00	78.00	34	0.097	−37	85
6	10.68	1.99	14.00	73.33	33	0.128	−46	87
7	10.00	1.50	13.07	75.44	35	0.161	−48	90
8	10.00	3.00	14.00	73.00	29	0.183	−56	85
9	11.16	1.50	11.38	75.95	46	0.149	−57	95
10	12.00	1.50	9.00	77.50	72	0.065	−54	95
11	10.21	1.64	9.03	79.13	46	0.090	−35	95
12	12.00	2.16	11.50	74.34	40	0.136	−55	91
13	12.00	3.00	9.55	75.45	42	0.073	−53	89
14	11.79	1.50	12.92	73.79	43	0.101	−39	92
15	10.00	2.96	12.83	74.22	35	0.137	−56	86
16	10.97	3.00	11.45	74.58	39	0.113	−49	86
17	11.27	2.42	9.00	77.31	41	0.147	−64	87

18	10.25	1.50	10.53	77.72	40	0.089	−36	93
19	12.00	1.50	14.00	72.50	42	0.129	−41	89
20	10.67	3.00	10.10	76.22	37	0.099	−52	89
21	10.68	1.99	14.00	73.33	35	0.141	−44	87
22	10.00	2.42	11.49	76.09	33	0.177	−70	85
23	12.00	3.00	12.32	72.68	35	0.108	−52	85
24	11.27	2.42	9.00	77.31	47	0.113	−68	87

The precision of the design for predictions at different points in the design space was evaluated, and the resulting triangular contour plot as well as the surface plots of the standard error are presented in Figure 17. Given that the errors are almost uniform and relatively small (0.5–1.5 σ, where σ is the estimated variability of the data) across the region of interest, the fitted models are expected to provide precise predictions.

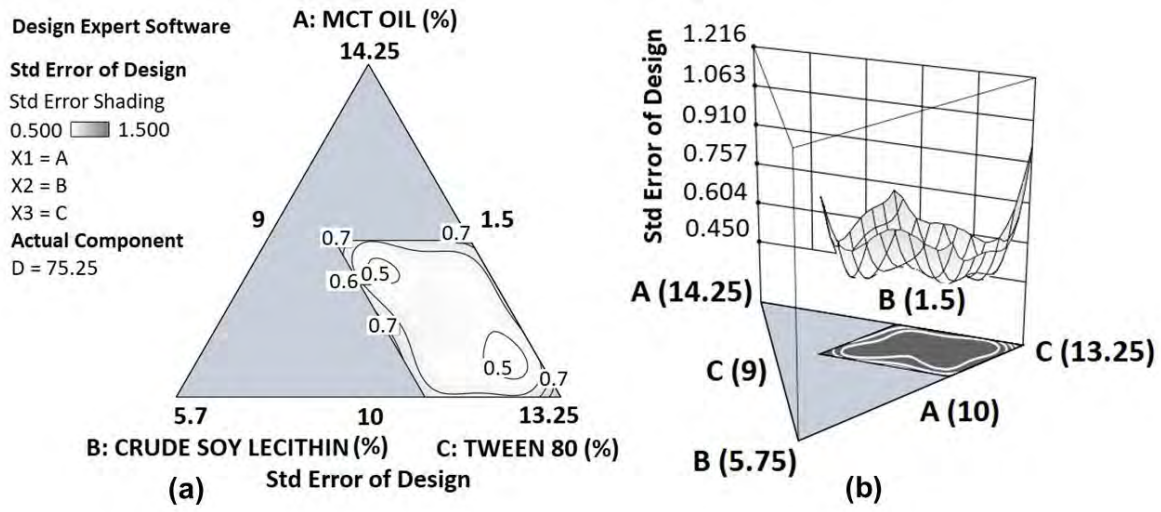

Figure 17. *Contour plot (a) as well as the surface plot (b) of the standard error at different points in the design space with changing compositions of MCT oil (A), crude soy lecithin (B) and Tween 80 (C), and with fixed composition of NaCl-water (D).*

The design software automatically fitted the experimental data to different statistical models, including linear, quadratic, special cubic and cubic models. Statistical parameters, such as the predicted residual sum of squared (PRESS), the lack of fit and the adjusted and predicted R squared were analyzed and some model reductions were applied to obtain best fit as well as best prediction ability. Models with the lowest values for the PRESS and high values for both adjusted and predicted R squared are associated with good prediction ability for a set of data [168]. Tables 12 and 13, respectively, summarize the ANOVA analysis of the suggested models

and that of reduced models that best fit the data. Table 14 highlights the PRESS values of modified models as compared to PRESS values of suggested polynomials.

Table 12. *Analysis of variance of the suggested models*

Response	Suggested Model	f-Value	Degrees of Freedom	*p*-Value	R^2	Adjusted R^2	Predicted R^2	Adequate Precision
Droplet size (nm)	Special cubic	45.80	13	<0.0001	0.9835	0.9620	0.8718	33.2536
PDI	Linear	4.69	3	0.0123	0.4128	0.3247	0.1771	6.7749
Zeta potential (mV)	Special cubic	5.09	13	0.0072	0.687	0.6980	−2.3389	8.9294
Temperature of dilution (°C)	Linear	7.22	13	0.0018	0.9037	0.7785	−0.1615	7.8467

Table 13. *Analysis of variance of the modified models*

Response	Reduced Model	f-Value	Degrees of Freedom	*p*-Value	R^2	Adjusted R^2	Predicted R^2	Adequate Precision
Droplet size (nm)	Reduced special cubic	50.28	12	<0.0001	0.9821	0.9626	0.8876	34.5526
PDI	Linear	NM	NM	NM	NM	NM	NM	NM
Zeta potential (mV)	Reduced special cubic	4.79	12	0.0072	0.8393	0.6641	−1.0050	8.3624
Temperature of dilution (°C)	Reduced special cubic	10.79	8	<0.0001	0.8520	0.7730	0.6025	9.3516

NM: Not modified.

Table 14. *PRESS values of suggested and modified models*

	PRESS Values	
	Suggested Models	**Modified Models**
Droplet size (nm)	217.02	190.28
Polydispersity index	0.0182	NM
Zeta potential (mV)	8171.50	4906.83
Temperature of dilution (°C)	386.72	132.34

NM: Not modified.

The droplet size, zeta potential and temperature of dilution were originally fitted to Scheffé special cubic models prior to their reduction for best fit and better prediction ability. The polydispersity index was fitted to a linear model. These fitted models were subject to model *p*-value tests to ascertain the assumption of their prediction ability, and lack of fit F-test to evaluate the variation of data around them. All models were significant (model *p*-value < 0.05), assuming that they could be used to predict data and navigate the design space. Unlike the models fitted for zeta potential and temperature of dilution whose lack of fit was significant (*p*-value < 0.05), an insignificant lack of fit (*p*-value > 0.10) was observed for the reduced special cubic and linear models, respectively, fitted to the droplet size and the polydispersity index, suggesting that the models' predicted data fit the actual experimental response data [170–172]. Prior to the prediction of the optimized formulation, the analysis of residuals was performed for the statistical diagnosis of the models, and the Box–Cox plots for power transformation confirmed that no transformation was required for any of the models.

3.1.4. Droplet Size, Polydispersity Index, Zeta Potential and Temperature of Dilution

Design Expert Software allowed fitting the droplet size, zeta potential and temperature of dilution to Scheffé's "reduced special cubic polynomials", while the polydispersity index was fitted to a linear polynomial. These ones are expressed by the following equations:

Equation 6. *Droplet size (DS)*

Droplet size = −215.99 x A + 1809.66 x B + 49.4047 x C + −8.08815 x D + −29.3894 x AB + 13.0495 x AC + 3.72536 x AD + −103,505 x BC + −19.1016 x BD + −0.0407471 x CD + 1.68149 x ABC + −0.232067 x ACD + 1.05428 x BCD (**Eq. 6**)

Equation 7. *Zeta potential (ZP)*

Zeta potential = 3159.65 x A + 9637.82 x B + 1599.49 x C + 94.2751 x D + −762,856 x AB + −173,983 x AC + −43.9283 x AD + −126.84 x BC + −112,035 x BD + −23.3279 x CD + 9.63158 x ABC + 8.43236 x ABD + 2.02236 x ACD (**Eq. 7**)

Equation 8. *Temperature of dilution*

Temperature of dilution = 221,779 x A + 45.6503 x B + 261,092 x C + 11.4998 x D + −27,609 x AC + −3.43182 x AD + −1.01391 x BD + −3.9841 x CD + 0.381584 x ACD (**Eq. 8**)

Equation 9. *Polydispersity Index (PDI)*

Polydispersity index = −0.0137378 x A + 0.000328786 x B + 0.01033 x C + 0.00203285 x D (**Eq. 9**)

where factors A, B, C and D stand for MCT oil, crude soy lecithin, Tween 80 and NaCl-water, respectively. These equations in terms of actual factors can be used to make predictions about the response for given levels of each factor. Here, the levels should be specified in the original units (%) for each factor.

As illustrated in Table 15, the experimental droplet size ranged from 29 to 72 nm. The ANOVA analysis revealed that the terms AB, BC, BD (p-value < 0.0001) and CD, ABC and BCD (p-value < 0.05) significantly influenced the model fitted to the droplet size. This corroborates the fact that changes in the proportions of A, B and C highly affect the droplet size. The droplet-size contour plot is shown in Figure 18a where the dark blue region corresponds to the smallest sizes as the proportions of both Tween 80 and crude soy lecithin increase, while MCT oil proportion is the lowest. Hence, it is interesting to note that the smallest size was observed for the blend where the highest proportion of both crude soy lecithin and Tween 80 were used with the lowest proportion of MCT oil (Table 11). Table 12 shows that the droplet size reduced special cubic model R squared value was 0.9821, meaning that this model could explain 98.21% of the variation in the response, therefore indicating the relevance of the model. The predicted R squared value of 0.876 is in reasonable agreement with the adjusted R squared value of 0.9626 (difference is less than 0.2), implying that the responses' trends could be analyzed by this model [172,173].

Table 15. *Summary of the responses*

Response	Name	Units	Observations	Minimum	Maximum	Mean	Std. Dev.	Ratio
R1	Droplet size	nm	24.00	29	72	39.75	8.58	2.48
R2	PDI		24.00	0.065	0.183	0.1216	0.031	2.82
R3	Zeta potential	mV	24.00	−73	−35	−51.67	10.32	2.09
R4	Temperature of dilution	°C	24.00	83	95	88.96	3.80	1.14

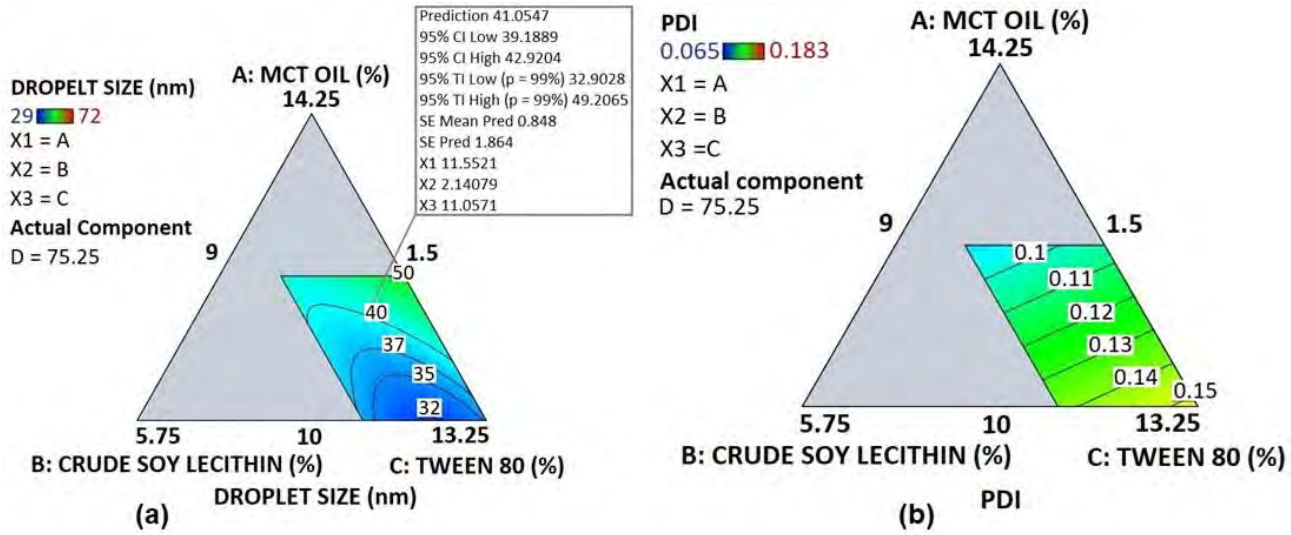

Figure 18. *Contour plot of droplet size (a) and polydispersity index (b).*

On the other hand, as depicted in Figure 18b, the polydispersity index < 0.2 was observed for all the studied formulations suggesting a good uniformity of size within the particles in the PNCs. The linear model shown in Table 12 is associated with very low adjusted and predicted R squared values, making this model not very strong for predictions. Nevertheless, the adequate precision of 6.7749 indicates an adequate signal; this value must be greater than "4" to explain the signal-to-noise ratio for excellent navigation in the design space [174]. Moreover, the model F-value of 4.69 and not significant lack of fit (*p*-value 0.4584), respectively, imply that the model is significant and that its predicted data fit the actual experimental response data [170–172]. However, given that this model could only explain 41.28% of the variation in the response (R^2 = 0.4128), model validation might help to assess this model's reliability for polydispersity index predictions [170].

Interestingly, the zeta potential values obtained suggest that the developed LNCs were likely to achieve good stability. As shown in Table 15, the zeta potential ranges from −73 to −35 mV

and its fitted model is significantly (p-value < 0.05) affected by the terms AB, AC, AD, BC, BD, CD, ABC and ACD. Negatively charged nanoparticles are likely to undergo macrophage uptake and allow drug targeted delivery to action sites [175–177]. Macrophages play a pivotal role in microbial infections. On one hand, they can be hijacked by some microbes such as M*ycobacterium tuberculosis* and rhinovirus that are likely to penetrate them and utilize them as reservoirs to replicate, disseminate or persist [178,179]. On the other hand, macrophages play an important role in recognizing the pathogen responsible of an infection. They are responsible of initiating and resolving inflammation reactions as well as repairing tissue damage. Since, they are the most numerous immune cells present in the lungs, and since they are susceptible to uptake negatively charged LNC, they are therefore a good for drug delivery in case of infection in the respiratory tract[178,179].

As to the data presented in Table 13, the reduced special cubic model could explain 83.93% of the variation in the response (R^2 = 0.8393). A negative predicted R squared was observed, suggesting that the overall mean may be a better predictor of the zeta potential than the present model.

As far as the temperature of the dilution is concerned, it was found to be significantly affected by crude soy lecithin and NaCl-water (model term BD p-value was 0.0126). The terms B and D, respectively, represent crude soy lecithin and NaCl-water. As depicted in Figure 19, the higher the crude soy lecithin proportion, the lower the temperature of the dilution. Dilution was applied at the phase inversion temperature, and phase inversion is observed when microemulsions form, resulting in translucent mixtures. Bi-continuous microemulsion structures are likely to be formed when the non-ionic surfactant is trapped at the interface [75]. Since the higher the amount of non-ionic surfactants, the more likely they are to be trapped at the interface; high amounts of crude soy lecithin are likely to be associated with a low dilution temperature. On the other hand, as the concentration of NaCl increased in the NaCl-water, the temperature of the dilution decreased. This corroborates with the previous studies in which high concentrations of NaCl were associated with a decrease in the phase inversion temperature [69,180].

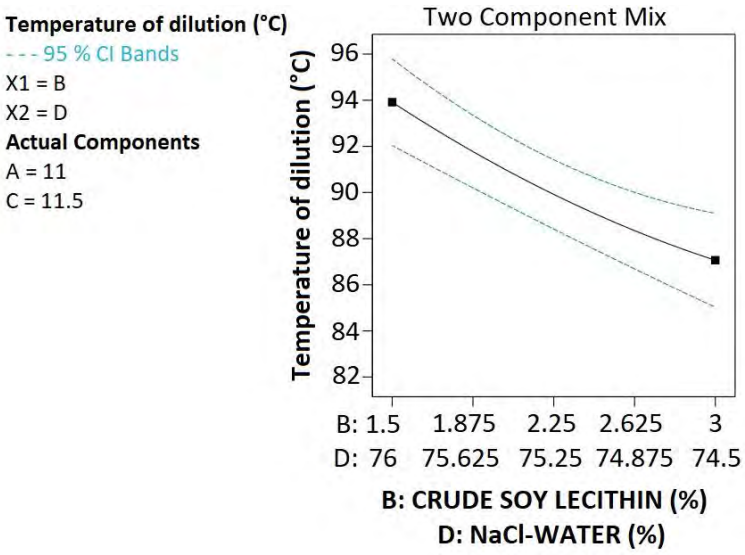

Figure 19. *Impact of crude soy lecithin and NaCl-water on temperature of dilution with MCT oil (A) and Tween 80 (C) proportions set, fixed at 11 and 11.5%, respectively.*

3.1.5. Model Optimization

In order to evaluate the polynomial models fitted to the droplet size, polydispersity index, zeta potential and temperature of dilution, four blends generated by the design expert software were selected and run in triplicate. MCT oil, lecithin, Tween 80 and NaCl-Water proportions (%) were, respectively, 12:3:9:76 for blend 1, 12:1.5:11.7:74.8 for blend 2, 10:3:13.1:73.9 for blend 3 and 10:1.5:12.9:75.6 for blend 4. As depicted in Table 16, all the average values (replicate = 3) of the experimental data were within the range of the 95% prediction intervals, suggesting a strong prediction ability for the polynomials models fitted to the responses. Given its lowest proportion of ionic surfactant (Tween 80), its ability to produce good particle-size uniformity (PDI = 0.12), as well as its high oil content susceptible to promote drug solubility in the nanocarrier, blend 1 was selected for further investigation, namely, the encapsulation efficiency and drug loading capacity evaluation.

Table 16. *Observed means against the prediction intervals*

	Response	**Mean**		**95% Prediction**	
		Predicted	**Observed**	**95% PI Low**	**95% PI High**
Blend 1	**Droplet size (nm)**	41.5892	41.3333	37.0875	46.0908
MCT oil: 12%	**PDI**	0.0835994	0.12	0.0426535	0.124545

Lecithin: 3% **Tween 80: 9%** **NaCl-Water: 71%**	**Zeta potential (mV)**	−59.8024	−58.6333	−76.1047	−43.5001
	Temperature of dilution (°C)	86.272	86	82.2926	90.2514
Blend 2 **MCT oil: 12%** **Lecithin: 1.5%** **Tween 80: 11.7%** **NaCl-Water: 74.8%**	**Droplet size (nm)**	48.3797	49.7633	44.9551	51.8043
	PDI	0.108375	0.141	0.0710762	0.145674
	Zeta potential (mV)	−41.9609	−53.5333	−53.8046	−30.1172
	Temperature of dilution (°C)	94.9996	95	91.9209	98.0782
Blend 3 **MCT oil: 10%** **Lecithin: 3%** **Tween 80: 13.1%** **NaCl-Water: 73.9%**	**Droplet size (nm)**	33.5363	30.52	30.3943	36.6782
	PDI	0.149043	0.179667	0.110426	0.187661
	Zeta potential (mV)	−58.7789	−51.8667	−70.0912	−47.4666
	Temperature of dilution (°C)	84.3132	84	81.3159	87.3105
Blend 4 **MCT oil: 10%** **Lecithin: 1.5%** **Tween 80: 12.9%** **NaCl-Water: 75.6%**	**Droplet size (nm)**	35.1093	38.5033	31.3772	38.8414
	PDI	0.150377	0.177667	0.111305	0.189449
	Zeta potential (mV)	−42.8831	−41.2667	−57.0207	−28.7456
	Temperature of dilution (°C)	88.6115	88	84.9719	92.2511

3.1.6. Encapsulation Efficacy and Drug Loading Capacity

3.1.6.1. Statistical Analysis

In order to determine the amount of efavirenz that LNCs are likely to entrap, their encapsulation efficiency and drug loading capacity were evaluated. The optimized blend 1, from the previous Section 3.1.5, was used for this purpose. This one consisted of a mixture of MCT oil, crude soy lecithin, Tween 80 and NaCl-water in a ratio of 12:3:9:76% (m/m). Furthermore, in order to build statistical models capable of predicting amounts of drug that would ensure both a high encapsulation efficiency and drug loading capacity in blend 1, the D-optimal (custom)

randomized design generated 13 formulation runs detailed in Table 17, together with the experimental data obtained.

Table 17. *Encapsulation efficacy and drug loading capacity of blend 1*

Input Variables (% m/m)						**Response (%)**	
	MCT Oil A	**Crude Soy Lecithin B**	**Tween 80 C**	**Salted Water D**	**Efavirenz**	**Encapsulation Efficiency**	**Drug Loading Capacity**
1	12.00	3.00	9.00	76.00	115.15	93.4	1.43
2	12.00	3.00	9.00	76.09	95	90.19	1.14
3	12.00	3.00	9.00	75.95	134.525	84.19	1.48
4	12.00	3.00	9.00	71.41	250	48.44	1.54
5	12.00	3.00	9.00	78.00	172.5	85.89	1.96
6	12.00	3.00	9.00	73.33	198.85	51.15	1.31
7	12.00	3.00	9.00	75.44	153.545	88.03	1.76
8	12.00	3.00	9.00	73.00	250	48.05	1.52
9	12.00	3.00	9.00	75.95	250	54.97	1.74
10	12.00	3.00	9.00	77.50	95	87.1	1.1
11	12.00	3.00	9.00	79.13	95	94.8	1.2
12	12.00	3.00	9.00	74.34	225.2	62.54	1.84
13	12.00	3.00	9.00	75.45	250	54.23	1.72

The encapsulation efficiency (EE%) and drug loading capacity (DLC%) were automatically fitted to sixth order polynomial models. The different statistical parameters of these models are detailed in Table 18. These were significant (model p-value < 0.05) and had predicted data fitting the actual experimental response data (lack-of-fit p-value > 0.05). However, they exhibited a low prediction ability as expressed by the high PRESS values along with predicted R^2 values that are not in reasonable agreement with the adjusted R^2 values (difference was more than 0.2), implying that response trends could not be analyzed by these models. Hence, model reduction was applied. It consisted of removing terms to improve the adjusted R^2 value, followed by the removal of terms with p-values > 0.100000. As a result, the encapsulation

efficiency and the drug loading capacity were, respectively, fitted to a linear model and a quadratic model as expressed by the equations below:

Equation 10. *LNC Encapsulation Efficiency (%EE)*

%EE = 120.562 + −0.273254 x A (**Eq. 10**)

Equation 11. *LNC Drug Loading Capacity (%DLC)*

%DLC = −0.390218 + 0.0215689 x A + −5.41283e-05 x A^2 (**Eq. 11**)

where A stands for the amount of efavirenz.

Table 18. *Statistical parameters of polynomial models fitted to encapsulation efficiency and drug loading capacity of blend 1*

	Encapsulation Efficiency		**Drug Loading Capacity**	
	Sixth Order Model	**Linear Model**	**Sixth Order Model**	**Quadratic Model**
PRESS values	2408.35	789.70	4.43	0.5820
R squared	0.9826	0.8584	0.9393	0.6311
Adjusted R squared	0.9653	0.8455	0.8783	0.5573
Predicted R squared	0.4514	0.8201	−3.8134	0.3669
Adeq Precision	16.1970	14.3630	10.7785	6.6481

These reduced models were significant (model *p*-value < 0.05) and had predicted R^2 values in reasonable agreement with the adjusted R^2 values (difference was less than 0.2). Adequate precision values higher than four indicated adequate signals, meaning that they could explain the signal-to-noise ratio for excellent navigation in the design space. However, the predicted data of these models could not fit the actual experimental data (lack-of-fit *p*-value < 0.05). Hence, model validation was performed to assess their prediction performance on the encapsulation efficiency and drug loading capacity (see Section 3.1.6.2.).

Interestingly, as illustrated in Figure 20, unlike the drug loading, as the amount of drug increases, the encapsulation efficiency decreases. This can be explained by the solubility of efavirenz in the liquid lipid core of LNC (see section 3.1.2.). As the LNC core becomes saturated, no more efavirenz dissolves. This means that dissolved efavirenz is at chemical equilibrium with an excess of undissolved efavirenz [39]. Therefore, the higher the undissolved

amount of efavirenz, the more likely it is to be detected in high concentrations in the supernatant when determining the encapsulation efficiency, as previously described.

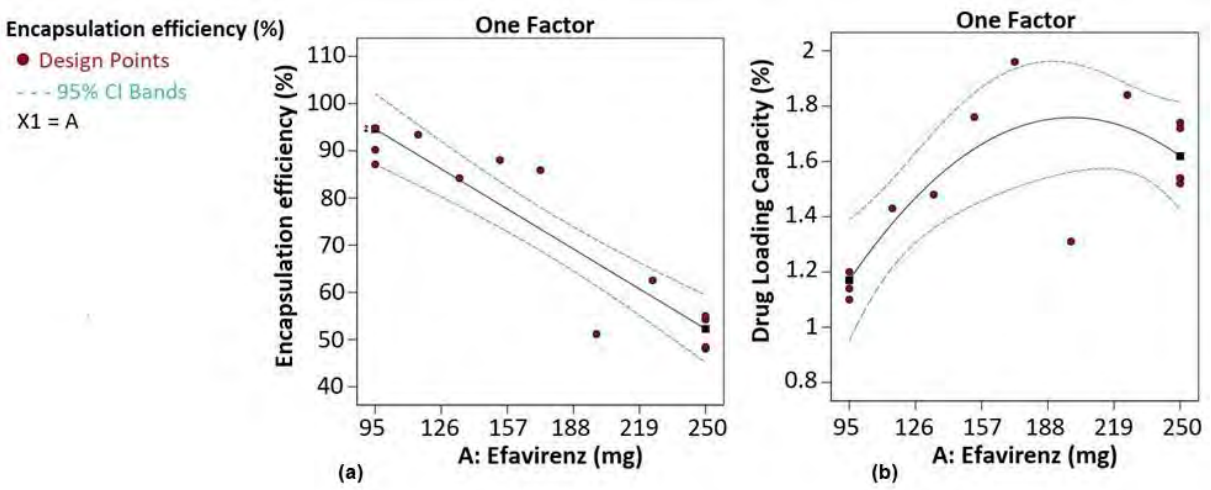

Figure 20. *Encapsulation efficiency (a) and drug loading capacity (b) profiles.*

3.1.6.2. Model Validation

This section aims to confirm the prediction performance assumption of the models fitted to the encapsulation efficiency and the drug loading capacity. The target was also to obtain an optimized amount of efavirenz that could achieve both high encapsulation efficiency and drug loading capacity in blend 1. Hence, the optimization criteria consisted of maximizing encapsulation efficiency and drug loading capacity values with the amount of efavirenz minimized to avoid excess undissolved drug. The software generated only one amount of drug that was formulated in blend 1 in triplicate. The formulation was performed using the method described in Section 2.1.2.4, by adding 135 mg of efavirenz to blend 1. Table 19 shows that the average value of the experimental data was within the range of the 95% prediction intervals, suggesting that the models fitted to the responses could be used to predict the encapsulation efficiency as well as the drug loading capacity. This amount of drug was selected for drug-release investigation in blend 1.

Table 19. *Optimized encapsulation efficiency and drug loading capacity*

	Response	Mean		95% Prediction	
		Predicted	Observed	95% PI Low	95% PI High
Blend 1-EFV 135	**EE%**	83.7808	87.4	72.7572	94.8044
	DLC%	1.53233	1.5	1.2386	1.82605

3.1.7. Characterization of Blank-LNC and EFV-LNC

3.1.7.1. Droplet Size and Shape Analysis

Both blank-LNC and EFV-LNC were characterized by very small droplets of various sizes, as demonstrated by DLS (dynamic light scattering) Gaussian distribution in Figure 21A. Moreover, the average size of blank-LNC was around 42 nm, which increased to over 80 nm following EFV encapsulation. This was confirmed by TEM analysis that describes, as depicted in Figure 21B, normal distribution peaks at around 30 to 50 nm (Figure 21C) and 50 to 80 nm (Figure 21E) for blank-LNC and EFV-LNC, respectively. Moreover, as illustrated in Figure 21B,D, different particle shapes were observed from the TEM images, the majority of the particles being nearly ellipsoidal and spherical, as already observed in the previous studies [69,181]. It is noteworthy to mention that EFV encapsulation resulted in the growth of particle shapes, as shown in the TEM images.

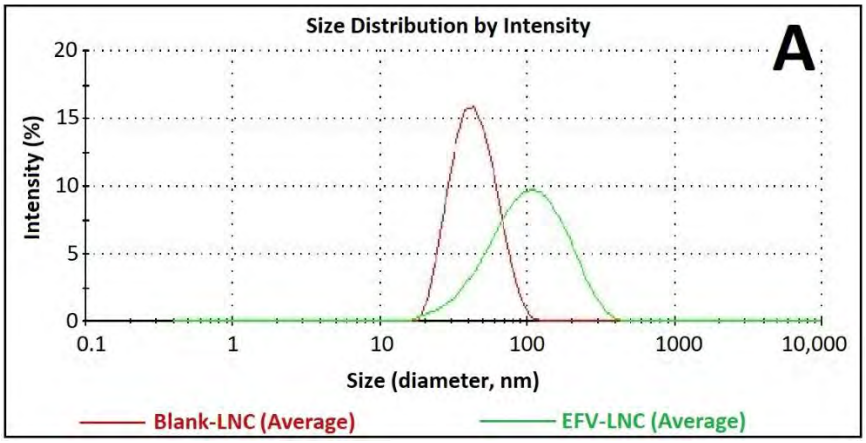

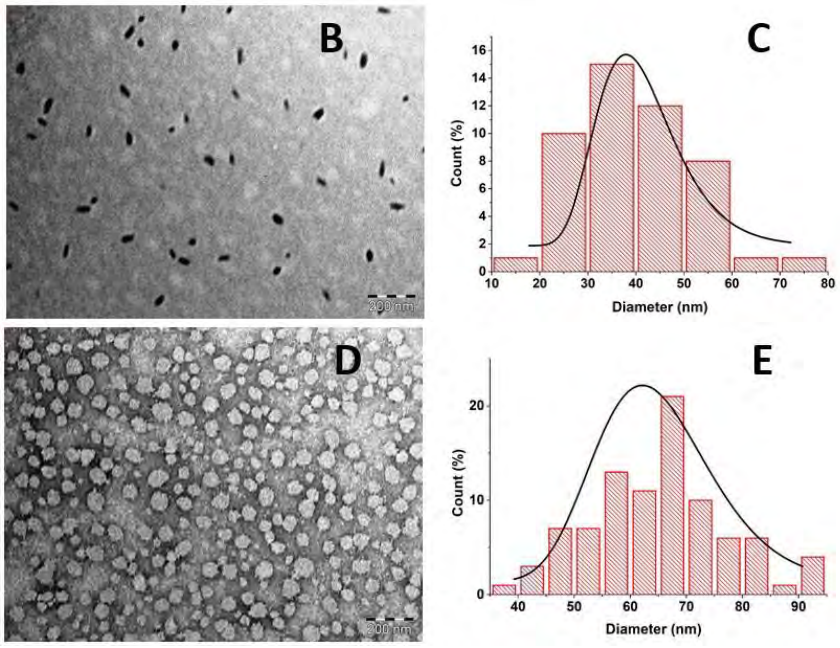

Figure 21. *DLS average-particle-size distribution (triplicate) of blank-LNC and EFV-LNC (A), TEM images (200 nm scale) of blank-LNC (B) and EFV-LNC (D), TEM particle-size distribution by Image-J of blank-LNC (C) and EFV-LNC (E).*

3.1.7.2. Diffraction Scanning Calorimetry

DSC analysis was performed in order to investigate any possible drug-excipient interaction, as well as any change in the crystalline nature of the drug as LNCs form. Figure 22 shows the overlaid thermograms of efavirenz, physical mixture of LNC components, blank-LNC and EFV-LNC. At first sight, an endothermic peak at approximately 138 °C, associated with 48.875 J/g enthalpy, indicated the melting point of efavirenz, in agreement with the previous studies [182–184]. The observed sharp peak suggests high drug purity and crystallinity. On the other hand, the shift in the appearance of this peak from 138.67 °C to 122.33 °C in the physical mixture thermogram suggests possible interactions that could be a result of hydrogen bond formations between the drug and the raw materials. However, it could also be a result of the amorphous form formation as EFV quickly dissolves in the physical mixture, thus accounting for a low melting energy consumption (ΔH = 6.8802 J/g). Such outcomes have been reported when EFV was formulated in polyvibylpyrrolidone or in a binary mixture with nicotinamide [182,183]. Interestingly, no major peak has been observed either for blank-LNC or for EFV-LNC over the scanned temperature range, suggesting an excellent encapsulation of efavirenz in an amorphous or molecular dispersed nature with the advantage of enhancing its solubility and dissolution in biological media.

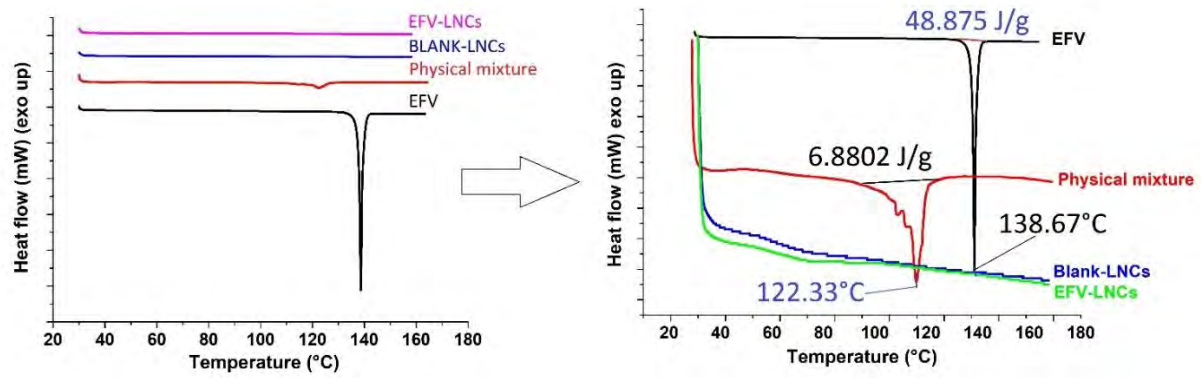

Figure 22. *DSC thermograms.*

3.1.7.3. Fourrier Transform Infrared Spectroscopy

The structure of EFV includes a secondary amine that may act as a weak Bronsted–Lowry acid and a carbonyl group (C=O), as well as a C–O–C group, which are acceptor groups. In addition, MCT oil, Tween 80 and soy lecithin have in common carbonyl groups as acceptors of hydrogen bonding, which could favor some interactions with EFV [185]. These interactions may be expressed by the shifting or broadening of bands, disappearance of peaks or intensity alterations [186]. Hence, the FTIR spectra were recorded to assess and scout possible chemical interactions between the pure drug and raw materials in the developed nanocapsules.

The different spectra obtained are shown in Figure 23. As it can be observed from the graphs, LNC formulations exhibit intense characteristic bands of aliphatic groups, which are a clear contribution of the structural composition of soy lecithin, Tween 80 and MCT oil. The C–H stretch of saturated fatty acids was observed at around 2950–2840 cm^{-1}. Bands at 1750–1745 cm^{-1} and 1416 cm^{-1}, respectively, revealed the presence of carbonyl functions (C=O) and C–O–C stretching vibrations, which are both part of the structure of EFV and the raw materials. The broad band visible in the range of 3700–3000 cm^{-1} is associated with O–H stretching in the spectra of Tween 80 and soy lecithin. On the other hand, all the expected signals for pure EFV were present. They encompass the N–H stretching vibrations and N–H bending vibrations of benzoxazin-2-one ring, respectively, at about 3320 cm^{-1} and 1600 cm^{-1}; the exocyclic tricyclic triple bond (–C≡C–) at around 2250 cm^{-1}; and C–F and C–Cl stretching near 1250 cm^{-1} and 1038, respectively, in agreement with the previous studies [186–189].

As clearly displayed in Figure 8, the disappearance of N–H stretching and bending vibrations, as well as a plunge in the intensity of carbonyl group stretches, occurred in the EFV-based LNC and the physical mixture. These events could result from the physical interactions between EFV

and the raw materials, suggesting intramolecular hydrogen bonding. They could also be a result of the transition from the crystalline form of EFV to an amorphous form, as confirmed by the XRD and DSC data. Moreover, the O–H stretch of the terminal hydroxyl group of Tween 80 and soy lecithin vanished in the developed nanocapsules and the physical mixture, thus indicating intramolecular hydrogen bonding between the drug and these two raw materials. The absence of the characteristic peak of the exocyclic tricyclic triple bond (–C≡C–) that appeared at around 2250 cm^{-1} indicates the successful entrapment of EFV in the lipid core of LNC.

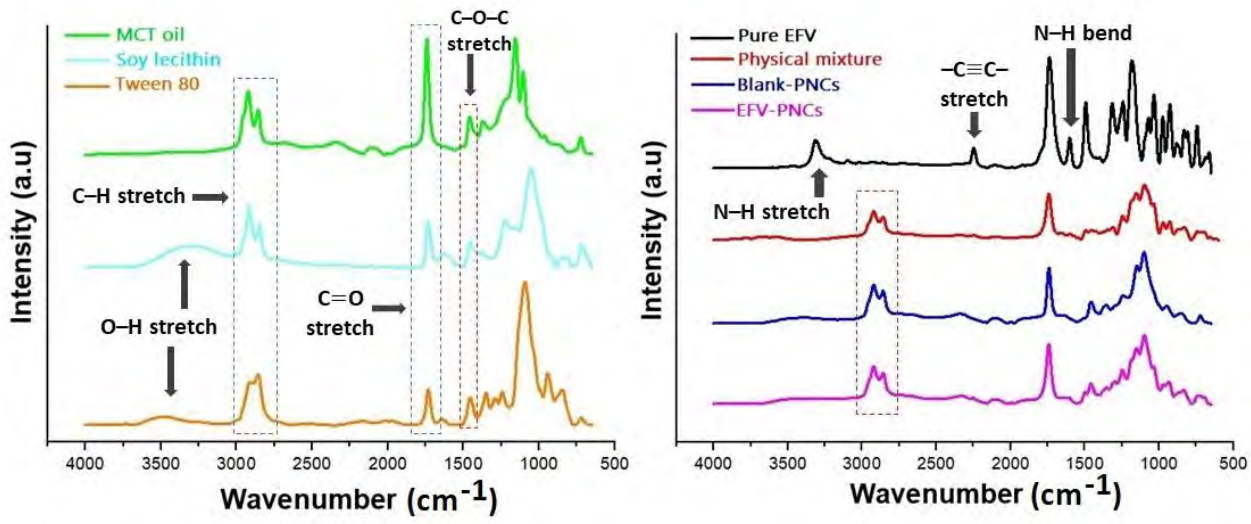

Figure 23. *FTIR spectra of LNC formulations and raw materials.*

3.1.7.4. X-ray Diffraction

Changes in the crystalline structure of EFV in lipid nanocapsules was ascertained by using powder X-ray diffraction. Overall, the LNC formulation influenced EFV crystallinity. The diffractograms sketched in Figure 24 unveil a very crystalline state (88.1%) of efavirenz (EFV) characterized by remarkable peaks in 2 tetha diffraction angle ranges of almost 8 to 25°, in accordance with the previous investigations [182,186]. The blank-LNC formulation exhibited few diffraction peaks with a relatively low crystallinity of 23.7%, which increased to 52.3% following EFV encapsulation. The disappearance of EFV characteristic diffraction peaks in the EFV-LNC formulation indicates that EFV was successfully entrapped in the LNC matrix. This result corroborates with the previous DSC conclusions and further supports the EFV transformation into its amorphous or molecular dispersed nature, hence accounting for the enhancement of its solubility.

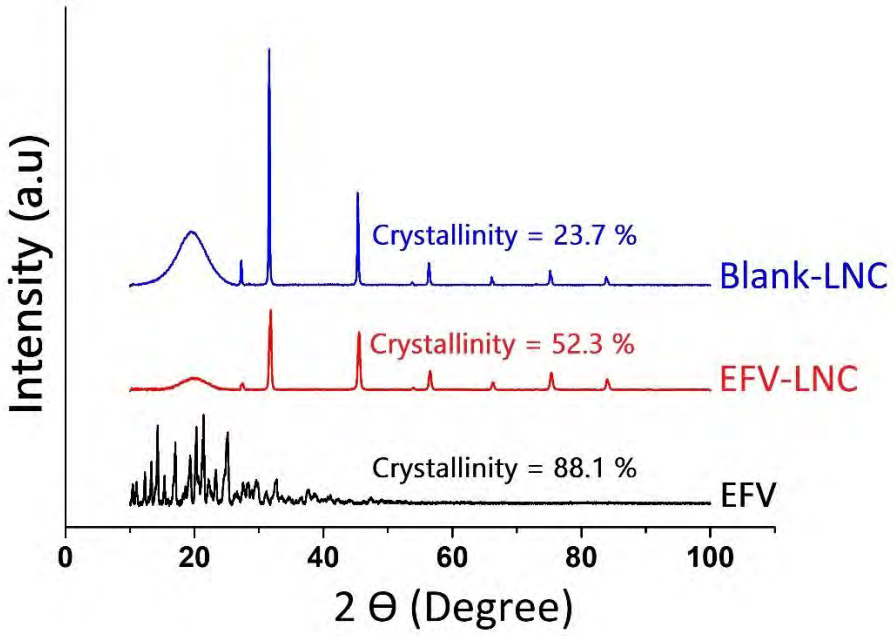

Figure 24. *XRD diffractograms of blank-LNC, EFV-LNCs and EFV.*

3.1.7.5. Energy-Dispersive X-ray Spectroscopy

Energy-dispersive X-ray spectroscopy was used to probe the qualitative composition of freeze-dried EFV-LNC and freeze-dried blank-LNC, as compared to that of free efavirenz. The EDS spectra of both blank-LNC and EFV-LNC were characterized in common by the presence of carbon, chlorine, oxygen, sodium and phosphorus (Figure 25b,c). Fluorine was observed only in EFV-LNC as being characteristic of the structure of efavirenz (Figure 25a,c). Phosphorus characterized the LNC formulations as being a key element in the hydrophilic heads of phospholipids that are organized along with the hydrophilic heads of the ionic surfactant (Tween 80) to form the rigid shell of LNC [69,190].

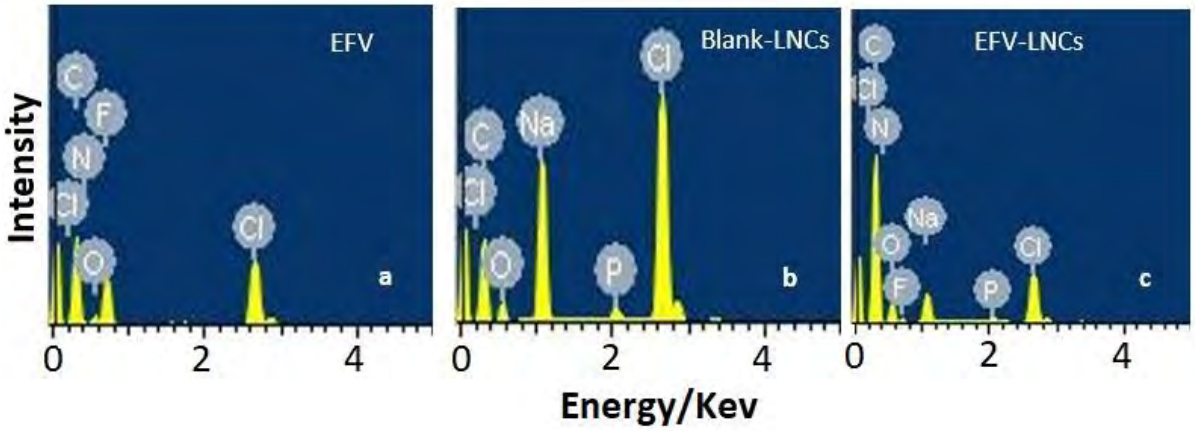

Figure 25. *EDS spectra illustrating the elemental composition of free efavirenz (a) and LNC formulations (b,c).*

3.1.8. In Vitro Release

The choice of a model drug is very critical in the design of a drug delivery system, given that its stability and activity must be maintained following encapsulation. Many factors, especially the components used to design the carrier, could interact with the drug and negatively affect the stability of its structure as well as its biological activity [191]. To verify whether the structure of efavirenz remained intact following encapsulation in LNC, the release medium containing the liberated drug was collected and the drug spectrum was recorded using a UV spectrometer. As displayed in Figure 26, no change was observed in the efavirenz spectrum (λmax = 247 nm) following drug release, as compared to its spectrum before drug release, hence suggesting that the structural integrity of the drug was preserved during the entire EFV-LNC manufacturing process.

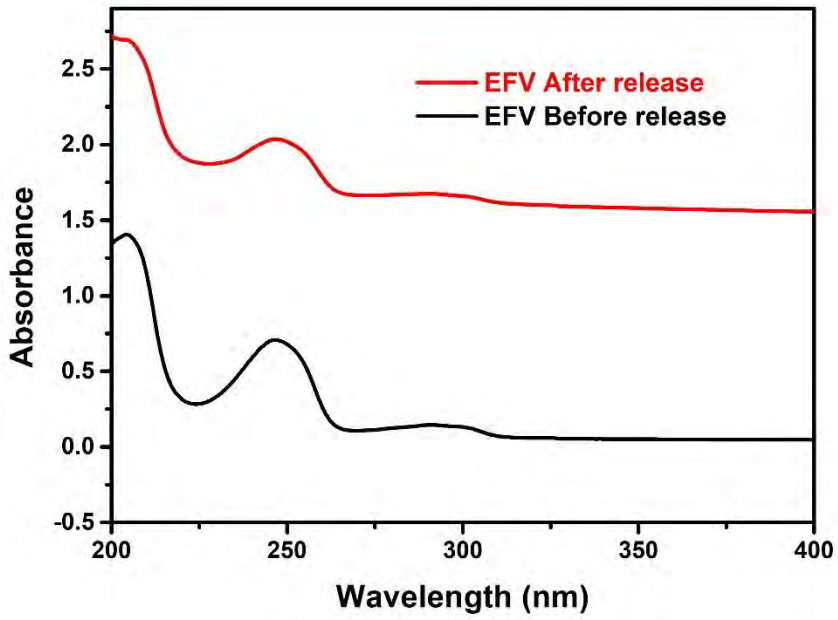

Figure 26. *Efavirenz UV spectra before encapsulation and after release from EFV-LNC.*

The in vitro release profiles of EFV-LNC and free EFV are sketched in Figure 27. Overall, the release profile in pH 7 was higher than in pH 4 for EFV-LNC. As illustrated by the interactive graphs below (Figure 27a), free EFV was quickly released from the dialysis bags, as compared to EFV-LNC both in pH 4 and 7, reaching up to around 40% release in 74 h. This could be explained by the fact that, before crossing the dialysis bag barrier, encapsulated EFV had to be first liberated from the LNC carrier.

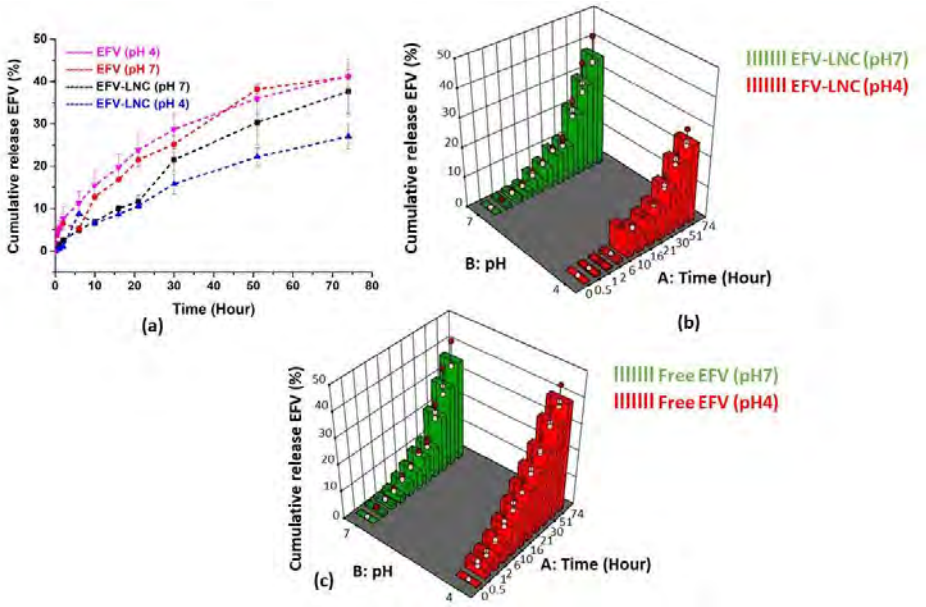

Figure 27. *Interactive plot (a) and 3D surface plots of EFV-LNC (b) and free EFV (c) in vitro release profiles in both pH 7 and pH 4.*

On the other hand, EFV-LNC liberated the drug quicker in pH 7 than in pH 4, as shown by the interactive plot (Figure 27a). However, both release profiles in pH 4 and 7 followed an upward trend up to the end of the experiment, suggesting a prolonged release that could be complete if more time was set up. From a statistical point of view, the analysis of variance revealed that both the release time and pH of the release medium significantly affected EFV liberation from the LNCs (p-value < 0.05). Finally, as outlined in the normal plot of residuals (Figure 28a for EFV-LNC and Figure 28b for free EFV), a linear regression was observed, therefore supporting the fact that the residuals were normally distributed.

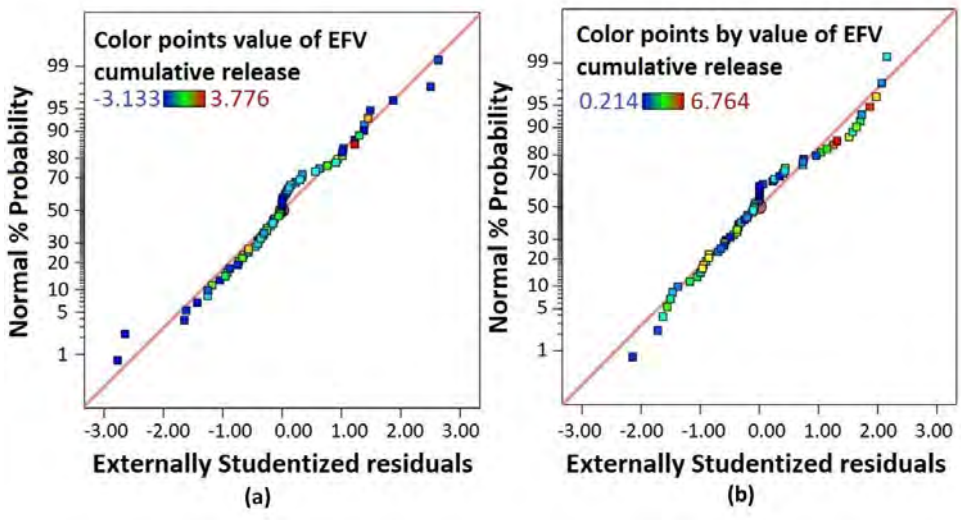

Figure 28. *Normal plot of residuals for EFV-LNC (a) and for free EFV (b).*

3.1.9. Stability Studies

The developed LNCs are not true solutions and are, rather, a homogenous colloidal system consisting of a dispersion of different substances; hence, they are likely to lose their stability over time. Particles in a colloidal system are influenced by diverse types of forces that could either foster their stability or cause their flocculation. According to the Derjaguin, Landau, Verwey and Overbeek theory, these forces include the Van Der Walls attraction forces and the repulsive electric double-layer forces [192]. Briefly, if the electrostatic repulsive forces are higher than the attractive ones, no flocculation is expected to occur, and the system can be considered as stable. This phenomenon is known as electrostatic stabilization [193]. In other words, when particles in suspension have a similar electrostatic charge on the surface, the system stability increases as no attraction occurs between them. As depicted in the bar charts in Figure 29, the EFV-LNC remains stable over 28 days of stability studies as referring to the zeta potential measurement values (Figure 29c), knowing that zeta potential represents the electric surface properties of particles in a colloidal system [194,195]. On the other hand, the droplet size remained stable (Figure 29a) and no change in the polydispersity index was observed over the period of experimentation (Figure 29b).

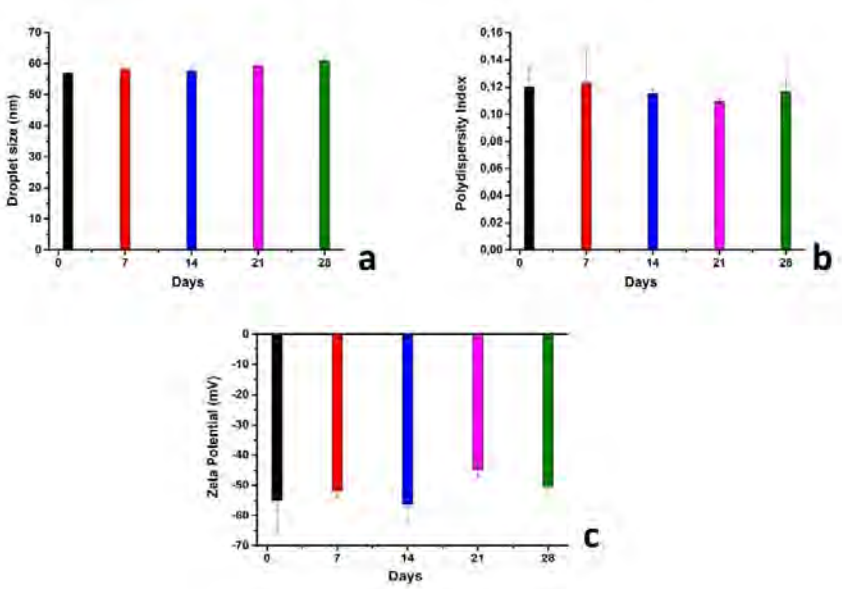

Figure 29. *Droplet size (a), Polydispersity index (b) and Zeta potential (c) values over 28 days of EFV-LNC stability evaluation.*

3.1.10. Conclusion

The present work reported the successful encapsulation of EFV in lipid nanocapsules and its prolonged release from this matrix. The design expert software allowed the building of

polynomial models that could predict the different characteristics of these nanomaterials, namely, the particle size, polydispersity index and zeta potential. Different characterization techniques confirmed the entrapment of EFV in the lipid nanocapsules and its transformation into its amorphous state, therefore enhancing its solubility. Among them, FTIR revealed some chemical interactions, assumed as hydrogen bonds, between the drug and the different starting materials owing to their respective structures. Stability studies revealed that the developed LNC were quite stable over the period of experimentation. Overall, lipid nanocapsules stand as promising delivery system for the improvement of EFV biopharmaceutical properties. Further investigations are ongoing in our laboratories to evaluate the antiviral activities of the formulated nanocapsules as compared to that of the free EFV.

Project II: "Design, Synthesis, Manufacture, Characterization and Evaluation of Lipid Nanocapsules-Hydrogel Composite"

A manuscript entitled "Lipid Nanocapsules in chitosan-g-iota carrageenan-g-poly (acrylamide-co-acrylic acid) hydrogel scaffold, for Pulmonary Drug Delivery System: Design, Synthesis, Manufacture, Characterization and Evaluation", based on results presented in this second project, is underway to be submitted for publication in ACS Applied Materials & Interfaces.

3. RESULTS AND DISCUSSION

3.2. Results and Discussion for Project II

3.2.1. EFV-LNC preparation

EFV-LNC were produced in order to be encapsulated in chitosan-g-iota carrageenan-g-poly (acrylamide-co-acrylic acid) hydrogel (CS/iCar-p(AAm-co-AA)). Hence, an optimized formulation of EFV-LNC developed in the first project, was prepared using the phase inversion method [69,162]. The obtained EFV-LNC were characterized for their particles size (PS), polydispersity index (PDI) and zeta potential (ZP). The average values of these parameters turned out to be around 57 nm, 0.148 and -54.9, respectively and aligned with results observed in the previous study.

3.2.2. Synthesis, optimization and statistical analysis of CS-iCar-p(AAm-co-AA) hydrogel

CS-iCar-p(AAm-co-AA) was synthesized by free radical co-polymerization method and the Design Expert software version 13.0 (Stat-Ease, Inc., Minneapolis, MN, USA) was used for optimization and statistical analysis. The I-optmial mixture design of experiments which was considered for this study generated 35 different hydrogel formulations that were run using the method described in section 2.2.2.4. Table 20 depicts the composition of each of them along with their corresponding swelling capacity that was considered as the response for optimization. The swelling capacity is expressed in percentage and corresponds to the ratio between the amount of absorbed water (g) and the amount of hydrogel (g).

Table 20. *Hydrogels formulations with their corresponding swelling capacity*

	Input variables (%)					Response (%)
Run	**Iota-carrageenan**	**Chitosan**	**Acrylic acid**	**Acrylamide**	**MBA**	**Swelling capacity (%)**
	A	**B**	**C**	**D**	**E**	
1	4,72	4,79	49,05	40,44	1,00	3696,00
2	5,82	5,64	41,49	44,05	3,00	6044,00
3	6,00	4,30	40,00	47,85	1,85	20700,00

4	3,26	3,00	50,98	40,00	2,76	10533,00
5	4,72	4,79	49,05	40,44	1,00	4605,00
6	3,00	3,13	43,59	49,28	1,00	6600,00
7	4,47	4,18	40,51	47,84	3,00	1594,00
8	3,00	3,00	40,00	53,00	1,00	34251,00
9	4,52	3,00	43,74	46,56	2,19	5970,00
10	5,74	3,56	46,89	41,07	2,75	43443,00
11	3,09	3,00	46,82	45,93	1,15	2064,00
12	3,41	3,00	47,79	42,80	3,00	3192,00
13	4,81	3,00	40,00	51,19	1,00	2219,00
14	3,00	3,00	40,98	50,03	3,00	27212,00
15	3,00	4,54	40,00	50,41	2,05	600,00
16	3,00	6,00	40,00	50,00	1,00	10950,00
17	3,00	4,25	45,34	44,41	3,00	1860,00
18	3,00	3,39	50,08	42,53	1,00	27648,00
19	3,74	5,60	47,87	40,00	2,79	3553,33
20	3,00	4,87	46,29	44,75	1,10	2933,33
21	4,52	3,00	43,74	46,56	2,19	4300,00
22	4,47	4,18	40,51	47,84	3,00	34816,00
23	3,00	3,33	52,68	40,00	1,00	284,00
24	4,30	6,00	43,56	44,43	1,70	8650,00
25	4,30	6,00	43,56	44,43	1,70	7352,00
26	3,00	4,54	40,00	50,41	2,05	510,00
27	6,00	5,09	44,04	41,88	3,00	8800,00
28	3,00	5,96	47,74	42,31	1,00	3344,00
29	6,00	6,00	46,37	40,00	1,63	5866,00
30	6,00	3,56	44,84	44,60	1,00	32468,00
31	3,00	6,00	50,00	40,00	1,00	721,00
32	6,00	6,00	40,33	46,68	1,00	3290,00
33	5,83	3,00	50,14	40,00	1,03	19440,00
34	3,14	6,00	40,45	47,41	3,00	605,00
35	6,00	3,00	40,00	48,00	3,00	14452,00

Different polynomial models were evaluated, and the linear model provided more precision in predicting data with approximately similar and relatively small standard errors (< 0.5 σ, where σ is the estimated variability of the data) across the region of interest (Figure 30).

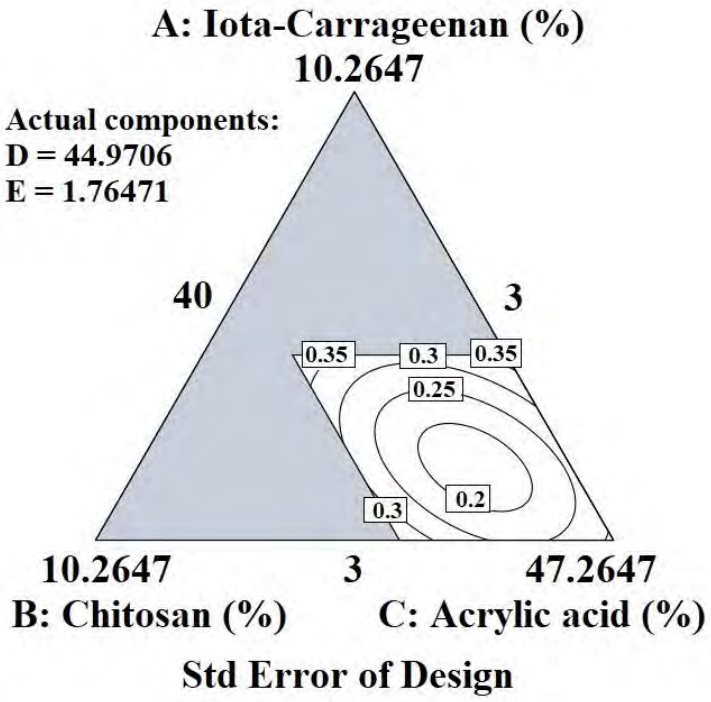

Figure 30. *Contour plot of the standard error at different points in the design space.*

The experimental data were fitted to different polynomial models as shown in Table 21, and among them, the linear model was automatically suggested as the best fit since its PRESS value was the lowest and its small sequential p-value suggested the model to be relatively significant. In fact, lowest PRESS values are assumed to be associated to better prediction ability [168].

Table 21. *Analysis of variance of fitted models*

Model	Sequential p-value	Lack of Fit p-value	Adjusted R^2	Predicted R^2	PRESS	
Linear	**0,0512**	**0,3168**	**0,1643**	**-0,0344**	**61,47**	**Suggested**
Quadratic	0,7921	0,2329	0,0374	-0,8826	111,88	
Special Cubic	0,4275	0,1962	0,0943	-8,4271	560,25	
Cubic	0,1962		0,444		*	**Aliased**

3.2.3. Effect of the different components on the swelling capacity

The swelling capacity was automatically fitted to a Scheffe's linear model as expressed by the following equation:

Equation 12. *Swelling Capacity (%SC)*

$$\%SC = 0.556464 \times A + -0.241395 \times B + 0.0694467 \times C + 0.0907205 \times D + 0.0431736 \times E \quad \textbf{(Eq. 12)}$$

where factors A, B, C, D and E correspond respectively to iota-carrageenan, chitosan, acrylic acid, acrylamide and *N,N*-methylene bisacrylamide.

This model is associated to very low adjusted and predicted R-squared making it not strong for predictions. Hence, it was subjected to model p-value test to assess its prediction ability hypothesis and to lack of fit F-test to evaluate the variation of data around it. As shown in Table…above, this linear model was found to be relatively significant (sequential p-value = 0.0512) meaning that it could be used to predict data. Besides, its insignificant lack of fit (p-value = 0.3168) suggested that its predicted data fit to the actual experimental response data[171,172,196]. Furthermore, since the value of adequate precision must be greater than "4", the observed adequate precision of 5.497 implies a good signal and could therefore explain the signal-to-noise ratio for excellent navigation in the design space [174].

On the other hand, as depicted in Table 19, the swelling capacity of the synthesized hydrogels ranged from 284 to 43443 % (2.84 g to 434.43 g of water per g of hydrogel). This one was affected by changes in the hydrogels components proportions. As shown in Figure 31, the swelling capacity increases as the proportion of iota-carrageenan rises and that of chitosan falls. In the same way, it was observed that the swelling capacity goes up as the proportions of acrylic acid, acrylamide and MBA decrease. This can be accounted for by the fact that the higher the amounts of monomers and crosslinker in a hydrogel formulation, the higher the crosslinking density is, which makes it hard for the resulting scaffold to open in order to absorb water.

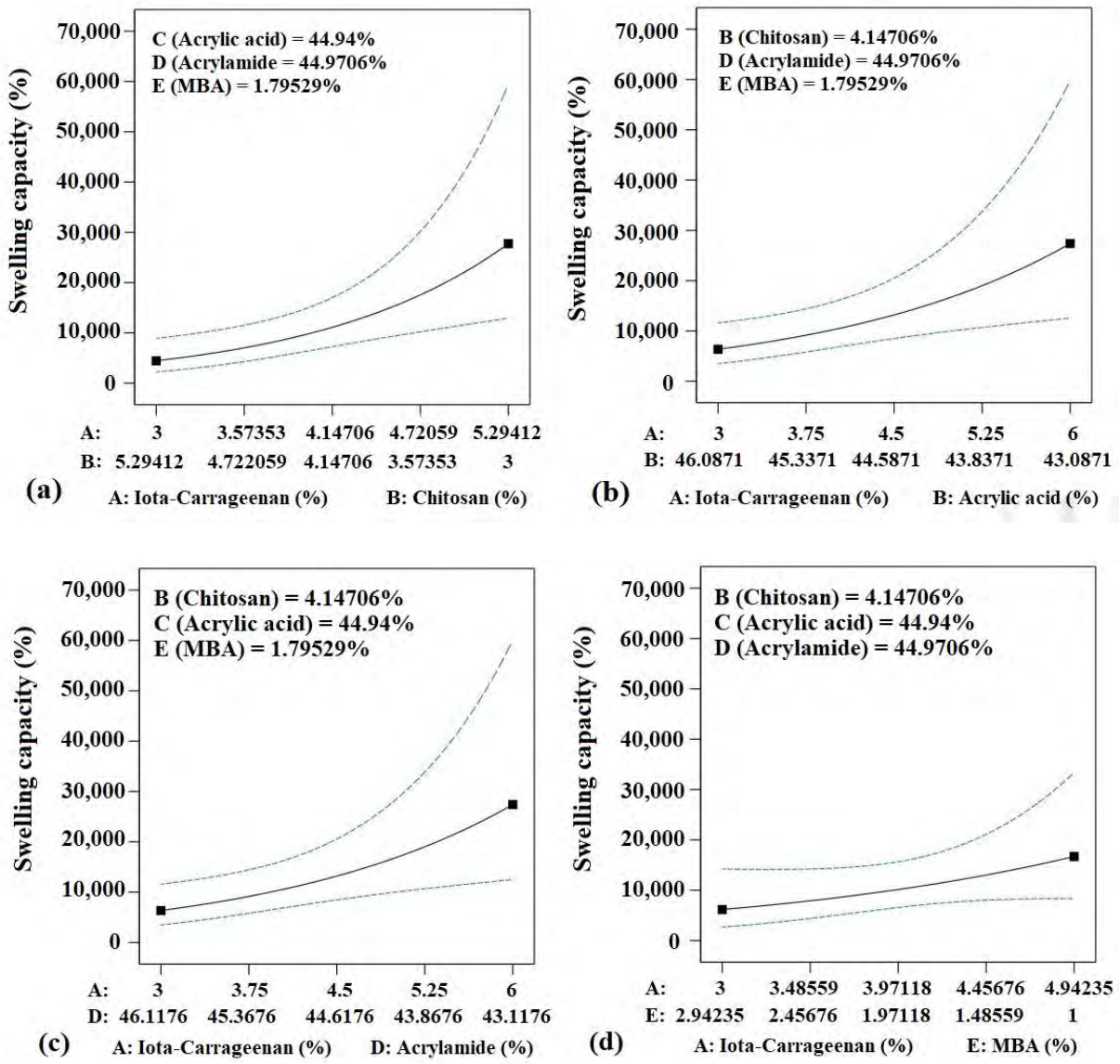

Figure 31. *Effects of starting materials proportions on hydrogel swelling capacity, namely by changing proportions of iota-carrageenan and chitosan (a), iota-carrageenan and acrylic acid (b), iota-carrageenan and acrylamide (d) and iota-carrageenan and N'N'-methylene bisacrylamide (MBA).*

3.2.4. Model optimization and confirmation

To confirm the prediction ability of the built-up linear model, the design expert software generated five different formulations with the optimization criterion being swelling ratio maximization. As shown in Table 22 the formulation with the highest desirability was selected and run in triplicate. Table 23 shows that the average value of the experimental data obtained was within the range of the 95% prediction intervals that confirmed that this linear model could predict the swelling capacity. This formulation was therefore designated for further experiments.

Table 22. *Automatically generated hydrogel composition batches for model optimisation and confirmation*

Number	i-Car	CS	AA	AAm	MBA	SR	Desirability	
1	**6.00**	**3.00**	**40.00**	**50.00**	**1.00**	**44445.79**	**0.86**	**Selected**
2	6.00	3.00	50.00	40.00	1.00	35928.51	0.82	
3	5.44	3.00	40.00	50.56	1.00	34202.18	0.81	
4	5.44	3.00	50.56	40.00	1.00	27319.05	0.76	
5	4.40	3.99	44.31	44.31	3.00	12553.68	0.61	

Table 23. *Observed swelling ratio mean against the prediction interval*

	Response	**Mean**		**95% Prediction**	
		Predicted	**Observed**	**95% PI low**	**95% PI high**
Formulation 1	Swelling capacity	44445.8	30424.7	3258.07	140709

3.2.5. Potential mechanism of formation of the hydrogel

At higher temperature, ammonium persulfate (APS) generates free radicals, which interact with either the hydroxyl or the amide groups of polysaccharides (chitosan and iota-carrageenan). This interaction results in formation of free radical sites on the backbone of these polymers as illustrated in Figure 32. The addition of acrylamide (AAm), acrylic acid (AA), and *N'N'*-methylene bisacrylamide (MBA) (compounds with unsaturated carbon chains) to the activated polysaccharides result into a random reaction with their free radical sites as described in the suggested scheme of the free radical copolymerization reaction sketched in Figure 33. Since *N'N'*-methylene bisacrylamide is a bifunctional compound, it is likely to be responsible of the formation of polymer-polymer network, which would result in the enhancement of the viscosity of the reactional mixture. The addition of acetone at the end of the reaction allows dehydration

of the produced hydrogel and remove the compounds that didn't react in the formation of the hydrogel [165,197].

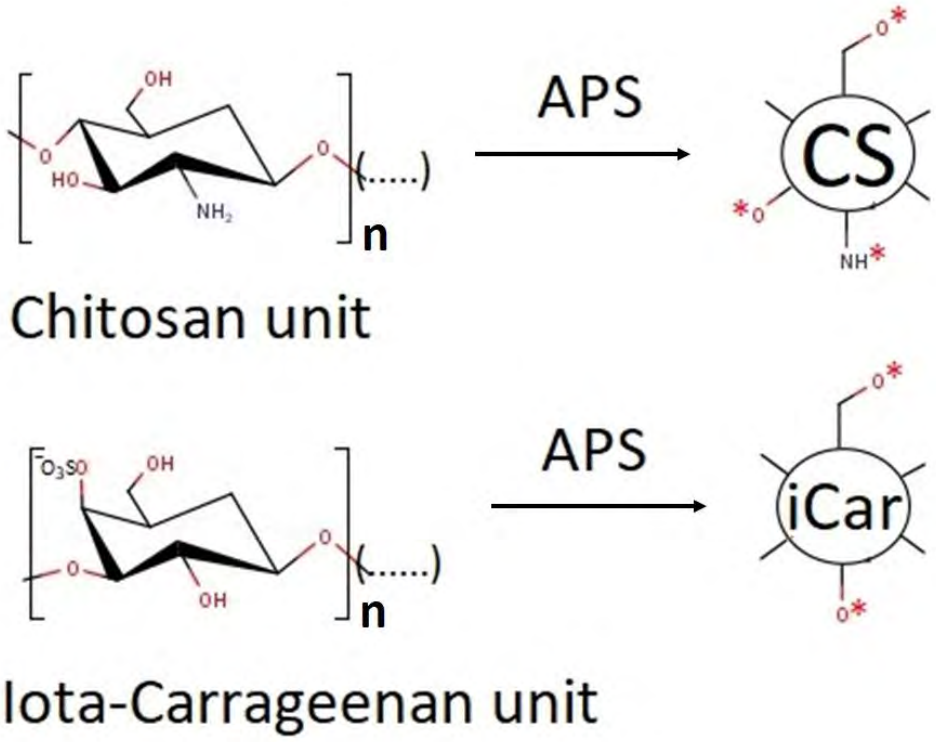

Figure 32. *Formation of free radical sites on chitosan (a) and iota-carrageenan (b) backbones under ammonium persulfate (APS) initiation.*

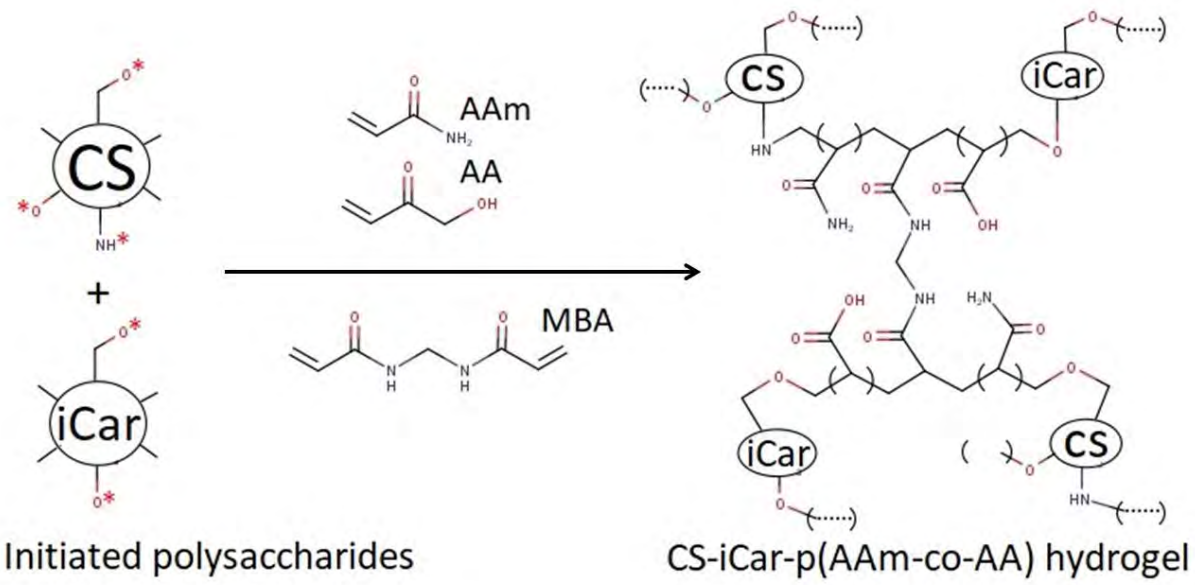

Figure 33. *Plausible reactional mechanism of CS-iCar-p(AAm-co-AA) hydrogel.*

3.2.6. Development of EFV-LNC- CS-iCar-p(AAm-co-AA) hydrogel composite

This section aimed at developing EFV-LNC-CS-iCar-p(AAm-co-AA) hydrogel composite following the encapsulation method previously described in section 2.2.2.5. In order to determine the effect of EFV-LNC concentration on their entrapment into CS-iCar-p(AAm-co-AA) hydrogel, the 13 runs generated through the D-optimal (custom) randomized design were realised and experimental data are summarized in Figure 34. It is conspicuously clear that as the concentration of EFV in LNC increases, the encapsulation efficiency goes up too and reaches a broaden peak at around 55 to 60 mg/ml of EFV-LNC before it starts declining. These experimental data were fitted to a reduced quadratic model expressed by the following equation:

Equation 13. *LNC- CS-iCar-p(AAm-co-AA) hydrogel composite Encapsulation Efficiency (%EE)*

$\mathbf{\%EE} = 4.25921 + 1.45271 \times A + -0.0123934 \times A^2$ (**Eq. 13**) where A is the concentration of EFV in LNC.

To obtain an optimal concentration to be used for further studies and to assess the ability of this model to predict experimental data, maximisation of encapsulation efficiency was established as the optimisation criterion. A single run was generated by the software, suggesting the use of 58.61 mg/ml EFV-LNC associated with a predicted encapsulation efficiency of 46.83%. Briefly, 50 mg of the optimized hydrogel were soaked in 25 ml of a solution containing 58.61 mg/ml of EFV-LNC. Table 24 shows that the experimental data was within the range of the 95% prediction intervals; hence, this model could be used to predict the encapsulation efficiency.

Table 24. *Observed swelling ratio mean against the prediction interval*

	Response	**Mean**		**95% Prediction**	
		Predicted	**Observed**	**95% PI low**	**95% PI high**
Hydrogel + 58.61 mg/ml of EFV-LNCs	**Encapsulation efficiency**	46.83	53.04	28.03	65.63

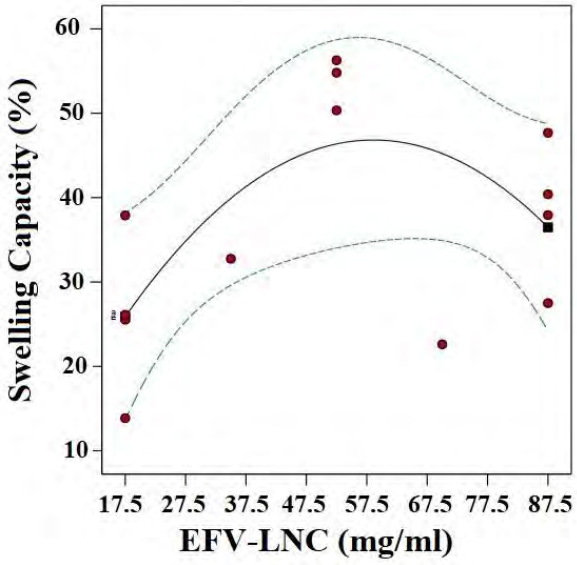

Figure 34. *Encapsulation efficiency of EVF-LNCs in poly (iCar/CS-co-AA/.AAm) based hydrogel.*

3.2.7. Characterization of poly (iCar/CS-co-AA/AAm) hydrogel and EFV-LNC-poly (iCar/CS-co-AA/AAm) hydrogel composite

3.2.7.1. Thermal gravimetric analysis

The thermal gravimetric analysis (TGA) of the synthesized hydrogel against that of raw materials described different thermal events that happened consecutively to hydrogel formation by chemical crosslinking.

Overall, the grafting of acrylamide and acrylic acid onto the polysaccharide backbones clearly resulted in a new decomposition behaviour in the produced hydrogel. As plotted in Figure 35a, the decomposition is split into several successive zones of weight loss. Of the two used polysaccharides, iota-carrageenan (iCar) turned out to have the quickest decomposition profile. By almost 160°C, iCar lost around 12% of its weight and a cumulative loss of 28% was observed in the second zone at around 208°C. On the other hand, chitosan (CS) resisted to heat and recorded first loss of about 10% only by nearly 237°C. However, when temperature rose to around 357°C, CS weight plunged, losing almost 39% in the second zone. Interestingly, the synthesized hydrogels presented a decomposition profile in the intersection of iCar and CS. Only around 7 to 8% weight loss was recorded in the first zone, while from about 106-178°C up to 600°C, the decomposition curve followed a nearly gradual trend. Thus, these decomposition profiles confirm the successful modification of polysaccharides, thereby affecting their thermal stability.

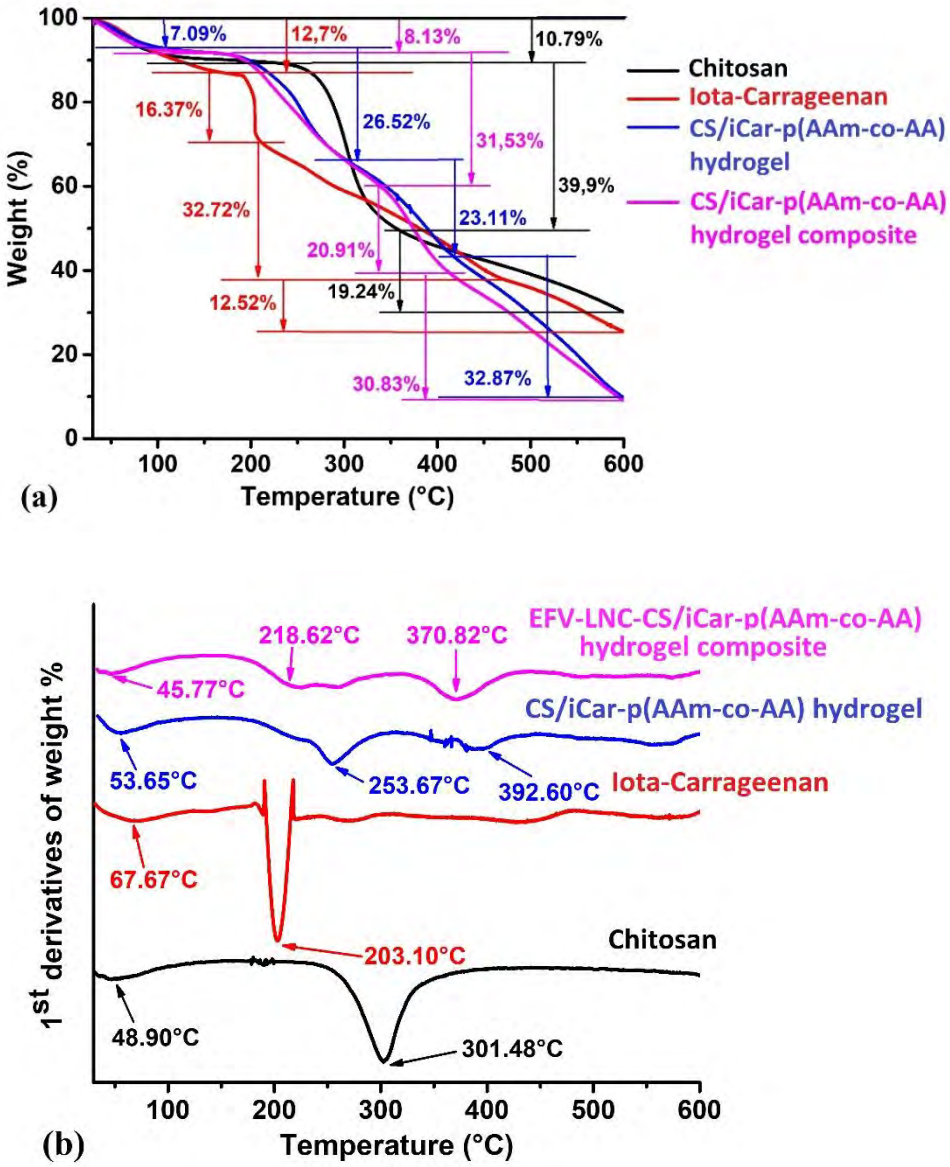

Figure 35. *Decomposition profiles of CS/iCar-p(AAm-co-AA) hydrogel, EFV-LNC-CS/iCar-p(AAm-co-AA) hydrogel composite, CS and iCar, showing weight loss as a function of temperature (a) and the first-order derivatives of their weight loss (b)*

3.2.7.2. Fourrier Transform Infrared Spectroscopy (FTIR)

As previously explained in the section about the potential mechanism of formation of poly CS/iCar-p(AAm-co-AA) hydrogel, both CS and iCar possess hydroxyl groups capable of interacting with double bonds (-C=C-) present in monomers and crosslinking agent. Moreover, the formation of the composite may yield possible interactions between EFV-LNC and CS/iCar-p(AAm-co-AA) hydrogel structure. Hence, to scout out any possible chemical interactions or changes in the final products (hydrogel and EFV-LNC hydrogel composite), their FTIR spectra were recorded in comparison with the one of raw materials.

As illustrated in Figure 36, iCar FTIR spectrum unveiled stretches corresponding to certain characteristic bonding present in iCar the structure, namely at 3369 cm^{-1}, 2912 cm^{-1}, 1214 cm^{-1}, 1157 cm^{-1} - 1066 cm^{-1} O-H, and 848 cm^{-1} – 802 cm^{-1}, respectively for C-H, O=S=O, C-O, C-O-C and O-SO3 stretches, in agreement with previous studies[198,199]. On the other side, chemical bonds in CS were expressed by the appearance of characteristic absorption bands at around 3450 cm^{-1} (amide I), 1580 cm^{-1} (-NH2 bending), 1320 cm^{-1} (amide III), 1160 cm^{-1} (C-O-C bridge), 1082 and 1032 cm^{-1} (C-O stretches), in agreement with other studies[200,201].

Moreover, while acrylic acid spectrum revealed bands at around 2987 cm^{-1} (O-H), 1694 cm^{-1} (C=O), 1634 cm^{-1} (C=C), functional groups in MBA appeared at around 3302 cm^{-1} (N-H), 1655 cm^{-1} (C=O) and 1538 cm^{-1} (C=C); and carbonyl and amide functions stretches at around 1657 and 3209-3344 cm^{-1} respectively, were characteristic of acrylamide spectrum[202,203].

The FTIR spectrum of the synthesized CS/iCar-p(AAm-co-AA) hydrogel was characterized by a broad stretch in the region 3300-3500 cm^{-1}, that could be attributed to O-H and N-H bonding. The sharp stretch at about 3300 cm^{-1} could be a good indication of C-H bonds present in the hydrogel structure. Besides, stretches in the region 1000 to 1200 indicate the C-O vibrations in the synthesized hydrogel. Stretches in the region 2000 – 2300 cm^{-1}, also present in CS and iCar, could be the first overtones of the C-O vibrations that are likely to appear due to the large thickness of the hydrogel or polysaccharides film. The peak at 1657 cm^{-1} reveals the presence of C=O bands in the hydrogel.

Furthermore, the FTIR spectrum of the synthesized EFV-LNC-CS/iCar-p(AAm-co-AA) hydrogel composite exhibited the same stretches present in CS/iCar-p(AAm-co-AA) hydrogel spectrum, apart from the bands in the region 200 – 2300 cm^{-1} that accounted for the possible largeness of the hydrogel or polysaccharides thickness. In addition, C-H bands (2950 – 2840 cm^{-1}), characteristic of aliphatic chains in saturated fatty acid were visible in EFV-LNC spectrum along with carbonyl group stretches (1750 – 1745 cm^{-1}).

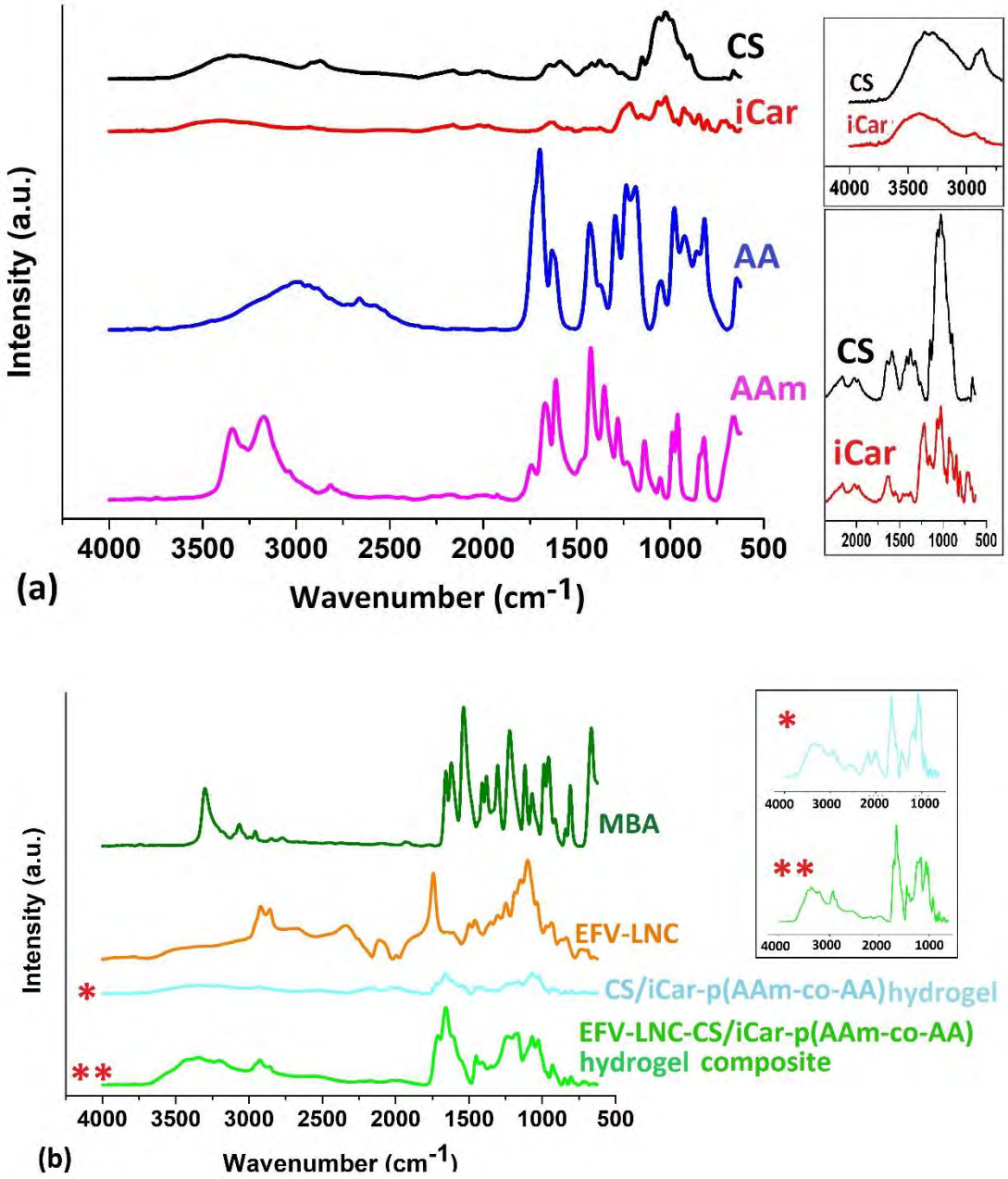

Figure 36. *(a) FTIR spectra of chitosan (CS), iota-carrageenan (iCar), acrylic acid (AA) and acrylamide (AAm). (b) FTIR spectra of N'N'Methyelene bisacrylamide (MBA), efavirenz loaded lipid nanocapsules (EFV-LNC), chitosan-g-iota carrageenan-g-poly (acrylamide-co-acrylic acid) hydrogel (CS/iCar-p(AAm-co-AA) hydrogel) and EFV-LNC-CS/iCar-p(AAm-co-AA) hydrogel composite.*

3.2.7.3. Scanning Electron Microscopy (SEM) and Energy Dispersive X-ray Spectroscopy (EDS)

The surface morphology and chemical elements composition of CS/iCar-p(AAm-co-AA) hydrogel and EFV-LNC-CS/iCar-p(AAm-co-AA) hydrogel composite was screened out on their freeze-dried samples using the SEM and EDS, respectively. Micrographs in Figure 37 (a

and b) highlight the presence of very rough and fibrous structures containing numerous pores that play a pivotal role in drug delivery[204]. On the other side, the EDS analysis of CS/iCar-p(AAm-co-AA) hydrogel unveil the presence of carbon, oxygen, nitrogen and sulfur, characteristic of chitosan (nitrogen) and carrageenan (sulfur) structures (Figure 37c), which were also present in the composite in addition to sodium and chlorine present in the LNC formulation (Figure 37d).

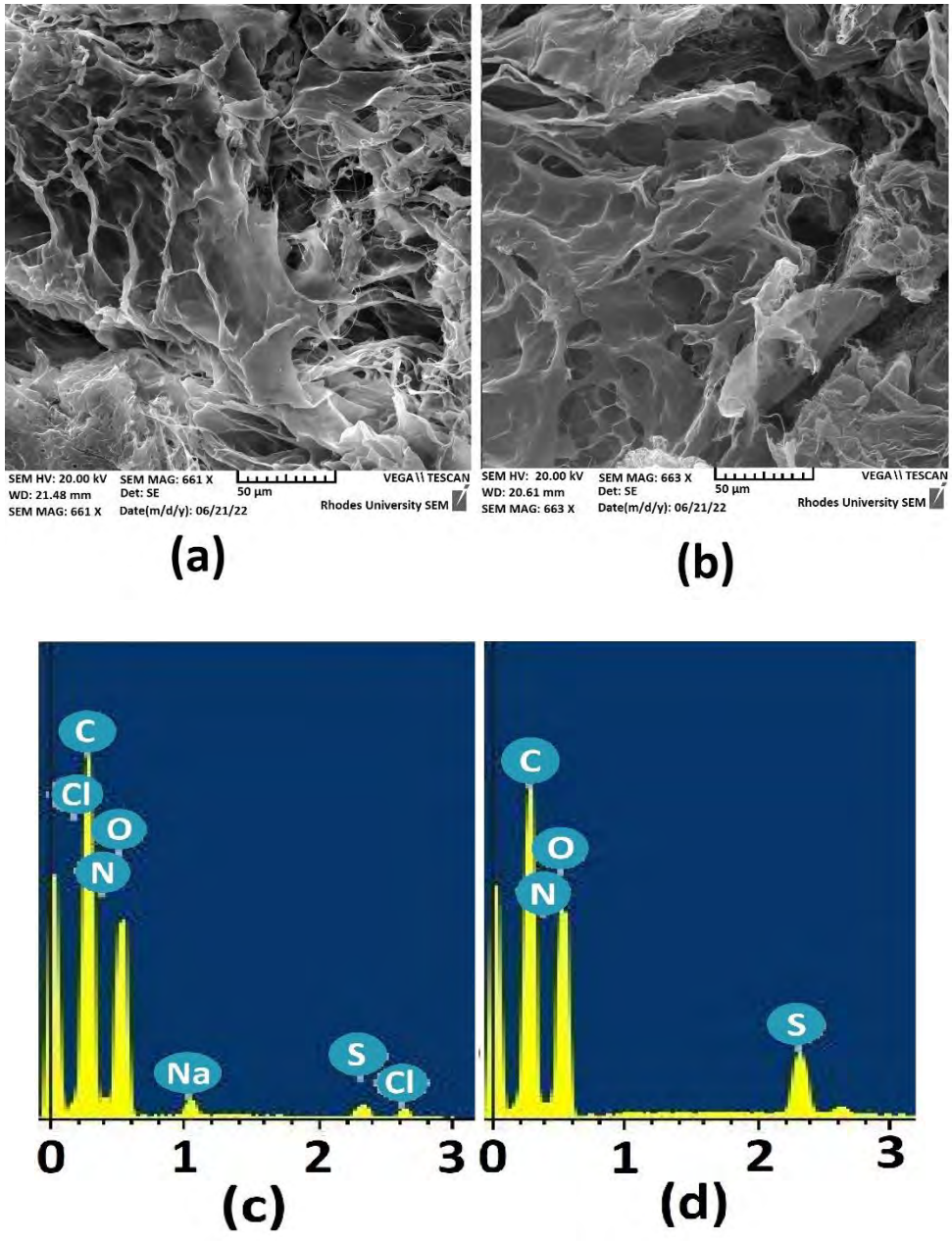

Figure 37. *SEM micrographs and EDS spectra of EFV-LNC-CS/iCar-p(AAm-co-AA) hydrogel (a and c) and CS/iCar-p(AAm-co-AA) hydrogel (b and d).*

3.2.7.4. Powder X-Ray Diffraction Spectroscopy

Powder x-ray diffraction spectroscopy (XRD) was used to assess possible crystallinity changes happened after synthesis of CS/iCar-p(AAm-co-AA) hydrogel and EFV-LNC CS/iCar-p(AAm-co-AA) hydrogel composite, in comparison with iCar and CS. Overall, as shown in Figure 38 CS diffractogram revealed a semi-crystalline structure with the highest crystallinity (14.31%) as compared to iCar (5.53%), which is known to be an amorphous compound, as confirmed by its XRD spectrum bellow. CS spectrum was characterized by the presence of a broad peak at 2 Θ angle around 19.8°. Since chitosan derives from chitin, a highly crystalline compound, its crystallinity depends on the degree of chitin's deacetylation that results into glucosamine units, as well as a decrease in the crystallinity[205,206]. Therefore, this modification in the crystalline structure of chitin could explain the semi-crystalline nature of chitosan. On the other side, synthesis of both CS/iCar-p(AAm-co-AA) hydrogel and EFV-LNC-CS/iCar-p(AAm-co-AA) hydrogel composite resulted in amorphous products with crystallinity respectively equals 2.13 and 4.04%, which further supports successful yield of chemical crosslinking between the different raw materials.

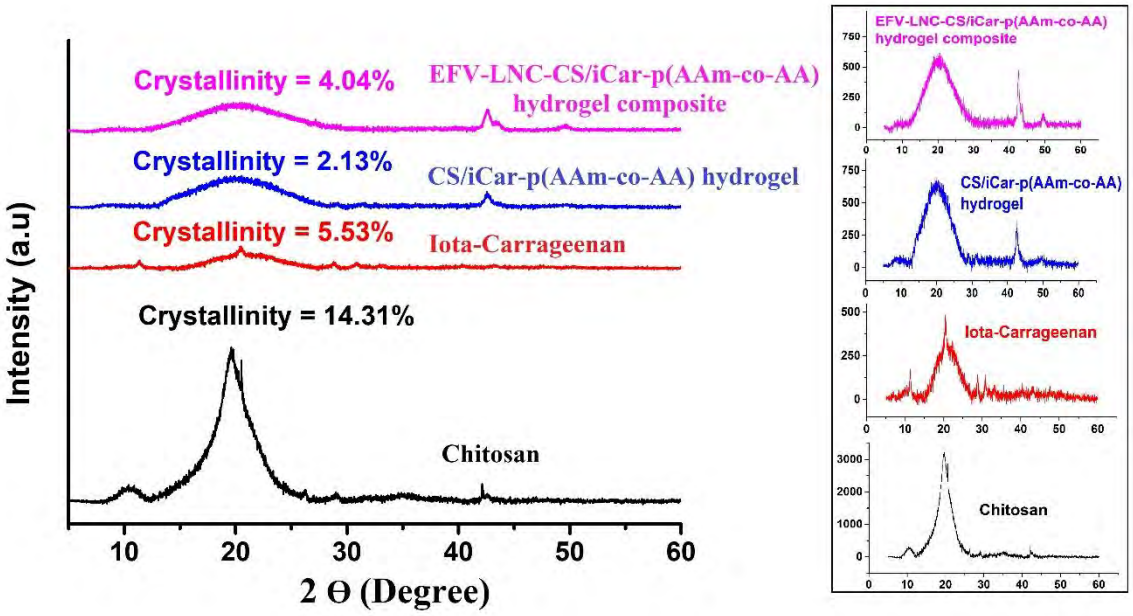

Figure 38. *XRD spectra of CS/iCar-p(AAm-co-AA) and EFV-LNC-CS/iCar-p(AAm-co-AA) as compared to the starting polysaccharides.*

3.2.8. *In vitro* Drug Release

The ability of the manufactured EFV-LNC-CS/iCar-p(AAm-co-AA) hydrogel composite to liberate the drug encapsulated in LNC, themselves entrapped in the hydrogel scaffold, was

determined by performing an *in vitro* release study using a 1% sodium lauryl sulfate (SLS) solution adjusted to pH 7 then to pH4. As sketched in Figure 39, EFV-LNC-CS/iCar-p(AAm-co-AA) hydrogel composite achieved a prolonged release of EFV over a period of 9 days (216 hours) in both pH 7 and 4. However, like in the first project on EFV-LNC presented in section 3.1.8, drug release in pH 7 was relatively higher (around 50%) than in pH 4 (around 40%), which could be explained by the high solubility of Efavirenz in neutral medium. Since, LNC as well as other lipid nanoparticles are known to achieve prolonged release of drugs encapsulated in their structure, their entrapment in hydrogel scaffold is likely to prolong the liberation of the encapsulated drug given the two barriers shelling it[107]. This suggests that LNC-CS/iCar-p(AAm-co-AA) hydrogel composite could be promising to deliver long lasting potential covid-19 treatment and avoid regular contact with the patient, therefore limiting the risk of contracting covid-19 infection.

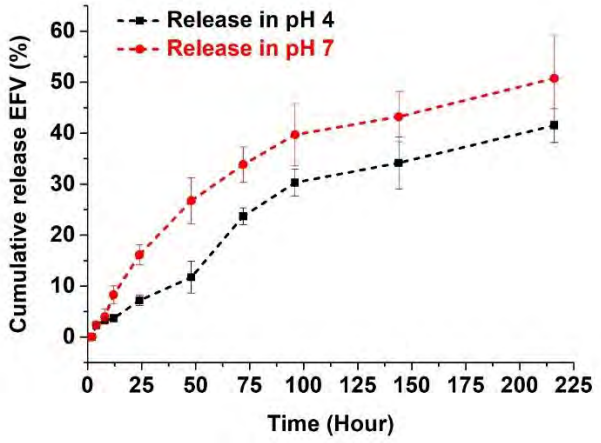

Figure 39. *Cumulative release profiles of efavirenz entrapped in the LNC-CS/iCar-p(AAm-co-AA) hydrogel composite, both in pH 7 and 4.*

3.2.9. Conclusion

The objective of this project was to fabricate a composite of lipid nanocapsules and hydrogel for potential prolonged release of antiviral drugs, with efavirenz used as the drug model. Two polysaccharides were selected to synthesize the hydrogel scaffold. Chitosan was chosen given its wide and successful use in the field of drug delivery, while iota-carrageenan was selected as it has been reported to be effective against sars-cov-2 virus, the overall selection having the potential benefit of yielding a hydrogel with promising anti-viral activity. Experiments were designed by using the design expert software version 13, which was able to construct linear and reduced quadratic models with the ability of predicting the hydrogel swelling ratio and its

encapsulation capacity, respectively. The hydrogel was synthesized by free radical co-polymerization that resulted in a chitosan-g-iota carrageenan-g-poly (acrylamide-co-acrylic acid) hydrogel (CS/iCar-p(AAm-co-AA)). This one exhibited a swelling ratio of about 30,000% (300 g of water for 1 g of hydrogel). The LNC-CS/iCar-p(AAm-co-AA) hydrogel composite was obtained by allowing the hydrogel to swell in a solution of LNC, followed by determination of encapsulation efficiency of efavirenz entrapped in the LNC core, which turned out to be about 53%. Different characterization techniques were used to assess the properties of the developed materials and further supported successful modification of the polysaccharides as well as successful manufacturing of EFV-LNC- CS/iCar-p(AAm-co-AA) hydrogel composite. The SEM particularly confirmed the porous nature of the developed hydrogels. Finally, the release study unveiled prolonged release profiles of efavirenz of about 50 and 40% in pHs 7 and 4, respectively.

Chapter Four

General Conclusion

4. GENERAL CONCLUSION

In conclusion, this research mainly aimed to design, synthesize, manufacture, characterize and evaluate lipid nanocapsules-hydrogel composite (LNC-hydrogel composite) as being a potential anti-covid-19 drug delivery system. The topic was divided into two projects, one focused on LNC and the other focused on hydrogel and LNC-hydrogel composite. Efavirenz, a very poor water-soluble compound, was used as the antiviral model drug. The work reports successful construction of polynomial models capable of predicting both LNC and hydrogel properties, namely the droplet size (DS), the polydispersity index (PDI), the Zeta potential (ZP), and the swelling capacity. Prediction models for encapsulation efficiency and drug loading capacity are also reported.

Natural raw materials such as medium-chain triglycerides oil from coconut and palm kernel oil and crude soya lecithin turned out to be successful in the production of stable LNC. The preparation technique used to produce LNC consisted of a low energy method named phase inversion, which allowed obtaining LNC with droplet size less than 100 nm measured using the dynamic light scattering (DLS). Different characterization techniques such as XRD, DSC, FTIR, EDS and TEM were used to study the LNC chemical composition, phase behaviour along with their morphological properties. After conclusive encapsulation of EFV in LNC lipid liquid core, release experiments were carried out in 1% sodium lauryl sulfate solution (SLS) adjusted to pH 4 then pH7, and revealed prolonged release profiles, with the alkaline medium achieving higher drug release than the acidic one. When stored at room temperature (15 ± 0.8) over a period of 28 days, EFV-LNC remained relatively stable with no significant change observed in their properties (DS, PDI and ZP).

Furthermore, successful hydrogel synthesis by free radical copolymerization was reported. Chitosan and iota-carrageenan, two polysaccharides with incredible biological activities, were used as polymer backbones to which acrylamide (AAm) and acrylic acid (AA) monomers were grafted using N'N'-methylene bisacrylamide (MBA) as crosslinking agent, yielding the chitosan-g-iota carrageenan-g-poly (acrylamide-co-acrylic acid) hydrogel (CS/iCar-p(AAm-co-AA)). The swelling capacity of this hydrogel turned out to be influenced by changes in the starting materials amounts, with higher rates observed for high proportions of iota-carrageenan and low proportions of chitosan, AAm, AA and MBA. The hydrogel synthesis was followed by the preparation of EFV-LNC- CS/iCar-p(AAm-co-AA) hydrogel composite. This one was

realised by allowing the hydrogel to swell in a solution of EFV-LNC resulting in their entrapment. Afterwards, encapsulation efficiency was determined by quantifying the amount of EFV encapsulated in the core of LNC, themselves entrapped in the hydrogel scaffold. Characterization techniques like FTIR, TGA, XRD, EDS and SEM allowed screening out the chemical composition of hydrogel and EFV-LNC-hydrogel, their decomposition profile, their phase behaviour as well as their surface properties. Finally, the release studies performed in 1% SLS solution (pHs 4 and 7), unveiled prolonged release profiles over 9 days. Therefore, LNC-CS/iCar-p(AAm-co-AA) hydrogel composite could be used to not only improve the solubility of poorly water-soluble compounds, but also to limit multi-dose drug administration. This has the advantage of keeping the organism exposed to the therapeutic dose needed to fight the infection, but also limits regular contact with the patient and thus reduces the spread of the disease as in the case of covid-19.

Future perspective

Although interesting results have been reported in this work, much remains to be done to bring this technology to the healthcare system through its translation into the clinic. Up to now, some further studies are underway, including:

— Microscopic investigation of the internal structure of the EFV-LNC-CS/iCar-p(AAm-co-AA) hydrogel composite to observe the presence LNC in the hydrogel scaffold, by using Transmission Electron Microscopy (TEM). Figure 40 illustrates some preliminary images obtained so far at different magnifications;
— Cytotoxicity studies of both EFV-LNC and EFV-LNC-CS/iCar-p(AAm-co-AA) hydrogel composite to ensure they can be safely use for potential clinical essays;
— Antimicrobial activity evaluation of both EFV-LNC and EFV-LNC- CS/iCar-p(AAm-co-AA) hydrogel composite to verify if the drug's biological activity was maintained, enhanced, reduced or lost after the manufacturing process.

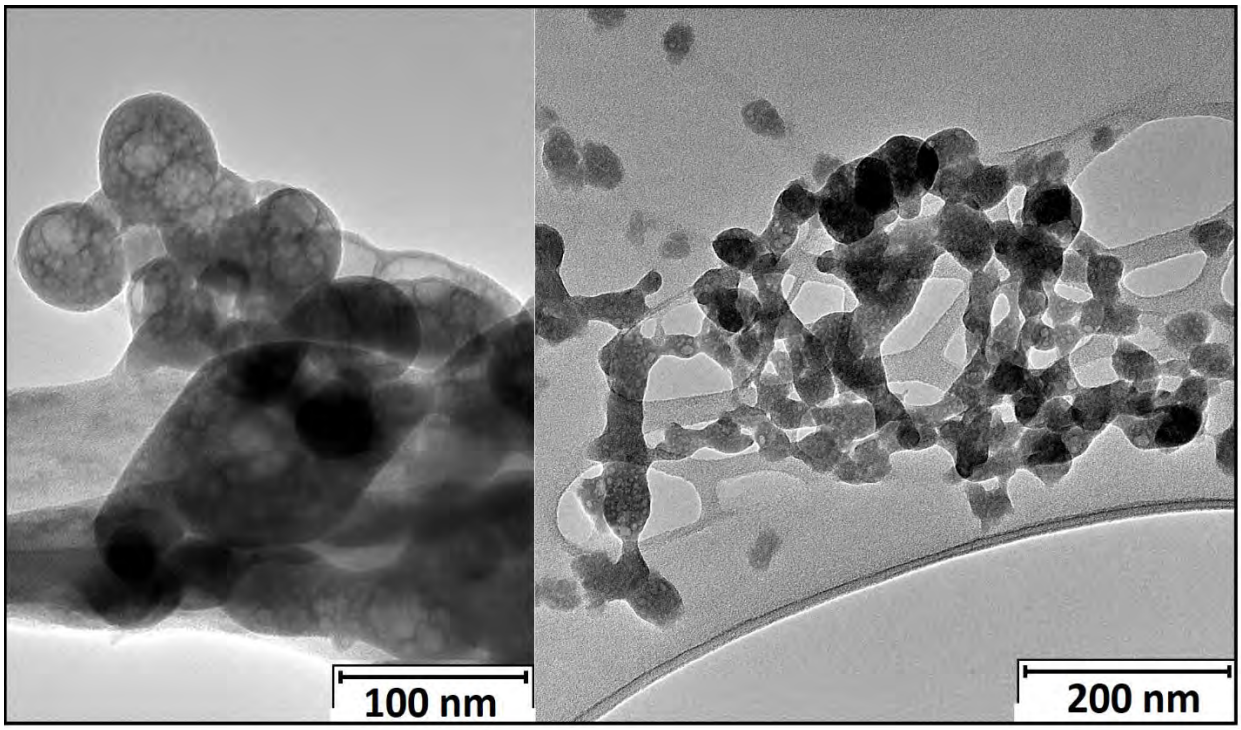

Figure 40. *Preliminary TEM images of EFV-LNC-CS/iCar-p(AAm-co-AA) hydrogel composite*

On the other side, further characterization studies could be performed on the synthesized hydrogel as well as on the LNC-hydrogel composite. They could include:

— Evaluation of their response to stimuli (pH, temperature etc.);

— Evaluation of their mechanical properties (viscosity);
— Evaluation of their ability to apply to other drugs than EFV (encapsulation efficiency, drug loading capacity, drug release profile);
— *In vivo* pharmacological properties evaluation;
— Formulation and evaluation of a nasal spray based on the developed LNC-hydrogel composite;
— Etc.

References

1. Singhal, T. Review on COVID19 Disease so Far. *The Indian Journal of Pediatrics* **2020**, *87*, 281–286.

2. Madabhavi, I.; Sarkar, M.; Kadakol, N. CoviD-19: A Review. *Monaldi Archives for Chest Disease* **2020**, *90*, 248–258, doi:10.4081/monaldi.2020.1298.

3. Huang, C.; Wang, Y.; Li, X.; Ren, L.; Zhao, J.; Hu, Y.; Zhang, L.; Fan, G.; Xu, J.; Gu, X.; et al. Clinical Features of Patients Infected with 2019 Novel Coronavirus in Wuhan, China. *The Lancet* **2020**, *395*, 497–506, doi:10.1016/S0140-6736(20)30183-5/ATTACHMENT/D5332CA1-83D8-4C4C-BC57-00A390BF0396/MMC1.PDF.

4. WHO Coronavirus Disease (COVID-19) Situation Reports Available online: https://www.who.int/emergencies/diseases/novel-coronavirus-2019/situation-reports (accessed on 23 April 2022).

5. WHO Weekly Epidemiological Update on COVID-19 - 20 April 2022 Available online: https://www.who.int/publications/m/item/weekly-epidemiological-update-on-covid-19---20-april-2022 (accessed on 22 April 2022).

6. Kamiya, Y.; Lai, N.M.S.; Schmid, K. *World Population Ageing*; 2020; ISBN 9789211483475.

7. Adams, J.; MacKenzie, M.J.; Amegah, A.K.; Ezeh, A.; Gadanya, M.A.; Omigbodun, A.; Sarki, A.M.; Thistle, P.; Ziraba, A.K.; Stranges, S.; et al. The Conundrum of Low COVID-19 Mortality Burden in Sub-Saharan Africa: Myth or Reality? *Glob Health Sci Pract* **2021**, *9*, 433–443, doi:10.9745/GHSP-D-21-00172.

8. Lawal, Y. Africa's Low COVID-19 Mortality Rate: A Paradox? *International Journal of Infectious Diseases* **2021**, *102*, 118–122, doi:10.1016/J.IJID.2020.10.038.

9. United Nations *World Population Ageing 2015*; 2015;

10. Chitungo, I.; Dzobo, M.; Hlongwa, M.; Dzinamarira, T. COVID-19: Unpacking the Low Number of Cases in Africa. *Public Health in Practice* **2020**, *1*, 100038, doi:10.1016/J.PUHIP.2020.100038.

11. Lone, S.A.; Ahmad, A. COVID-19 Pandemic – an African Perspective. *https://doi.org/10.1080/22221751.2020.1775132* **2020**, *9*, 1300–1308, doi:10.1080/22221751.2020.1775132.

12. Osei, S.A.; Biney, R.P.; Anning, A.S.; Nortey, L.N.; Ghartey-Kwansah, G. Low Incidence of COVID-19 Case Severity and Mortality in Africa; Could Malaria Co-Infection Provide the Missing Link? *BMC Infect Dis* **2022**, *22*, 1–11, doi:10.1186/S12879-022-07064-4/FIGURES/2.

13. Ghosh, D.; Jonathan, A.; Mersha, T.B. COVID-19 Pandemic: The African Paradox. *J Glob Health* **2020**, *10*, 1–6, doi:10.7189/JOGH.10.020348.

14. WHO Weekly Bulletins on Outbreaks and Other Emergencies | WHO | Regional Office for Africa Available online: https://www.afro.who.int/health-topics/disease-outbreaks/outbreaks-and-other-emergencies-updates (accessed on 23 April 2022).

15. Stiegler, N.; Bouchard, J.P. South Africa: Challenges and Successes of the COVID-19 Lockdown. *Annales Médico-psychologiques, revue psychiatrique* **2020**, *178*, 695–698, doi:10.1016/J.AMP.2020.05.006.

16. Broadbent, A.; Combrink, H.; Smart, B. COVID-19 in South Africa. *Glob Epidemiol* **2020**, *2*, 100034, doi:10.1016/J.GLOEPI.2020.100034.

17. Wang, M.Y.; Zhao, R.; Gao, L.J.; Gao, X.F.; Wang, D.P.; Cao, J.M. SARS-CoV-2: Structure, Biology, and Structure-Based Therapeutics Development. *Front Cell Infect Microbiol* **2020**, *10*, 724, doi:10.3389/FCIMB.2020.587269/BIBTEX.

18. Hasöksüz, M.; Kiliç, S.; Saraç, F. Coronaviruses and Sars-Cov-2. *Turk J Med Sci* **2020**, *50*, 549–556, doi:10.3906/SAG-2004-127.

19. Michel, C.J.; Mayer, C.; Poch, O.; Thompson, J.D. Characterization of Accessory Genes in Coronavirus Genomes. *Virol J* **2020**, *17*, 1–13, doi:10.1186/S12985-020-01402-1/FIGURES/8.

20. Salgado, S.; Maiso, A.; Gonzáles, T. Epidemiología y Fisiopatología de La COVID-19. *Patología Respiratoria* **2020**, *23*, 246–250.

21. Zeng, W.; Liu, G.; Ma, H.; Zhao, D.; Yang, Y.; Liu, M.; Mohammed, A.; Zhao, C.; Yang, Y.; Xie, J.; et al. Biochemical Characterization of SARS-CoV-2 Nucleocapsid Protein. *Biochem Biophys Res Commun* **2020**, *527*, 618–623, doi:10.1016/j.bbrc.2020.04.136.

22. Ahmed, S.F.; Quadeer, A.A.; McKay, M.R. Preliminary Identification of Potential Vaccine Targets for the COVID-19 Coronavirus (SARS-CoV-2) Based on SARS-CoV Immunological Studies. *Viruses* **2020**, *12*, doi:10.3390/v12030254.

23. Shang, J.; Wan, Y.; Luo, C.; Ye, G.; Geng, Q.; Auerbach, A.; Li, F. Cell Entry Mechanisms of SARS-CoV-2. *Proc Natl Acad Sci U S A* **2020**, *117*, 1–8, doi:10.1073/pnas.2003138117.

24. Li, R.; Qin, C. Expression Pattern and Function of SARS-CoV-2 Receptor ACE2. *Biosaf Health* **2021**, *3*, 312–318, doi:10.1016/j.bsheal.2021.08.003.

25. Li, M.; Li, L.; Zhang, Y.; Wang, X. An Investigation of the Expression of 2019 Novel Coronavirus Cell Receptor Gene ACE2 in a Wide Variety of Human Tissues. *Infect Dis Poverty* **2020**, *9(1)*, 1–7.

26. Ruch, T.R.; Machamer, C.E. The Coronavirus E Protein: Assembly and Beyond. *Viruses* **2012**, *4*, 363, doi:10.3390/V4030363.

27. Florindo, H.F.; Kleiner, R.; Vaskovich-Koubi, D.; Acúrcio, R.C.; Carreira, B.; Yeini, E.; Tiram, G.; Liubomirski, Y.; Satchi-Fainaro, R. Immune-Mediated Approaches against COVID-19. *Nature Nanotechnology 2020 15:8* **2020**, *15*, 630–645, doi:10.1038/s41565-020-0732-3.

28. Vasireddy, D.; Vanaparthy, R.; Mohan, G.; Malayala, S.V.; Atluri, P. Review of COVID-19 Variants and COVID-19 Vaccine Efficacy: What the Clinician Should Know? *J Clin Med Res* **2021**, *13*, 317–325, doi:10.14740/jocmr4518.

29. Parums, D. v. Editorial: Revised World Health Organization (Who) Terminology for Variants of Concern and Variants of Interest of Sars-Cov-2. *Medical Science Monitor* 2021, *27*.

30. Hadj Hassine, I. Covid-19 Vaccines and Variants of Concern: A Review. *Rev Med Virol* 2022, *32*.

31. Lu, R.; Zhao, X.; Li, J.; Niu, P.; Yang, B.; Wu, H.; Wang, W.; Song, H.; Huang, B.; Zhu, N.; et al. Genomic Characterisation and Epidemiology of 2019 Novel Coronavirus: Implications for Virus Origins and Receptor Binding. *The Lancet* **2020**, *395*, 565–574, doi:10.1016/S0140-6736(20)30251-8.

32. Murgolo, N.; Therien, A.G.; Howell, B.; Klein, D.; Koeplinger, K.; Lieberman, L.A.; Adam, G.C.; Flynn, J.; McKenna, P.; Swaminathan, G.; et al. SARS-CoV-2 Tropism, Entry, Replication, and Propagation: Considerations for Drug Discovery and Development. *PLoS Pathog* **2021**, *17*, 1–18, doi:10.1371/JOURNAL.PPAT.1009225.

33. Mason, R.J. Pathogenesis of COVID-19 from a Cell Biology Perspective. *European Respiratory Journal* **2020**, *55*, 9–11, doi:10.1183/13993003.00607-2020.

34. Liu, Y.C.; Kuo, R.L.; Shih, S.R. COVID-19: The First Documented Coronavirus Pandemic in History. *Biomed J* **2020**, *43*, 328–333, doi:10.1016/J.BJ.2020.04.007.

35. Kumar, R.; Nagpal, S.; Kaushik, S.; Mendiratta, S. COVID-19 Diagnostic Approaches: Different Roads to the Same Destination. *Virusdisease* 2020, *31*, 97–105.

36. Kyosei, Y.; Yamura, S.; Namba, M.; Yoshimura, T.; Watabe, S.; Ito, E. Antigen Tests for COVID-19. *Biophys Physicobiol* 2021, *18*, 28–39.

37. Kopel, J.; Goyal, H.; Perisetti, A. Antibody Tests for COVID-19. *Baylor University Medical Center Proceedings* 2021, *34*, 63–72.

38. Liu, G.; Rusling, J.F. COVID-19 Antibody Tests and Their Limitations. *ACS Sens* 2021, *6*, 593–612.

39. Teymouri, M.; Mollazadeh, S.; Mortazavi, H.; Naderi Ghale-noie, Z.; Keyvani, V.; Aghababaei, F.; Hamblin, M.R.; Abbaszadeh-Goudarzi, G.; Pourghadamyari, H.; Hashemian, S.M.R.; et al. Recent Advances and Challenges of RT-PCR Tests for the Diagnosis of COVID-19. *Pathol Res Pract* 2021, *221*.

40. Burckhardt, R.M.; Dennehy, J.J.; Poon, L.L.M.; Saif, L.J.; Enquist, L.W. Are COVID-19 Vaccine Boosters Needed? The Science behind Boosters. *J Virol* **2022**, *96*, doi:10.1128/jvi.01973-21.

41. Pascarella, G.; Strumia, A.; Piliego, C.; Bruno, F.; Del Buono, R.; Costa, F.; Scarlata, S.; Agrò, F.E. COVID-19 Diagnosis and Management: A Comprehensive Review. *J Intern Med* **2020**, *288*, 192–206, doi:10.1111/joim.13091.

42. Satarker, S.; Ahuja, T.; Banerjee, M.; E, V.B.; Dogra, S.; Agarwal, T.; Nampoothiri, M. Hydroxychloroquine in COVID-19: Potential Mechanism of Action Against SARS-CoV-2. *Curr Pharmacol Rep* **2020**, *6*, 203, doi:10.1007/S40495-020-00231-8.

43. Cao, B.; Wang, Y.; Wen, D.; Liu, W.; Wang, J.; Fan, G.; Ruan, L.; Song, B.; Cai, Y.; Wei, M.; et al. A Trial of Lopinavir–Ritonavir in Adults Hospitalized with Severe Covid-19. *New England Journal of Medicine* **2020**, *382*, 1787–1799, doi:10.1056/NEJMOA2001282/SUPPL_FILE/NEJMOA2001282_DATA-SHARING.PDF.

44. Rubin, D.; Chan-Tack, K.; Farley, J.; Sherwat, A. FDA Approval of Remdesivir — A Step in the Right Direction. *New England Journal of Medicine* **2020**, *383*, 2598–2600, doi:10.1056/NEJMP2032369/SUPPL_FILE/NEJMP2032369_DISCLOSURES.PDF.

45. Wang, M.; Cao, R.; Zhang, L.; Yang, X.; Liu, J.; Xu, M.; Shi, Z.; Hu, Z.; Zhong, W.; Xiao, G. Remdesivir and Chloroquine Effectively Inhibit the Recently Emerged Novel Coronavirus (2019-NCoV) in Vitro. *Cell Research 2020 30:3* **2020**, *30*, 269–271, doi:10.1038/s41422-020-0282-0.

46. Yin, W.; Mao, C.; Luan, X.; Shen, D.D.; Shen, Q.; Su, H.; Wang, X.; Zhou, F.; Zhao, W.; Gao, M.; et al. Structural Basis for Inhibition of the RNA-Dependent RNA Polymerase from SARS-CoV-2 by Remdesivir. *Science* **2020**, *368*, 1499–1504, doi:10.1126/SCIENCE.ABC1560.

47. Shen, C.; Wang, Z.; Zhao, F.; Yang, Y.; Li, J.; Yuan, J.; Wang, F.; Li, D.; Yang, M.; Xing, L.; et al. Treatment of 5 Critically Ill Patients With COVID-19 With Convalescent Plasma. *JAMA* **2020**, *323*, 1582–1589, doi:10.1001/JAMA.2020.4783.

48. Gupta, A.; Gonzalez-Rojas, Y.; Juarez, E.; Crespo Casal, M.; Moya, J.; Falci, D.R.; Sarkis, E.; Solis, J.; Zheng, H.; Scott, N.; et al. Early Treatment for Covid-19 with SARS-CoV-2 Neutralizing Antibody Sotrovimab. *New England Journal of Medicine* **2021**, *385*, 1941–1950, doi:10.1056/NEJMOA2107934/SUPPL_FILE/NEJMOA2107934_DATA-SHARING.PDF.

49. Ong, S.W.X.; Ren, D.; Lee, P.H.; Sutjipto, S.; Dugan, C.; Khoo, B.Y.; Tay, J.X.; Vasoo, S.; Young, B.E.; Lye, D.C. Real-World Use of Sotrovimab for Pre-Emptive Treatment in High-Risk Hospitalized COVID-19 Patients: An Observational Cross-Sectional Study. *Antibiotics 2022, Vol. 11, Page 345* **2022**, *11*, 345, doi:10.3390/ANTIBIOTICS11030345.

50. Su, H.; Xu, Y.; Jiang, H. Drug Discovery and Development Targeting the Life Cycle of SARS-CoV-2. *Fundamental Research* **2021**, *1*, 151–165, doi:10.1016/J.FMRE.2021.01.013.

51. Radesca, L.A.; Lo, Y.S.; Moore, J.R.; Pierce, M.E. Synthesis of HIV-1 Reverse Transcriptase Inhibitor DMP 266. *https://doi.org/10.1080/00397919708005064* **2006**, *27*, 4373–4384, doi:10.1080/00397919708005064.

52. Christofoletti, R.; Nair, A.; Abrahamsson, B.; Groot, D.W.; Kopp, S.; Langguth, P.; Polli, J.E.; Shah, V.P.; Dressman, J.B. Biowaiver Monographs for Immediate Release Solid Oral Dosage Forms: Efavirenz. *J Pharm Sci* **2013**, *102*, 318–329, doi:10.1002/jps.23380.

53. Gatch, M.B.; Kozlenkov, A.; Huang, R.Q.; Yang, W.; Nguyen, J.D.; González-Maeso, J.; Rice, K.C.; France, C.P.; Dillon, G.H.; Forster, M.J.; et al. The HIV Antiretroviral Drug Efavirenz Has LSD-Like Properties. *Neuropsychopharmacology 2013 38:12* **2013**, *38*, 2373–2384, doi:10.1038/npp.2013.135.

54. Adkins, J.C.; Noble, S. Efavirenz. *Drugs 1998 56:6* **2012**, *56*, 1055–1064, doi:10.2165/00003495-199856060-00014.

55. Yee, J.; Preuss, C. V *Efavirenz*; StatPearls Publishing, Treasure Island (FL), 2021;

56. Kappelhoff, B.S.; Huitema, A.D.R.; Yalvaç, Z.; Prins, J.M.; Mulder, J.W.; Meenhorst, P.L.; Beijnen, J.H. Population Pharmacokinetics of Efavirenz in an Unselected Cohort of HIV-1-Infected Individuals. *Clin Pharmacokinet* **2005**, *44*, 849–861, doi:10.2165/00003088-200544080-00006/FIGURES/5.

57. Dooley, K.E.; Denti, P.; Martinson, N.; Cohn, S.; Mashabela, F.; Hoffmann, J.; Haas, D.W.; Hull, J.; Msandiwa, R.; Castel, S.; et al. Pharmacokinetics of Efavirenz and Treatment of HIV-1 Among Pregnant Women With and Without Tuberculosis Coinfection. *J Infect Dis* **2015**, *211*, 197–205, doi:10.1093/INFDIS/JIU429.

58. Bumpus, N.N.; Kent, U.M.; Hollenberg, P.F. Metabolism of Efavirenz and 8-Hydroxyefavirenz by P450 2B6 Leads to Inactivation by Two Distinct Mechanisms. *Journal of Pharmacology and Experimental Therapeutics* **2006**, *318*, 345–351, doi:10.1124/JPET.106.102525.

59. McDonagh, E.M.; Lau, J.L.; Alvarellos, M.L.; Altman, R.B.; Klein, T.E. PharmGKB Summary: Efavirenz Pathway, Pharmacokinetics (PK). *Pharmacogenet Genomics* **2015**, *25*, 363, doi:10.1097/FPC.0000000000000145.

60. Ogburn, E.T.; Jones, D.R.; Masters, A.R.; Xu, C.; Guo, Y.; Desta, Z. Efavirenz Primary and Secondary Metabolism In Vitro and In Vivo: Identification of Novel Metabolic Pathways and Cytochrome P450 2A6 as the Principal Catalyst of Efavirenz 7-Hydroxylation. *Drug Metabolism and Disposition* **2010**, *38*, 1218, doi:10.1124/DMD.109.031393.

61. Cressey, T.R.; Stek, A.; Capparelli, E.; Bowonwatanuwong, C.; Prommas, S.; Sirivatanapa, P.; Yuthavisuthi, P.; Neungton, C.; Huo, Y.; Smith, E.; et al. Efavirenz Pharmacokinetics during the Third Trimester of Pregnancy and Postpartum. *J Acquir Immune Defic Syndr* **2012**, *59*, 245, doi:10.1097/QAI.0B013E31823FF052.

62. Jordaan, M.A.; Ebenezer, O.; Damoyi, N.; Shapi, M. Virtual Screening, Molecular Docking Studies and DFT Calculations of FDA Approved Compounds Similar to the Non-Nucleoside Reverse Transcriptase Inhibitor (NNRTI) Efavirenz. *Heliyon* **2020**, *6*, e04642, doi:10.1016/j.heliyon.2020.e04642.

63. Frediansyah, A.; Tiwari, R.; Sharun, K.; Dhama, K.; Harapan, H. Antivirals for COVID-19: A Critical Review. *Clin Epidemiol Glob Health* **2021**, *9*, 90–98, doi:10.1016/J.CEGH.2020.07.006.

64. Mohamed, K.; Yazdanpanah, N.; Saghazadeh, A.; Rezaei, N. Computational Drug Discovery and Repurposing for the Treatment of COVID-19: A Systematic Review. *Bioorg Chem* 2021, *106*.

65. Beck, B.R.; Shin, B.; Choi, Y.; Park, S.; Kang, K. Predicting Commercially Available Antiviral Drugs That May Act on the Novel Coronavirus (SARS-CoV-2) through a Drug-Target Interaction Deep Learning Model. *Comput Struct Biotechnol J* **2020**, *18*, 784–790, doi:10.1016/j.csbj.2020.03.025.

66. Huynh, N.; Passirani, C.; Saulnier, P.; Benoit, J. Lipid Nanocapsules: A New Platform for Nanomedicine. *Int J Pharm* **2009**, *379*, 201–209, doi:10.1016/J.IJPHARM.2009.04.026.

67. Heurtault, B., Saulnier, P., Proust, J.E., Benoit, J.P. Lipid Nanocapsules, Preparation Process and Use as Medicine. **2000**, *2*.

68. Rassouli, A.; Al-qushawi, A. Lipid-Based Nanoparticles as Novel Drug Delivery Systems for Antimicrobial Agents. *Iran J Vet Sci Technol* **2018**, 1–16, doi:10.22067/veterinary.v2i10.75569.

69. Heurtault, B.; Saulnier, P.; Pech, B.; Proust, J.E.; Benoit, J.P. A Novel Phase Inversion-Based Process for the Preparation of Lipid Nanocarriers. *Pharm Res* **2002**, *19*, 875–880, doi:10.1023/A:1016121319668.

70. Kumar, M.; Bishnoi, R.S.; Shukla, A.K.; Jain, C.P. Techniques for Formulation of Nanoemulsion Drug Delivery System: A Review. *Prev Nutr Food Sci* **2019**, *24*, 225–234, doi:10.3746/pnf.2019.24.3.225.

71. Shinoda, K.; Saito, H. The Effect of Temperature on the Phase Equilibria and the Types of Dispersions of the Ternary System Composed of Water, Cyclohexane, and Nonionic Surfactant. *J Colloid Interface Sci* **1968**, *26*, 70–74, doi:10.1016/0021-9797(68)90273-7.

72. Moreira de Morais, J.; Henrique dos Santos, D.O.; Delicato, T.; Azzini Gonçalves, R.; Alves da Rocha-Filho, P. Physicochemical Characterization of Canola Oil/Water Nano-Emulsions Obtained by Determination of Required HLB Number and Emulsion Phase Inversion Methods. *J Dispers Sci Technol* **2006**, *27*, 109–115, doi:10.1081/DIS-200066829.

73. Solans, C.; Solé, I. Nano-Emulsions: Formation by Low-Energy Methods. *Curr Opin Colloid Interface Sci* **2012**, *17*, 246–254, doi:10.1016/J.COCIS.2012.07.003.

74. Rawal, S.U.; Patel, M.M. *Lipid Nanoparticulate Systems: Modern Versatile Drug Carriers*; Elsevier Inc., 2018; ISBN 9780128136874.

75. Anton, N.; Gayet, P.; Benoit, J.P.; Saulnier, P. Nano-Emulsions and Nanocapsules by the PIT Method: An Investigation on the Role of the Temperature Cycling on the Emulsion Phase Inversion. *Int J Pharm* **2007**, *344*, 44–52, doi:10.1016/j.ijpharm.2007.04.027.

76. Förster, T.; Von Rybinski, W.; Wadle, A. Influence of Microemulsion Phases on the Preparation of Fine-Disperse Emulsions. *Adv Colloid Interface Sci* **1995**, *58*, 119–149, doi:10.1016/0001-8686(95)00247-N.

77. Pons, R.; Carrera, I.; Caelles, J.; Rouch, J.; Panizza, P. Formation and Properties of Mini-Emulsions Formed by Microemulsions Dilution. *Adv Colloid Interface Sci* **2003**, *106*, 129–146, doi:10.1016/S0001-8686(03)00108-8.

78. Saberi, A.H.; Fang, Y.; McClements, D.J. Formation of Thermally Reversible Optically Transparent Emulsion-Based Delivery Systems Using Spontaneous Emulsification. *Soft Matter* **2015**, *11*, 9321–9329, doi:10.1039/c5sm02221e.

79. Lorant, R.; Bara, I.; Josso, M.; Vernaire, S. Patent. Transparent or Transluscent Emulsions, Process for Preparing Them and Cosmetic Use Thereof.Pdf 2003.

80. Izquierdo, P.; Esquena, J.; Tadros, T.F.; Dederen, C.; Garcia, M.J.; Azemar, N.; Solans, C. Formation and Stability of Nano-Emulsions Prepared Using the Phase Inversion Temperature Method. *Langmuir* **2001**, *18*, 26–30, doi:10.1021/LA010808C.

81. Izquierdo, P.; Esquena, J.; Tadros, T.F.; Dederen, J.C.; Feng, J.; Garcia-Celma, M.J.; Azemar, N.; Solans, C. Phase Behavior and Nano-Emulsion Formation by the Phase Inversion Temperature Method. *Langmuir* **2004**, *20*, 6594–6598, doi:10.1021/LA049566H/ASSET/IMAGES/MEDIUM/LA049566HN00001.GIF.

82. McClements, D.J. Nanoemulsions versus Microemulsions: Terminology, Differences, and Similarities. *Soft Matter* **2012**, *8*, 1719–1729, doi:10.1039/c2sm06903b.

83. Saulnier, P.; Benoît, J.P. Lipidic Core Nanocapsules as New Drug Delivery Systems. *Nanoparticulates as Drug Carriers* **2006**, 213–224, doi:10.1142/9781860949074_0010.

84. Balamurugan, K. Lipid Nano Particulate Drug Delivery: An Overview of the Emerging Trend. *Pharma Innov* **2018**, *7*, 779–789.

85. Eissa, M.M.; El-Moslemany, R.M.; Ramadan, A.A.; Amer, E.I.; El-Azzouni, M.Z.; El-Khordagui, L.K. Miltefosine Lipid Nanocapsules for Single Dose Oral Treatment of Schistosomiasis Mansoni: A Preclinical Study. *PLoS One* **2015**, *10*, doi:10.1371/journal.pone.0141788.

86. Karmakar, S. Particle Size Distribution and Zeta Potential Based on Dynamic Light Scattering: Techniques to Characterize Stability and Surface Charge Distribution of Charged Colloids. *Recent Trends in Materials: Physics and Chemistry* **2019**, 117–159.

87. Bhattacharjee, S. DLS and Zeta Potential – What They Are and What They Are Not? *Journal of Controlled Release* **2016**, *235*, 337–351, doi:10.1016/J.JCONREL.2016.06.017.

88. Bello, V.; Mattei, G.; Mazzoldi, P.; Vivenza, N.; Gasco, P.; Idee, J.M.; Robic, C.; Borsella, E. Transmission Electron Microscopy of Lipid Vesicles for Drug Delivery: Comparison between

Positive and Negative Staining. *Microscopy and Microanalysis* **2010**, *16*, 456–461, doi:10.1017/S1431927610093645.

89. Bunjes, H.; Unruh, T. Characterization of Lipid Nanoparticles by Differential Scanning Calorimetry, X-Ray and Neutron Scattering. *Adv Drug Deliv Rev* **2007**, *59*, 379–402, doi:10.1016/J.ADDR.2007.04.013.

90. Giron, D. Applications of Thermal Analysis and Coupled Techniques in Pharmaceutical Industry. *Journal of Thermal Analysis and Calorimetry 2002 68:2* **2002**, *68*, 335–357, doi:10.1023/A:1016015113795.

91. Ohline, S.M.; Campbell, M.L.; Turnbull, M.T.; Kohler, S.J. Differential Scanning Calorimetric Study of Bilayer Membrane Phase Transitions. A Biophysical Chemistry Experiment. *J Chem Educ* **2001**, *78*, 1251–1256, doi:10.1021/ED078P1251.

92. Tomoda, B.T.; Yassue-Cordeiro, P.H.; Ernesto, J.V.; Lopes, P.S.; Péres, L.O.; da Silva, C.F.; de Moraes, M.A. Characterization of Biopolymer Membranes and Films: Physicochemical, Mechanical, Barrier, and Biological Properties. *Biopolymer Membranes and Films* **2020**, 67–95, doi:10.1016/B978-0-12-818134-8.00003-1.

93. Patel, J.P.; Parsania, P.H. *Characterization, Testing, and Reinforcing Materials of Biodegradable Composites*; Elsevier Ltd, 2017; ISBN 9780081009703.

94. Kaliva, M.; Vamvakaki, M. Nanomaterials Characterization. *Polymer Science and Nanotechnology: Fundamentals and Applications* **2020**, 401–433, doi:10.1016/B978-0-12-816806-6.00017-0.

95. Vishwakarma, V.; Uthaman, S. *Environmental Impact of Sustainable Green Concrete*; Elsevier Inc., 2019; ISBN 9780128178553.

96. Rajeswari, A.; Jackcina Stobel Christy, E.; Gopi, S.; Jayaraj, K.; Pius, A. Characterization Studies of Polymer-Based Composites Related to Functionalized Filler-Matrix Interface. *Interfaces in Particle and Fibre Reinforced Composites: Current Perspectives on Polymer, Ceramic, Metal and Extracellular Matrices* **2019**, 219–250, doi:10.1016/B978-0-08-102665-6.00009-1.

97. Hodoroaba, V.D. Energy-Dispersive X-Ray Spectroscopy (EDS). *Characterization of Nanoparticles: Measurement Processes for Nanoparticles* **2020**, 397–417, doi:10.1016/B978-0-12-814182-3.00021-3.

98. Wang, G. The Utilization of Slag in Civil Infrastructure Construction. **2013**, doi:10.1016/B978-0-08-099363-8.00011-X.

99. Kumar, C.G.; Pombala, S.; Poornachandra, Y.; Agarwal, S.V. Synthesis, Characterization, and Applications of Nanobiomaterials for Antimicrobial Therapy. *Nanobiomaterials in Antimicrobial Therapy: Applications of Nanobiomaterials* **2016**, 103–152, doi:10.1016/B978-0-323-42864-4.00004-X.

100. Nasr, M.; Abdel-Hamid, S. Lipid Based Nanocapsules: A Multitude of Biomedical Applications. *Curr Pharm Biotechnol* **2015**, *16*, 322–332, doi:10.2174/1389201016041502181035555.

101. Chauvet, S.; Barras, A.; Boukherroub, R.; Bouron, A. Lipid Nanocapsules Containing the Non-Ionic Surfactant Solutol HS15 Inhibit the Transport of Calcium through Hyperforin-Activated Channels in Neuronal Cells. *Neuropharmacology* **2015**, *99*, 726–734, doi:10.1016/j.neuropharm.2015.08.043.

102. Bastiancich, C.; Vanvarenberg, K.; Ucakar, B.; Pitorre, M.; Bastiat, G.; Lagarce, F.; Préat, V.; Danhier, F. Lauroyl-Gemcitabine-Loaded Lipid Nanocapsule Hydrogel for the Treatment of Glioblastoma. *Journal of Controlled Release* **2016**, *225*, 283–293, doi:10.1016/j.jconrel.2016.01.054.

103. Abdel-Mottaleb, M.M.A.; Neumann, D.; Lamprecht, A. In Vitro Drug Release Mechanism from Lipid Nanocapsules (LNC). *Int J Pharm* **2010**, *390*, 208–213, doi:10.1016/j.ijpharm.2010.02.001.

104. Abdel-Mottaleb, M.M.A.; Neumann, D.; Lamprecht, A. Lipid Nanocapsules for Dermal Application: A Comparative Study of Lipid-Based versus Polymer-Based Nanocarriers. *European Journal of Pharmaceutics and Biopharmaceutics* **2011**, *79*, 36–42, doi:10.1016/j.ejpb.2011.04.009.

105. Montigaud, Y.; Ucakar, B.; Krishnamachary, B.; Bhujwalla, Z.M.; Feron, O.; Préat, V.; Danhier, F.; Gallez, B.; Danhier, P. Optimized Acriflavine-Loaded Lipid Nanocapsules as a Safe and Effective Delivery System to Treat Breast Cancer. *Int J Pharm* **2018**, *551*, 322–328, doi:10.1016/j.ijpharm.2018.09.034.

106. Valsalakumari, R.; Yadava, S.K.; Szwed, M.; Pandya, A.D.; Mælandsmo, G.M.; Torgersen, M.L.; Iversen, T.G.; Skotland, T.; Sandvig, K.; Giri, J. Mechanism of Cellular Uptake and Cytotoxicity of Paclitaxel Loaded Lipid Nanocapsules in Breast Cancer Cells. *Int J Pharm* **2021**, *597*, doi:10.1016/J.IJPHARM.2021.120217.

107. Desfrançois, C.; Auzély, R.; Texier, I. Lipid Nanoparticles and Their Hydrogel Composites for Drug Delivery: A Review. *Pharmaceuticals* **2018**, *11*, doi:10.3390/ph11040118.

108. Ferreira, N.N.; Ferreira, L.M.B.; Cardoso, V.M.O.; Boni, F.I.; Souza, A.L.R.; Gremião, M.P.D. Recent Advances in Smart Hydrogels for Biomedical Applications: From Self-Assembly to Functional Approaches. *Eur Polym J* **2018**, *99*, 117–133, doi:10.1016/J.EURPOLYMJ.2017.12.004.

109. Chirani, N.; Yahia, H.; Gritsch, L.; Motta, F.L.; Chirani, S.; Faré, S. History and Applications of Hydrogels. *JOURNAL OF BIOMEDICAL SCIENCES* **2021**, *04*, 1–23, doi:10.4172/2254-609X.100013.

110. Caló, E.; Khutoryanskiy, V. V. Biomedical Applications of Hydrogels: A Review of Patents and Commercial Products. *Eur Polym J* **2015**, *65*, 252–267, doi:10.1016/J.EURPOLYMJ.2014.11.024.

111. Sievers, J.; Sperlich, K.; Stahnke, T.; Kreiner, C.; Eickner, T.; Martin, H.; Guthoff, R.F.; Schünemann, M.; Bohn, S.; Stachs, O. Determination of Hydrogel Swelling Factors by Two Established and a Novel Non-Contact Continuous Method. *J Appl Polym Sci* **2021**, *138*, 50326, doi:10.1002/APP.50326.

112. Ahmed, E.M. Hydrogel: Preparation, Characterization, and Applications: A Review. *J Adv Res* **2015**, *6*, 105–121, doi:10.1016/J.JARE.2013.07.006.

113. Lin, C.C.; Metters, A.T. Hydrogels in Controlled Release Formulations: Network Design and Mathematical Modeling. *Adv Drug Deliv Rev* **2006**, *58*, 1379–1408, doi:10.1016/J.ADDR.2006.09.004.

114. Varaprasad, K.; Raghavendra, G.M.; Jayaramudu, T.; Yallapu, M.M.; Sadiku, R. A Mini Review on Hydrogels Classification and Recent Developments in Miscellaneous Applications. *Mater Sci Eng C Mater Biol Appl* **2017**, *79*, 958–971, doi:10.1016/J.MSEC.2017.05.096.

115. Catoira, M.C.; Fusaro, L.; Di Francesco, D.; Ramella, M.; Boccafoschi, F. Overview of Natural Hydrogels for Regenerative Medicine Applications. *J Mater Sci Mater Med* **2019**, *30*, 1–10, doi:10.1007/S10856-019-6318-7/TABLES/2.

116. Patel, G.; Dalwadi, C. Recent Patents on Stimuli Responsive Hydrogel Drug Delivery System. *Recent Pat Drug Deliv Formul* **2013**, *7*, 206–215, doi:10.2174/18722113076661311181416 00.

117. Buwalda, S.J.; Vermonden, T.; Hennink, W.E. Hydrogels for Therapeutic Delivery: Current Developments and Future Directions. *Biomacromolecules* **2017**, *18*, 316–330, doi:10.1021/ACS.BIOMAC.6B01604.

118. Ding, X.; Wang, Y. Weak Bond-Based Injectable and Stimuli Responsive Hydrogels for Biomedical Applications. *J Mater Chem B* **2017**, *5*, 887–906, doi:10.1039/C6TB03052A.

119. Kulicke, W.-M.; Nottelmann, H. Structure and Swelling of Some Synthetic, Semisynthetic, and Biopolymer Hydrogels. **1989**, 15–44, doi:10.1021/BA-1989-0223.CH002.

120. Ullah, F.; Othman, M.B.H.; Javed, F.; Ahmad, Z.; Akil, H.M. Classification, Processing and Application of Hydrogels: A Review. *Materials Science and Engineering: C* **2015**, *57*, 414–433, doi:10.1016/J.MSEC.2015.07.053.

121. Mishra, S.; Rani, P.; Sen, G.; Dey, K.P. Preparation, Properties and Application of Hydrogels: A Review. **2018**, 145–173, doi:10.1007/978-981-10-6077-9_6.

122. Vigata, M.; Meinert, C.; Hutmacher, D.W.; Bock, N. Hydrogels as Drug Delivery Systems: A Review of Current Characterization and Evaluation Techniques. *Pharmaceutics 2020, Vol. 12, Page 1188* **2020**, *12*, 1188, doi:10.3390/PHARMACEUTICS12121188.

123. Zhang, K.; Feng, W.; Jin, C. Protocol Efficiently Measuring the Swelling Rate of Hydrogels. *MethodsX* **2020**, *7*, 100779, doi:10.1016/J.MEX.2019.100779.

124. Rahman, Md.S.; Islam, Md.M.; Islam, Md.S.; Zaman, A.; Ahmed, T.; Biswas, S.; Sharmeen, S.; Rashid, T.U.; Rahman, M.M. Morphological Characterization of Hydrogels. **2019**, 819–863, doi:10.1007/978-3-319-77830-3_28.

125. Koch, M.; Włodarczyk-Biegun, M.K. Faithful Scanning Electron Microscopic (SEM) Visualization of 3D Printed Alginate-Based Scaffolds. *bioRxiv* **2020**, 2020.03.18.997668, doi:10.1101/2020.03.18.997668.

126. Mathur, A.M.; Scranton, A.B. Characterization of Hydrogels Using Nuclear Magnetic Resonance Spectroscopy. *Biomaterials* **1996**, *17*, 547–557, doi:10.1016/0142-9612(96)88705-9.

127. Diehl, B. Principles in NMR Spectroscopy. *NMR Spectroscopy in Pharmaceutical Analysis* **2008**, 1–41, doi:10.1016/B978-0-444-53173-5.00001-9.

128. Bank, S. Some Principles of NMR Spectroscopy and Their Novel Application. **1997**, doi:10.1002/(SICI)1099-0534(1997)9:2.

129. Reif, B.; Ashbrook, S.E.; Emsley, L.; Hong, M. Solid-State NMR Spectroscopy. *Nature Reviews Methods Primers 2021 1:1* **2021**, *1*, 1–23, doi:10.1038/s43586-020-00002-1.

130. Bhaskar, K.; Krishna Mohan, C.; Lingam, M.; Jagan Mohan, S.; Venkateswarlu, V.; Madhusudan Rao, Y.; Anbu, J.; Ravichandran, V. Development of SLN and NLC Enriched Hydrogels for Transdermal Delivery of Nitrendipine: In Vitro and In Vivo Characteristics.

http://dx.doi.org/10.1080/03639040802192822 **2009**, *35*, 98–113, doi:10.1080/03639040802192822.

131. Qi, H.; Chen, W.; Huang, C.; Li, L.; Chen, C.; Li, W.; Wu, C. Development of a Poloxamer Analogs/Carbopol-Based in Situ Gelling and Mucoadhesive Ophthalmic Delivery System for Puerarin. *Int J Pharm* **2007**, *337*, 178–187, doi:10.1016/j.ijpharm.2006.12.038.

132. Din, F. ud; Kim, D.W.; Choi, J.Y.; Thapa, R.K.; Mustapha, O.; Kim, D.S.; Oh, Y.K.; Ku, S.K.; Youn, Y.S.; Oh, K.T.; et al. Irinotecan-Loaded Double-Reversible Thermogel with Improved Antitumor Efficacy without Initial Burst Effect and Toxicity for Intramuscular Administration. *Acta Biomater* **2017**, *54*, 239–248, doi:10.1016/J.ACTBIO.2017.03.007.

133. Mano, J.F. Stimuli-Responsive Polymeric Systems for Biomedical Applications. *Adv Eng Mater* **2008**, *10*, 515–527, doi:10.1002/ADEM.200700355.

134. Hao, J.; Wang, X.; Bi, Y.; Teng, Y.; Wang, J.; Li, F.; Li, Q.; Zhang, J.; Guo, F.; Liu, J. Fabrication of a Composite System Combining Solid Lipid Nanoparticles and Thermosensitive Hydrogel for Challenging Ophthalmic Drug Delivery. *Colloids Surf B Biointerfaces* **2014**, *114*, 111–120, doi:10.1016/J.COLSURFB.2013.09.059.

135. Gaudana, R.; Jwala, J.; Boddu, S.H.S.; Mitra, A.K. Recent Perspectives in Ocular Drug Delivery. *Pharm Res* **2009**, *26*, 1197–1216, doi:10.1007/S11095-008-9694-0.

136. Coviello, T.; Matricardi, P.; Marianecci, C.; Alhaique, F. Polysaccharide Hydrogels for Modified Release Formulations. *J Control Release* **2007**, *119*, 5–24, doi:10.1016/J.JCONREL.2007.01.004.

137. Messaoudi, K.; Saulnier, P.; Boesen, K.; Benoit, J.P.; Lagarce, F. Anti-Epidermal Growth Factor Receptor SiRNA Carried by Chitosan-Transacylated Lipid Nanocapsules Increases Sensitivity of Glioblastoma Cells to Temozolomide. *Int J Nanomedicine* **2014**, *9*, 1479–1490, doi:10.2147/IJN.S59134.

138. Patil, J.S.; Sarasija, S. Pulmonary Drug Delivery Strategies: A Concise, Systematic Review. *Lung India* **2012**, *29*, 44, doi:10.4103/0970-2113.92361.

139. Groneberg, D.A.; Witt, C.; Wagner, U.; Chung, K.F.; Fischer, A. Fundamentals of Pulmonary Drug Delivery. *Respir Med* **2003**, *97*, 382–387, doi:10.1053/RMED.2002.1457.

140. Whittemore, S. *Anatomy of the Respiratory System*; Infobase Publishing: New York, 2004; Vol. 32; ISBN 9780791076279.

141. Ward, J.P.T.; Ward, J.; Leach, R.M. *The Respiratory System at a Glance, 3rd Edition*; Wiley-Blackwell, 2010;

142. Möller, W.; Häußinger, K.; Ziegler-Heitbrock, L.; Heyder, J. Mucociliary and Long-Term Particle Clearance in Airways of Patients with Immotile Cilia. *Respir Res* **2006**, *7*, 10, doi:10.1186/1465-9921-7-10.

143. Yeh, H.C.; Phalen, R.F.; Raabe, O.G. Factors Influencing the Deposition of Inhaled Particles. *Environ Health Perspect* **1976**, *15*, 147–156, doi:10.1289/EHP.7615147.

144. Edwards, D.A.; Ben-Jebria, A.; Langer, R. Recent Advances in Pulmonary Drug Delivery Using Large, Porous Inhaled Particles. *J Appl Physiol (1985)* **1998**, *85*, 379–385, doi:10.1152/JAPPL.1998.85.2.379.

145. Lee, S.L.; Adams, W.P.; Li, B. V.; Conner, D.P.; Chowdhury, B.A.; Yu, L.X. In Vitro Considerations to Support Bioequivalence of Locally Acting Drugs in Dry Powder Inhalers for Lung Diseases. *AAPS J* **2009**, *11*, 414–423, doi:10.1208/S12248-009-9121-4.

146. Scheuch, G.; Kohlhaeufl, M.J.; Brand, P.; Siekmeier, R. Clinical Perspectives on Pulmonary Systemic and Macromolecular Delivery. *Adv Drug Deliv Rev* **2006**, *58*, 996–1008, doi:10.1016/J.ADDR.2006.07.009.

147. El-Sherbiny, I.M.; El-Baz, N.M.; Yacoub, M.H. Inhaled Nano- and Microparticles for Drug Delivery. *Glob Cardiol Sci Pract* **2015**, *2015*, doi:10.5339/GCSP.2015.2.

148. Paranjpe, M.; Müller-Goymann, C.C. Nanoparticle-Mediated Pulmonary Drug Delivery: A Review. *Int J Mol Sci* **2014**, *15*, 5852–5873, doi:10.3390/IJMS15045852.

149. Stone, K.C.; Mercer, R.R.; Gehr, P.; Stockstill, B.; Crapo, J.D. Allometric Relationships of Cell Numbers and Size in the Mammalian Lung. *Am J Respir Cell Mol Biol* **1992**, *6*, 235–243, doi:10.1165/AJRCMB/6.2.235.

150. Musante, C.J.; Schroeter, J.D.; Rosati, J.A.; Crowder, T.M.; Hickey, A.J.; Martonen, T.B. Factors Affecting the Deposition of Inhaled Porous Drug Particles. *J Pharm Sci* **2002**, *91*, 1590–1600, doi:10.1002/JPS.10152.

151. Du, J.; Du, P.; Smyth, H.D.C. Hydrogels for Controlled Pulmonary Delivery. *Ther Deliv* **2013**, *4*, 1293–1305, doi:10.4155/tde.13.90.

152. Samimi, S.; Maghsoudnia, N.; Eftekhari, R.B.; Dorkoosh, F. *Lipid-Based Nanoparticles for Drug Delivery Systems*; Elsevier Inc., 2018; ISBN 9780128140321.

153. Arora, S.; Chawla, A.; Pawar, P.; Sharma, P. Novel Drug Delivery Approaches on Antiviral and Antiretroviral Agents. *J Adv Pharm Technol Res* **2012**, *3*, 147–159, doi:10.4103/2231-4040.101007.

154. Lembo, D.; Cavalli, R. Nanoparticulate Delivery Systems for Antiviral Drugs. *Antivir Chem Chemother* **2010**, *21*, 53–70, doi:10.3851/IMP1684.

155. Cojocaru, F.D.; Botezat, D.; Gardikiotis, I.; Uritu, C.M.; Dodi, G.; Trandafir, L.; Rezus, C.; Rezus, E.; Tamba, B.I.; Mihai, C.T. Nanomaterials Designed for Antiviral Drug Delivery Transport across Biological Barriers. *Pharmaceutics* **2020**, *12*, 1–34, doi:10.3390/pharmaceutics12020171.

156. Kalepu, S.; Manthina, M.; Padavala, V. Oral Lipid-Based Drug Delivery Systems – an Overview. *Acta Pharm Sin B* **2013**, *3*, 361–372, doi:10.1016/J.APSB.2013.10.001.

157. APA PubChem Compound Summary for CID 64139, Efavirenz Available online: https://pubchem.ncbi.nlm.nih.gov/compound/Efavirenz (accessed on 24 November 2021).

158. Persson, L.C.; Porter, C.J.H.; Charman, W.N.; Bergström, C.A.S. Computational Prediction of Drug Solubility in Lipid Based Formulation Excipients. *Pharm Res* **2013**, *30*, 3225–3237, doi:10.1007/s11095-013-1083-7.

159. Rane, S.S.; Anderson, B.D. What Determines Drug Solubility in Lipid Vehicles: Is It Predictable? *Adv Drug Deliv Rev* **2008**, *60*, 638–656, doi:10.1016/j.addr.2007.10.015.

160. Bienvenu, E.; Hoffmann, K.J.; Ashton, M.; Kayumba, P.C. A Rapid and Selective HPLC-UV Method for the Quantitation of Efavirenz in Plasma from Patients on Concurrent HIV/AIDS and

Tuberculosis Treatments. *Biomedical Chromatography* **2013**, *27*, 1554–1559, doi:10.1002/bmc.2959.

161. Goos, P.; Jones, B.; Syafitri, U. I-Optimal Mixture Designs Faculty of Applied Economics. **2000**, *32*.

162. Mukubwa, G.K.; Safari, J.B.; Walker, R.B. Design , Manufacturing , Characterization and Evaluation of Lipid Nanocapsules to Enhance the Biopharmaceutical Properties of Efavirenz. **2022**.

163. Rahmani, Z.; Ghaemy, M.; Olad, A. Preparation of Nanogels Based on Kappa-Carrageenan/Chitosan and N-Doped Carbon Dots: Study of Drug Delivery Behavior. *Polymer Bulletin* 2021, *78*, 2709–2726.

164. Qi, X.; Wei, W.; Li, J.; Zuo, G.; Pan, X.; Su, T.; Zhang, J.; Dong, W. Salecan-Based PH-Sensitive Hydrogels for Insulin Delivery. *Mol Pharm* **2017**, *14*, 431–440, doi:10.1021/ACS.MOLPHARMACEUT.6B00875.

165. Safari, J.B.; Bapolisi, A.M.; Krause, R.W.M. Development of PH-Sensitive Chitosan-g-Poly (Acrylamide-Co-Acrylic Acid) Hydrogel for Controlled Drug Delivery of Tenofovir Disoproxil Fumarate. *Polymers (Basel)* **2021**, *13*, doi:10.3390/polym13203571.

166. Cristofoletti, R.; Nair, A.; Abrahamsson, B.; Groot, D.W.; Kopp, S.; Langguth, P.; Polli, J.E.; Shah, V.P.; Dressman, J.B. Biowaiver Monographs for Immediate Release Solid Oral Dosage Forms: Efavirenz. *J Pharm Sci* **2013**, *102*, 318–329, doi:10.1002/JPS.23380.

167. Brinkmann, J.; Huxoll, F.; Luebbert, C.; Sadowski, G. Solubility of Pharmaceutical Ingredients in Triglycerides. *European Journal of Pharmaceutics and Biopharmaceutics* **2019**, *145*, 113–120, doi:10.1016/j.ejpb.2019.10.012.

168. Mazonde, P.; Khamanga, S.M.M.; Walker, R.B. Design, Optimization, Manufacture and Characterization of Efavirenz-Loaded Flaxseed Oil Nanoemulsions. *Pharmaceutics* **2020**, *12*, 1–22, doi:10.3390/pharmaceutics12090797.

169. Brinkmann, J.; Rest, F.; Luebbert, C.; Sadowski, G. Solubility of Pharmaceutical Ingredients in Natural Edible Oils. *Mol Pharm* **2020**, *17*, 2499–2507, doi:10.1021/acs.molpharmaceut.0c00215.

170. Aydar, A.Y. Utilization of Response Surface Methodology in Optimization of Extraction of Plant Materials. *Statistical Approaches With Emphasis on Design of Experiments Applied to Chemical Processes* **2018**, doi:10.5772/INTECHOPEN.73690.

171. Li, Z.; Lu, D.; Gao, X. Optimization of Mixture Proportions by Statistical Experimental Design Using Response Surface Method - A Review. *Journal of Building Engineering* **2021**, *36*, 102101, doi:10.1016/J.JOBE.2020.102101.

172. Breig, S.J.M.; Luti, K.J.K. Response Surface Methodology: A Review on Its Applications and Challenges in Microbial Cultures. *Mater Today Proc* **2021**, *42*, 2277–2284, doi:10.1016/j.matpr.2020.12.316.

173. Shabbiri, K.; Adnan, A.; Noor, B.; Jamil, S. Optimized Production, Purification and Characterization of Alpha Amylase by Brevibacterium Linens DSM 20158, Using Bio-Statistical Approach. *Ann Microbiol* **2012**, *62*, 523–532, doi:10.1007/S13213-011-0286-6/FIGURES/2.

174. Singh, S.; Singla, Y.; Arora, S. Statistical, Diagnostic and Response Surface Analysis of Nefopam Hydrochloride Nanospheres Using 35 Box-Behnken Design. *Int J Pharm Pharm Sci* **2015**, *7*, 89–101.

175. M. Christopher, A.M.L.S. Principles of Nanoparticle Design for Overcoming Biological. *Physiol Behav* **2016**, *176*, 100–106, doi:10.1038/nbt.3330.Principles.

176. Xiao, K.; Li, Y.; Luo, J.; Lee, J.S.; Xiao, W.; Gonik, A.M.; Agarwal, R.G.; Lam, K.S. The Effect of Surface Charge on in Vivo Biodistribution of PEG-Oligocholic Acid Based Micellar Nanoparticles. *Biomaterials* **2011**, *32*, 3435–3446, doi:10.1016/j.biomaterials.2011.01.021.

177. Gustafson, H.H.; Holt-Casper, D.; Grainger, D.W.; Ghandehari, H. Nanoparticle Uptake: The Phagocyte Problem. *Nano Today* **2015**, *10*, 487–510, doi:10.1016/j.nantod.2015.06.006.

178. Knoll, R.; Schultze, J.L.; Schulte-Schrepping, J. Monocytes and Macrophages in COVID-19. *Front Immunol* **2021**, *12*, 2952, doi:10.3389/FIMMU.2021.720109/BIBTEX.

179. Byrne, A.J.; Mathie, S.A.; Gregory, L.G.; Lloyd, C.M. Pulmonary Macrophages: Key Players in the Innate Defence of the Airways. *Thorax* **2015**, *70*, 1189–1196, doi:10.1136/THORAXJNL-2015-207020.

180. Thakur, R.K.; Villette, C.; Aubry, J.M.; Delaplace, G. Dynamic Emulsification and Catastrophic Phase Inversion of Lecithin-Based Emulsions. *Colloids Surf A Physicochem Eng Asp* **2008**, *315*, 285–293, doi:10.1016/j.colsurfa.2007.08.017.

181. Ashour, A.A.; Ramadan, A.A.; Abdelmonsif, D.A.; El-Kamel, A.H. Enhanced Oral Bioavailability of Tanshinone IIA Using Lipid Nanocapsules: Formulation, in-Vitro Appraisal and Pharmacokinetics. *Int J Pharm* **2020**, *586*, 119598, doi:10.1016/j.ijpharm.2020.119598.

182. Zaini, E.; Rachmaini, F.; Armin, F.; Fitriani, L. Preparation and Characterization of Binary Mixture of Efavirenz and Nicotinamide. *Oriental Journal of Chemistry* **2015**, *31*, 2271–2276, doi:10.13005/OJC/310454.

183. Fitriani, L.; Haqi, A.; Zaini, E. Preparation and Characterization of Solid Dispersion Freeze-Dried Efavirenz – Polyvinylpyrrolidone K-30. *J Adv Pharm Technol Res* **2016**, *7*, 105, doi:10.4103/2231-4040.184592.

184. Chadha, R.; Arora, P.; Saini, A.; Jain, D.S. An Insight into Thermodynamic Relationship between Polymorphic Forms of Efavirenz. *Journal of Pharmacy and Pharmaceutical Sciences* **2012**, *15*, 234–251, doi:10.18433/j3j30z.

185. Liao, H.Y.; Chu, S.Y. Hydrogen Bond Acceptor Capability of Carbonyl π-Electrons—Case Study of the Hydrogen-Bonded Urea Dimer. *New Journal of Chemistry* **2003**, *27*, 421–424, doi:10.1039/B202440N.

186. Koh, P.; Chuah, J.; Talekar, M.; Gorajana, A.; Garg, S. Formulation Development and Dissolution Rate Enhancement of Efavirenz by Solid Dispersion Systems. *Indian J Pharm Sci* **2013**, *75*, 291–301, doi:10.4103/0250-474X.117434.

187. Lavra, Z.M.M.; Pereira de Santana, D.; Ré, M.I. Solubility and Dissolution Performances of Spray-Dried Solid Dispersion of Efavirenz in Soluplus. *Drug Dev Ind Pharm* **2017**, *43*, 42–54, doi:10.1080/03639045.2016.1205598.

188. Reddy, N.P.; Padmavathi, Y.; Mounika, P.; Anjali, A. FTIR Spectroscopy for Estimation of Efavirenz in Raw Material and Tablet Dosage Form. *International Current Pharmaceutical Journal* **2015**, *4*, 390–395, doi:10.3329/icpj.v4i6.23290.

189. Sathigari, S.K.; Radhakrishnan, V.K.; Davis, V.A.; Parsons, D.L.; Babu, R.J. Amorphous-State Characterization of Efavirenz-Polymer Hot-Melt Extrusion Systems for Dissolution Enhancement. *J Pharm Sci* **2012**, *101*, 3456–3464, doi:10.1002/jps.23125.

190. Li, J.; Wang, X.; Zhang, T.; Wang, C.; Huang, Z.; Luo, X.; Deng, Y. A Review on Phospholipids and Their Main Applications in Drug Delivery Systems. *Asian J Pharm Sci* **2015**, *10*, 81–98, doi:10.1016/J.AJPS.2014.09.004.

191. Omari, D.; Akkam, Y.; for, A.S.-A. of the R.S.; 2021, undefined Drug-Excipient Interactions: An Overview on Mechanisms and Effects on Drug Stability and Bioavailability. *Annalsofrscb.Ro* **2021**, *25*, 8402–8429.

192. Matusiak, J.; Grządka, E. Stability of Colloidal Systems - a Review of the Stability Measurements Methods. *Annales Universitatis Mariae Curie-Sklodowska, sectio AA – Chemia* **2017**, *72*, 33, doi:10.17951/AA.2017.72.1.33.

193. Van Der Hoeven, P.C.; Lyklema, J. Electrostatic Stabilization in Non-Aqueous Media. *Adv Colloid Interface Sci* **1992**, *42*, 205–277, doi:10.1016/0001-8686(92)80024-R.

194. Weiner, B.B.; Tscharnuter, W.W.; Fairhurst, D. Zeta Potential: A New Approach. *Canadian Mineral Analysts Meeting* **1993**, 1–12.

195. Clogston, J.D.; Patri, A.K. Zeta Potential Measurement. *Methods Mol Biol* **2011**, *697*, 63–70, doi:10.1007/978-1-60327-198-1_6.

196. Aydar, A.Y. Utilization of Response Surface Methodology in Optimization of Extraction of Plant Materials. In *Statistical Approaches With Emphasis on Design of Experiments Applied to Chemical Processes*; 2018.

197. Bashir, S.; Teo, Y.Y.; Ramesh, S.; Ramesh, K. Physico-Chemical Characterization of PH-Sensitive N-Succinyl Chitosan-g-Poly (Acrylamide-Co-Acrylic Acid) Hydrogels and in Vitro Drug Release Studies. *Polym Degrad Stab* **2017**, *139*, 38–54, doi:10.1016/j.polymdegradstab.2017.03.014.

198. Ghani, N.A.A.; Othaman, R.; Ahmad, A.; Anuar, F.H.; Hassan, N.H. Impact of Purification on Iota Carrageenan as Solid Polymer Electrolyte. *Arabian Journal of Chemistry* **2019**, *12*, 370–376, doi:10.1016/J.ARABJC.2018.06.008.

199. Chitra, R.; Sathya, P.; Selvasekarapandian, S.; Monisha, S.; Moniha, V.; Meyvel, S. Synthesis and Characterization of Iota-Carrageenan Solid Biopolymer Electrolytes for Electrochemical Applications. *Ionics (Kiel)* **2019**, *25*, 2147–2157, doi:10.1007/S11581-018-2687-Z/TABLES/5.

200. Santa Cruz Martins de Queiroz Antonino, R.; Rosa Paschoal Lia Fook, B.; Alexandre de Oliveira Lima, V.; Ícaro de Farias Rached, R.; Paloma Nascimento Lima, E.; José da Silva Lima, R.; Andrés Peniche Covas, C.; Vinícius Lia Fook, M.; Sashiwa, H.; Harding, D.; et al. Marine Drugs Preparation and Characterization of Chitosan Obtained from Shells of Shrimp (Litopenaeus Vannamei Boone)., doi:10.3390/md15050141.

201. Majekodunmi, S.O.; Olorunsola, E.O.; Uzoaganobi, C.C. Comparative Physicochemical Characterization of Chitosan from Shells of Two Bivalved Mollusks from Two Different

Continents. *American Journal of Polymer Science* **2017**, *7*, 15–22, doi:10.5923/j.ajps.20170701.03.

202. Ayu Laksanawati, T.; Novarita Trisanti, P.; Sumarno Synthesis and Characterization of Composite Gels Starch-Graftacrylic Acid/Bentonite (St-g-AA/B) Using N'Nmethylenebisacrylamide (MBA). *IOP Conf Ser Mater Sci Eng* **2019**, *509*, doi:10.1088/1757-899X/509/1/012150.

203. Abdelkader, R.; Mohammed, B. Green Synthesis of Cationic Polyacrylamide Composite Catalyzed by an Ecologically Catalyst Clay Called Maghnite-H+ (Algerian MMT) under Microwave Irradiation. *Bulletin of Chemical Reaction Engineering & Catalysis* **2016**, *11*, 170–175, doi:10.9767/BCREC.11.2.543.170-175.

204. Hoare, T.R.; Kohane, D.S. Hydrogels in Drug Delivery: Progress and Challenges. *Polymer (Guildf)* **2008**, *49*, 1993–2007, doi:10.1016/j.polymer.2008.01.027.

205. Aranaz, I.; Alcántara, A.R.; Civera, M.C.; Arias, C.; Elorza, B.; Caballero, A.H.; Acosta, N. Chitosan: An Overview of Its Properties and Applications. *Polymers (Basel)* **2021**, *13*, doi:10.3390/polym13193256.

206. Zhang, X.; Peng, X.; Zhang, S.W. Biodegradable Medical Polymers: Fundamental Sciences. *Science and Principles of Biodegradable and Bioresorbable Medical Polymers: Materials and Properties* **2017**, 1–33, doi:10.1016/B978-0-08-100372-5.00001-5.